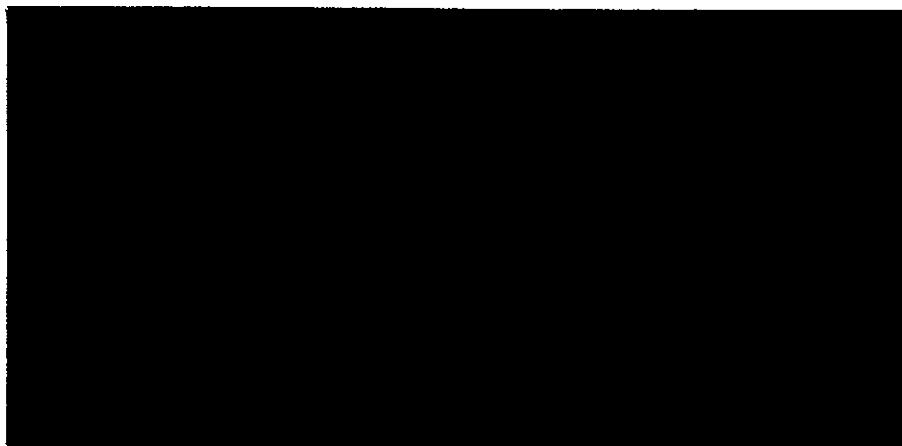


201 (11.1)



MISSILES AND SPACE DIVISION
LTV AEROSPACE CORPORATION

P. O. Box 6267

Dallas, Texas 75222

N71-26224

(ACCESSION NUMBER) **141** (THRU) **63**

(PAGES) **CR-114913** (CODE) **15**

(NASA CR OR TMX OR AD NUMBER) (CATEGORY)

FACILITY FORM 602



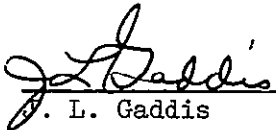
NASA Recall No. CR114913
Final Report
Contract 9-11254
VMSC Report No. 00.1427

FEASIBILITY DEMONSTRATION
OF A
SPRAYING FLASH EVAPORATOR
7 May 1971

Written:

Reviewed:

Approved:


J. L. Gaddis


R. J. French


F. T. Esenwein

Vought Missiles and Space Company
LTV Aerospace Corporation
P.O. Box 6267
Dallas, Texas 75222

ABSTRACT

This report is the final report of an effort to demonstrate the feasibility of a direct spray flash evaporator concept for Environmental Control System application. Included are analytical studies of particle freezing, evaporation on the wall, and controls. Analytical uncertainties were resolved by experimental data in a preliminary test. A documentation test of two evaporator configurations rejected 25,000 BTU/hr from an active transport loop using H₂O, Freon 22, and NH₃ as evaporants. Evaporant efficiencies of over 90% were achieved and outlet temperature control by evaporant pulsing was performed.

TABLE OF CONTENTS

Abstract	ii
List of Nomenclature	v
List of Figures	viii
List of Tables	xii
1.0 SUMMARY	1
2.0 INTRODUCTION	3
3.0 TECHNICAL DISCUSSION	4
3.1 Motivation Toward a Spray Evaporator	4
3.2 Design Requirements	8
3.3 Analytical Considerations	8
3.3.1 Evaporation Rates	8
3.3.2 Freezing Time	13
3.3.3 Evaporator Flooding	16
3.3.3.1 Characteristic Droplet Supply Time	21
3.3.3.2 Characteristic Droplet Evaporation Time	22
3.3.4 Transport Fluid Design	26
3.4 Control Schemes	34
3.5 Design of Configuration	38
3.5.1 Liquid Spray Devices	38
3.5.2 Evaporator Shape and Size	40
3.5.3 Exit Vapor Port Sizing	42
3.6 Thermal Model Development	44
3.6.1 Control Models	44

TABLE OF CONTENTS (CONTINUED)

3.6.2	Evaporation Models	45
3.6.3	Flash Evaporator Thermal Models	45
3.6.4	Results	51
3.7	Exploratory Tests	64
3.8	Feasibility Documentation Test	83
4.0	A SUGGESTED FLASH EVAPORATOR DEVELOPMENT PLAN	109
5.0	CONCLUSIONS AND RECOMMENDATIONS	115
6.0	REFERENCES	116
	APPENDIX - Computer Program	117

LIST OF NOMENCLATURE

A	Evaporator area
A	Vapor exit hole area
C _p	Specific heat
d _d , D	Droplet diameter
d _s	Splattered droplet diameter
d _i	Inside tube diameter
E	Valve open fraction
f	Friction factor
g _c	Gravitational proportionality constant
h	Heat transfer coefficient
h	Enthalpy
K	Thermal conductivity
L, l	Length
\dot{m}	Mass flow rate; Sub _e evaporation, Sub _s supply
Nu	Nusselt number, hd/k
P	Pressure
Pr	Prandtl number cp^{μ}/K
Q	Heat rate
Q/A	Heat flux sometimes denoted Q'' after Jakob
R	Gas constant
r	Radius
r _o	Outside radius
r _s	Splattered drop radius

Re	Reynolds number $\rho v x / \mu$; $Re_{di} = \rho v d_i / \mu$
t	Time coordinate
T	Temperature
T _w	Wall temperature
T _s	Surface temperature
T _{sat}	Saturation temperature (interphase temperature at observed pressure)
T _f	Fluid temperature (bulk or mixing cup)
\bar{v}	Average molecular velocity
\bar{w}	Weight flow rate
W	Weight
W _e	Evaporator weight
W _f	Expended fluid weight
x	Space coordinate; Sub-i interface, Sub-s surface
α	Thermal diffusivity $K/\rho c_p$
ϵ	Root of transcendental equation in freezing of droplets
δ	Thickness
Δ	Difference in (used as prefix)
ϵ	Temperature difference
ϵ	Emittance
θ	Off axis angle
λ	Latent heat of phase change
λ_{ij}	Phase change from i to j; 1 = solid, 2 = liquid, 3 = vapor
μ	Viscosity (dynamic)
μ	Also indicates micrometer 10^{-6} m or a micron

ρ	Fluid density
σ	Fluid surface tension
τ	Time, usually a particular interval
ϕ	Azimuthal angle

LIST OF FIGURES

<u>Figure Number</u>	<u>Title</u>	<u>Page</u>
Figure 1	Mechanisms for Evaporation	5
Figure 2	Single Droplet Possibilities	6
Figure 3A	Evaporation Rates for Water	10
Figure 3B	Evaporation Rates for Ammonia	11
Figure 3C	Evaporation Rate for Freon 22	12
Figure 4	Particle Size Distribution Produced by Typical Nozzles	14
Figure 5	Freezing Characteristics of Liquid Spheres	15
Figure 6	Effect of Particle Diameter on Freezing Time in a Vacuum	18
Figure 7	Effect of Ambient Pressure on Freezing Rates	19
Figure 8	Diameter of Particles which Completely Freeze During Transit	20
Figure 9	Characteristic Supply Time for Three Fluids	23
Figure 10	Phase Position History for a .0001 Ft. Thick Droplet on a 60 Degree F Wall in a Vacuum	25
Figure 11	Variation of Evaporation Time with Thickness and Wall Temperature	27
Figure 12A	Evaporation and Supply Times for Water	28
Figure 12B	Evaporation and Supply Times for Freon 22	29
Figure 12C	Evaporation and Supply Times for Ammonia	30
Figure 13	Transport Side Pressure and Temperature Characteristics	32
Figure 14	Transport Side Pressure and Temperature Characteristics	33
Figure 15	Sixteen Parallel Flow Path Results with Freon 21 Transport Fluid	35

<u>Figure Number</u>	<u>Title</u>	<u>Page</u>
Figure 16	Area Required with Various Tube Numbers	36
Figure 17	Particle Size Distribution in Full Cone Spray	41
Figure 18	Test Article Showing Thermocouple Locations	47
Figure 19	Thermal Model Development	48
Figure 20	Model 2 and 3 Cylindrical Evaporation Details	49
Figure 21	ECS Schematic with Flash Evaporator	50
Figure 22	Evaporant Deposition on the First Five Nodes	52
Figure 23	Evaporant Deposition on First Six Nodes	53
Figure 24	Evaporant Deposition on the First Seven Nodes	54
Figure 25	Ammonia Spray Analysis Correlation	55
Figure 26	Proportional Control Results	57
Figure 27	Organ Pipe Control Results	58
Figure 28	Effect of Control Band on Overshoot and Oscillation Period	59
Figure 29	Effect of Downstream Position on Overshoot and Oscillation Period	60
Figure 30	Computed Pressure to High Load Profile	61
Figure 31	Computed Response to Low Load Profile	62
Figure 32	Effect of Tubing Extension on Amplitude of Temperature Variations	63
Figure 33	Orifice Flow Data Measured for Atmospheric and Vacuum Conditions	65
Figure 34	Typical Spray Patterns	66
Figure 35	Illustration of Data Features	69
Figure 36	Results of Preliminary Water Test	72

<u>Figure Number</u>	<u>Title</u>	<u>Page</u>
Figure 37	Refrigerant 22 Evaporation Enthalpies	74
Figure 38	Effect of Spin Test on Spray Distribution	76
Figure 39	Azimuth Angle Effect of Spin Test on Spray Distribution	77
Figure 40	Azimuth Angle Effect of Spin Test of Spray Distribution	78
Figure 41	Acceleration Effects on Evaporant Distribution	80
Figure 42	Vaporization Enthalpy Achieved with Ammonia	82
Figure 43	Plate Evaporator Under Construction	84
Figure 44	Cylindrical Evaporator Under Construction	85
Figure 45	Schematic of Test Installation	86
Figure 46	Cylindrical Evaporator Installed in Vacuum Chamber	87
Figure 47	Cylindrical Evaporator in Chamber	88
Figure 48	Plate Evaporator Installation	89
Figure 49	Plate Evaporator Installation	90
Figure 50	Evaporator Test Support Equipment	91
Figure 51	Temperature Instrumentation Locations	92
Figure 52	Thermodynamic Results-Freon 22-Profile 1-Cylinder	94
Figure 53	Thermodynamic Results-Freon 22-Profile 2-Cylinder	95
Figure 54	Thermodynamic Results-H ₂ O-Profile 1-Plate	96
Figure 55	Thermodynamic Results-H ₂ O-Profile 2-Plate	97
Figure 56	Thermodynamic Results-H ₂ O-Profile 1-Cylinder	98
Figure 57	Thermodynamic Results-H ₂ O-Profile 2-Cylinder	99

<u>Figure Number</u>	<u>Title</u>	<u>Page</u>
Figure 58	Thermodynamic Results-NH ₃ -Profile 1-Plate	100
Figure 59	Thermodynamic Results-NH ₃ -Profile 2-Plate	101
Figure 60	Cooling Distribution Per Length in Plate	104
Figure 61	Cooling Distribution Per Length in Cylinder	105
Figure 62	Distribution of Evaporant With Angle	106
Figure 63	Flash Evaporator Program Schedule	114

LIST OF TABLES

Table 1	Design Requirements	9
Table 2	Comparison of Methods to Compute Freezing	17
Table 3	Primary Configurations	68
Table 4	Summary of Test Results With Water	71
Table 5	Thermodynamic Results	103
Table 6	Nozzle Freezing Data	107
Table 7	Flash Evaporator Feasibility Study (Phase I)	110
Table 8	Flash Evaporator Preliminary Design/Development (Phase II)	111
Table 9	Research Support to Phase II and Phase III Effort	112
Table 10	Flash Evaporator Flight Prototype Design (Phase III)	113

1.0 SUMMARY

This report presents the results of a first phase of effort to develop a heat rejection system which can flash expendable fluids to vapor by spraying them onto a heated surface. The heated surface in this instance is the Space Shuttle Environmental Control System transport fluid loop with its corresponding design requirements. Simplicity guidelines for the development of the spraying flash evaporator preclude active backpressure control, and encourage the incorporation of simple evaporant control.

The spray method of admitting evaporant is chosen over other methods due to the desire to control the heat rejection by supply rate modulation. Boilers and pool evaporators must depend on backpressure, and sublimators lack the ability to perform over a large heat load range. Should the spray freeze in transit to the wall, an efficiency loss is sure to occur so that this condition is avoided. If the spray is supplied at an excessive rate, a film will be built up on the surface and the control by supply rate modulation will be lost. Thus both freezing and flooding must be avoided to achieve the expected "dry wall" evaporation.

A brief analytical investigation of freezing indicates that the expected water particles (of size 100 microns) must be protected from freezing by providing an atmosphere of vapor. This atmosphere can be provided by judicious selection of the vapor exit area without active backpressure control. It is argued that the pressure response of the evaporator is quick enough during off-on cycling to insure high efficiency. An analytical difficulty lies in attempting to judge how frozen a particle could be tolerated before "egg shell" splattering is not observed. A preliminary test conducted demonstrated that saturation temperatures of about 0F to 20F result in a favorable environment, which may be readily supplied by exit port sizing.

Flooding analysis has been investigated on an average particle basis with a microscopic viewpoint. The time of droplet resupply is calculated; it depends on the spread out drop thickness and the evaporator area. The time of droplet evaporation is similarly calculated; this depends primarily on the spread out droplet thickness. A comparison of these characteristic times for the particle size range expected yields a critical evaporator area at which flooding is expected. The critical area is that at which resupply time equals evaporation time. If the resupply time is longer than the evaporation time, flooding is not anticipated. It is shown that heat fluxes of about 20,000 BTU/FT²-HR may be expected without flooding such that the evaporator may be quite compact.

A thermal model was constructed to facilitate control system parametric analysis, perform the predictions and evaluation, and as an aid to progressive design. The control systems considered were (1) proportional control, where evaporant flow is proportional to heat load, (2) organ pipe control, where a group of modularized mini-evaporators are turned off and on according to load, and

(3) off-on control. The first is not compatible with the backpressure control required, while the other two are. The organ pipe control is positive but requires a more complicated control system. Also considered but not analyzed is a predicted cycle system which similarly has a more complicated control system. The off-on control was analyzed to perform satisfactorily but is susceptible to non-uniform cooling distribution, sensor displacement, and other relatively minor details. The off-on valve is projected to require several millions of cycles during a high duty cycle shuttle lifetime, but current valve technology is adequate for this requirement.

Two tests were run during the course of the effort. The first, an exploratory test, showed the backpressure dependence on particle freezing, provided an initial evaporation efficiency estimate, and evaluated Hg effects on a preliminary basis. Data from this test aided greatly in the design of the feasibility demonstration test model. Also Hg effects were shown to have at most a moderate degrading effect.

In the second test a pair of test articles were constructed by winding rectangular copper tubing to simulate an evaporator shell. The configurations were cylindrical with end cap and "T-V tube" shapes. The spray was directed onto the active surface of the coils through which water transport fluid was flowed. Freezing of the spray nozzle with water turned out to be a nuisance causing about three days' delay to overcome. Freezing of the transport fluid in the coil with freon and ammonia was encountered. A two-sensor control partly eliminated the transport freezing while use of high conductivity materials (brass) in the evaporant fittings and valve suppressed valve freezing.

The tests indicated feasibility of the concept while also dictating the course of action to be followed. Heat loads exceeding the objective by 70 percent and inlet temperature ramps exceeding the objective were demonstrated. The average evaporation efficiency (referenced to a calculated maximum at the pressures expected) was for H_2O 93%, for freon 90%, and for NH_3 80%. The exit vapor sizing sufficiently eliminated spray droplet freezing tendencies to allow this high efficiency. Heat load control by evaporant metering according to transport fluid temperatures was demonstrated. The outlet temperature control band objective was not met indicating a need for further consideration. Freezing of the water injection nozzle from trapped hold up liquid similarly requires further consideration. The demonstrated evaporative heat fluxes will require an excellent heat transport fluid design incorporating entry length and extended surface (fin) effects for optimum design. This transport fluid surface design should also be pursued.

2.0 INTRODUCTION

The advent of manned space flight has resulted in the requirement of cabin thermal control; which, with other low-temperature waste heat sources produces a requirement for heat rejection. Generally speaking, heat rejection requirements for longer than a few days in duration are met with least weight penalty through space radiators. For short term heat rejection and topping of load peaks, expendable heat rejection systems are weight competitive, especially in the case of water evaporant which is generated by the auxiliary power system and thus does not represent a launch weight penalty. During atmospheric flight, water evaporates at a temperature too high to be of use in an environmental control system. For such an application fluids such as ammonia (from a weight usage standpoint) or a fluorinated hydrocarbon (from a materials compatibility consideration) are candidates. It is envisioned that two evaporants may be used on typical space shuttle flight: as redundant systems or top-off primary heat sinks during space operation, and as primary heat rejection during atmospheric operation.

Current devices evaporate water or Freon or freeze and sublimate water to accomplish the heat rejection. These devices have demonstrated operational difficulties when they are projected into the space shuttle anticipated flight schedule. The wicks used for liquid control in the evaporators are incapable of proper function at high accelerations and they have proven to be difficult to negotiate repeated quiescent operation. In addition, the backpressure control which is needed to regulate the heat transfer rate is felt to be an item of reduced reliability. The porous plate is deficient in that repeated start up requires waste of evaporant each time; the load range is limited; and the porous plate both deteriorates and may support bacteria growth.

Because of the shortcomings of existent devices, a suitable alternative was sought. It was deemed intuitively feasible to develop a device which would simply spray the evaporant onto the wall containing the environmental control heat transport fluid. Such a concept would avoid many of the possible operational difficulties while permitting the incorporation of several evaporants within the same device. The program reported herein is the feasibility study of the flash evaporator concept which culminates in the demonstration of a simple, advanced model of a flash evaporator.

The report begins with an expression of the motivation which drives to the selection of the spray evaporation mode. Following this is an analysis of the breadth of parameter range which can be tolerated, a discussion of applicable control modes, a description of attractive concepts, and the development of a mathematical model. Following this is a description of an exploratory test; and finally the documentation test results are incorporated. The technical discussion is followed by a plan whereby the development of the flash evaporator prototype may be accomplished.

3.0 TECHNICAL DISCUSSION

3.1 Motivation Toward a Spray Evaporator

The flash evaporator described herein is a device in which an expendable coolant is used to cool a transport fluid by evaporation. The rudimentary operation expected is simply that in which the evaporant is sprayed onto a surface which is highly conductive (thermally) to the transport fluid. The application which is most obvious is that of the space shuttle. In the shuttle, the evaporator can be used in several ways: (1) as a primary heat absorber in atmospheric flight phases, (2) as a supplementary heat absorber in normal space operation, and (3) as a redundant system with full load capacity. Atmospheric operation implies that a fluid other than water must be used. Other fluids under consideration are ammonia and fluorinated hydrocarbons.

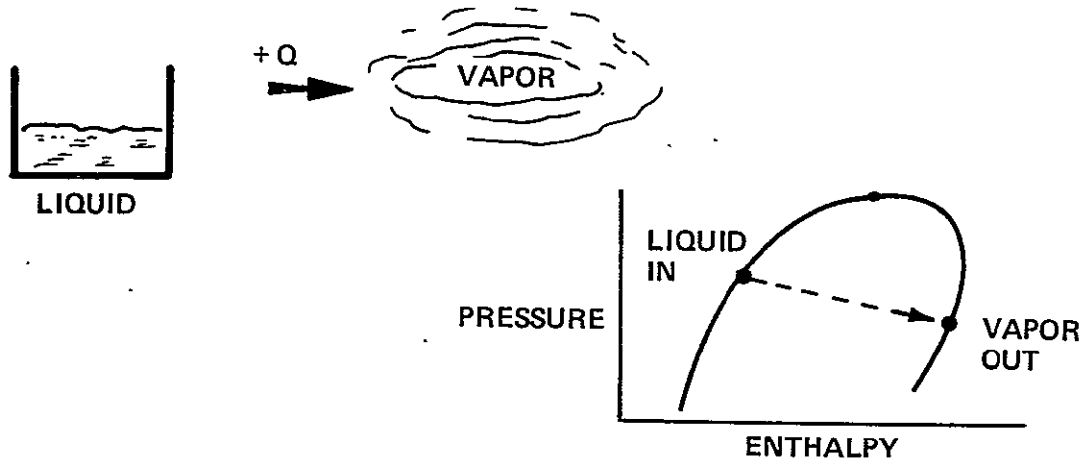
Several devices are in existence which evaporate an expendable by one of the mechanisms of Figure 1 to cool a transport line. However, these devices have operational disadvantages which presumably would not occur with a simple spray evaporator. Because of the unique possibilities of a device which functions on such a principle a program was initiated to determine the feasibility of its operation. The remainder of this report is devoted to analysis and test of such a spray evaporator.

The single droplet striking a heated wall can be expected to result in any of several modes of heat transfer illustrated in Figure 2.

1. The droplet can be frozen before impact and transfer heat during impact by conduction.
2. The droplet can strike a locally dry heated wall and evaporate or boil completely before being struck sufficiently often that a persistent film results.
3. The droplet can strike a surface and boil violently upon impact that the liquid-solid contact is impaired, producing low heat fluxes and possible expulsion of the droplet. The latter condition is termed a Leidenfrost phenomenon.
4. The droplet can strike on another particle or in a liquid pool and accumulate faster than the loss by evaporation.

The aforementioned modes of droplet heat transfer affect the operation of the flash evaporator. A consideration of maximum heat fluxes, potential stability problems, and liquid displacement due to accelerations establishes preferred modes. First consider mode 4 and presume the heat transfer occurs by conduction from the surface through the film of liquid. If the liquid surface and wall temperatures are fixed, the heat transfer

per unit area is given by $Q'' = K \frac{\partial T}{\partial X} = K \frac{T_w - T_s}{\delta}$. In this equation, K is the



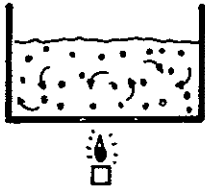

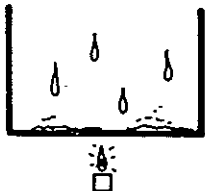
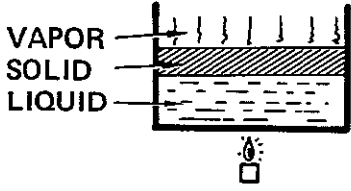
MECHANISM	RATE CONTROL VARIABLE
	BACKPRESSURE
	BACKPRESSURE
	SUPPLY RATE
	ICE THICKNESS (SELF REGULATING)

FIGURE 1 MECHANISMS FOR EVAPORATION

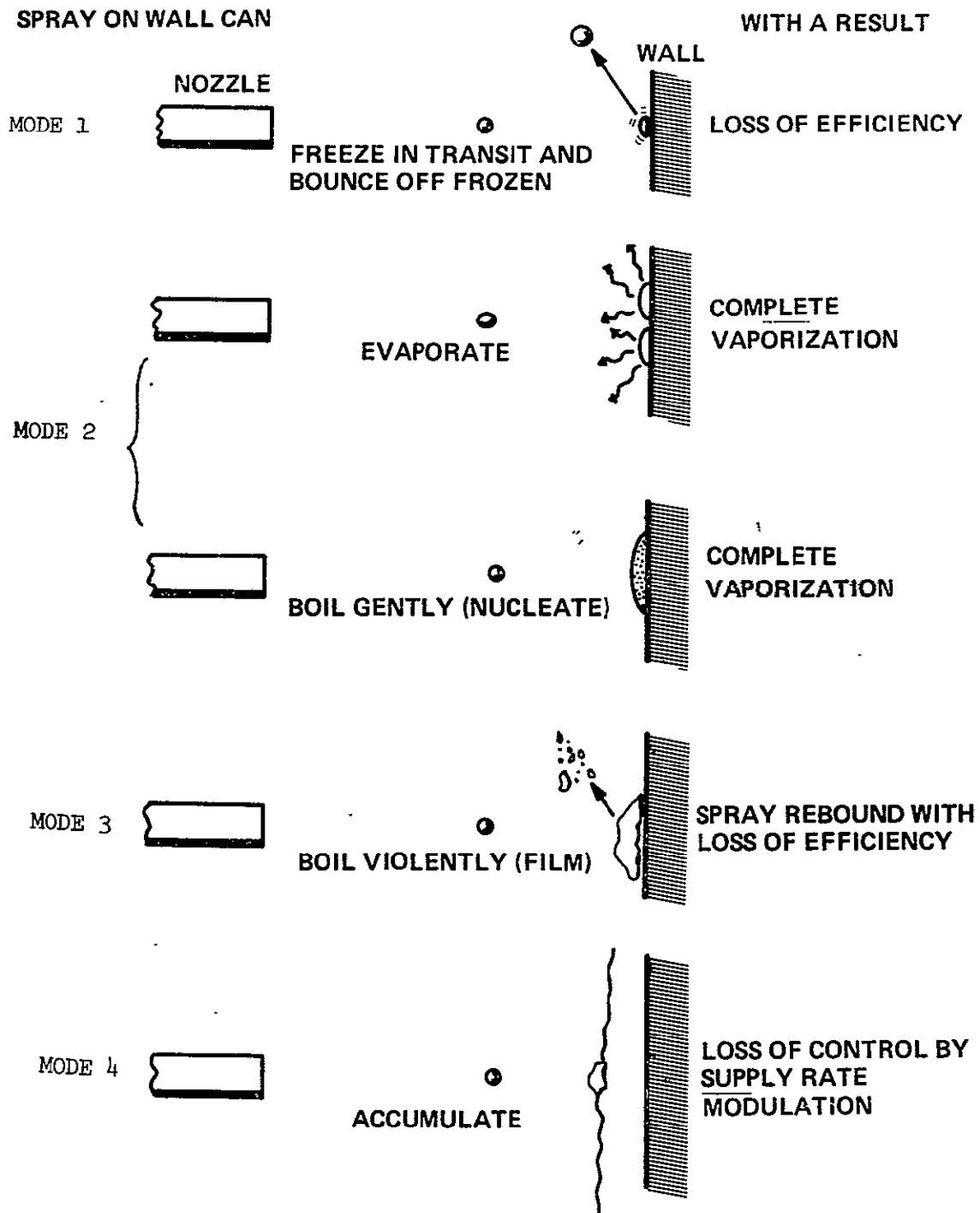


FIGURE 2 SINGLE DROPLET POSSIBILITIES

thermal conductivity, δ is the film thickness, and T_w and T_s are the wall and surface temperatures, respectively. The heat flux (Q'') is proportional to the evaporation flux (\dot{m}_e'') through $Q'' = \lambda_{23} \dot{m}_e''$, while the average liquid supply flux is \dot{m}_s'' . The thickness δ obeys the conservation equation $\rho \frac{d\delta}{dt} = \dot{m}_s'' - \dot{m}_e''$, where ρ is the density. If δ increases, Q'' must decrease resulting in a decrease in \dot{m}_e'' and $d\delta/dt > 0$. Similarly if δ decreases, $d\delta/dt < 0$ results. Any disturbance is therefore amplified unstably so that the film thickness is driven to zero or to grow until limited by some other factor. Thus, the assumption of mode 4 must resolve into either a mode 2 or 3 evaporator or one in which the supply rate cannot regulate the heat rate.

Now consider the mode 1 evaporator, having "ice pellet" heat transfer. In this mode the particle may not be completely solid, but has frozen enough that the shell does not break upon impact. The impact and rebound process is certainly a potentially complicated process. When the solid particle contacts the wall, it will deform and sublime. The sublimating wave will propagate into the ice layer, and the cool wave into the wall. The elastic compression of the wall and particle will tend to cause a rebound of the particle which is augmented somewhat by the vapor production. Upon rebounding some of the particle may remain on the wall and evaporate. The heat flux possible to achieve is not estimable easily due to the several competing rate processes, and the droplet breakup. However, it is safe to say that high efficiency could only be obtained by more than a single wall contact by each particle - a requirement not applicable to a mode 2 evaporator.

The mode 3 evaporator droplet phenomenon has been studied extensively in conjunction with quenching applications of high temperature items cooled by spraying. References 1 and 2 in particular infer large heat fluxes and short contact times resulting in only about 30 percent droplet evaporation. This mode is like the "ice pellet" evaporator described above in that multiple impacts for each particle will be required to achieve high liquid use efficiency.

Mode 2 evaporators suffer none of the difficulties associated with the other modes. The heat flux rates will be the subject of a later discussion; but are adequate to allow a reasonably sized device. No stability problems are expected provided the mass addition fluxes are less than the critical fluxes at which the liquid film would tend to grow. The heat rejection rate control may be accomplished by inlet flow metering without back pressure control and without significant overshoot due to liquid storage. Liquids on the wall are never of a thickness such that moderate gravity effects will predominate over surface and viscous effects. The distribution of the spray is similarly not expected to be changed significantly during linear accelerations. Since the mode 2 "dry wall" device is apparently superior, the primary design considerations will be outlined for it.

3.2 Design Requirements

The independent variables over which the designer has control are: the size of the device, the shape or other configuration detail, the transport side features conductance and pressure drop, and the mode of control. Design guidelines for the present study are listed in Table 1. Of the candidate transport fluids, Freon 21 seems to be the most probable candidate, but the test reported herein used water which is also a candidate fluid.

3.3 Analytical Considerations

The desired mode of evaporation has been selected to be a spray directed onto the transport fluid structure. The droplets of the spray are intended to impact a dry wall and evaporate completely. This desired operation will fail to occur if the particles freeze in transit or if the droplets are supplied so fast that accumulation occurs on the wall. Within this range of operation, the performance of the device may be improved by causing the vapor to exit at an increased temperature.

3.3.1 Evaporation Rates

The rates of evaporation used in the present study are taken primarily from kinetic theory. The maximum evaporation rate from a liquid surface at temperature T is assumed to be equivalent to the rate of impingement of the vapor in equilibrium with the surface. This rate may be calculated from kinetic theory which predicts the flow per unit area (Reference 3)

$$\frac{\dot{w}}{A} = \frac{1}{4} \rho \bar{v} \quad (1)$$

Here \dot{w}/A is the mass flow per unit area leaving the surface, ρ is the density of saturated vapor, and \bar{v} is the average molecular velocity $(\frac{8}{\pi} g_c RT)^{1/2}$. The values of maximum evaporation rate are shown in Figure 3, a, b, and c, for H_2O , NH_3 , and CH_2Cl_2 .

At ambient pressures different from zero, the net mass evaporation flux is calculated assuming the evaporation and condensation coefficients are unity, thus.

$$\frac{\dot{w}}{A}_{net} = \left(\frac{\dot{w}}{A} \right)_{T_{surface}} - \left(\frac{\dot{w}}{A} \right)_{T_{saturation}}$$

This value of evaporation is of questionable validity according to Reference 4. However it is used for all calculations herein without modification unless otherwise indicated.

TABLE I
DESIGN REQUIREMENTS

ITEM	MAGNITUDE
Maximum load	25,000 Btu/hr
Minimum load	0
Inlet Temperature (transport fluid)	45-95°F
Control Temperature	45°F
Control Range of Outlet Temperature	35-45°F
Ambient Pressure	< .08 psia for H ₂ O .08 - 15 psia for NH ₃ or R-22
Evaporant Temperature	Room temperature

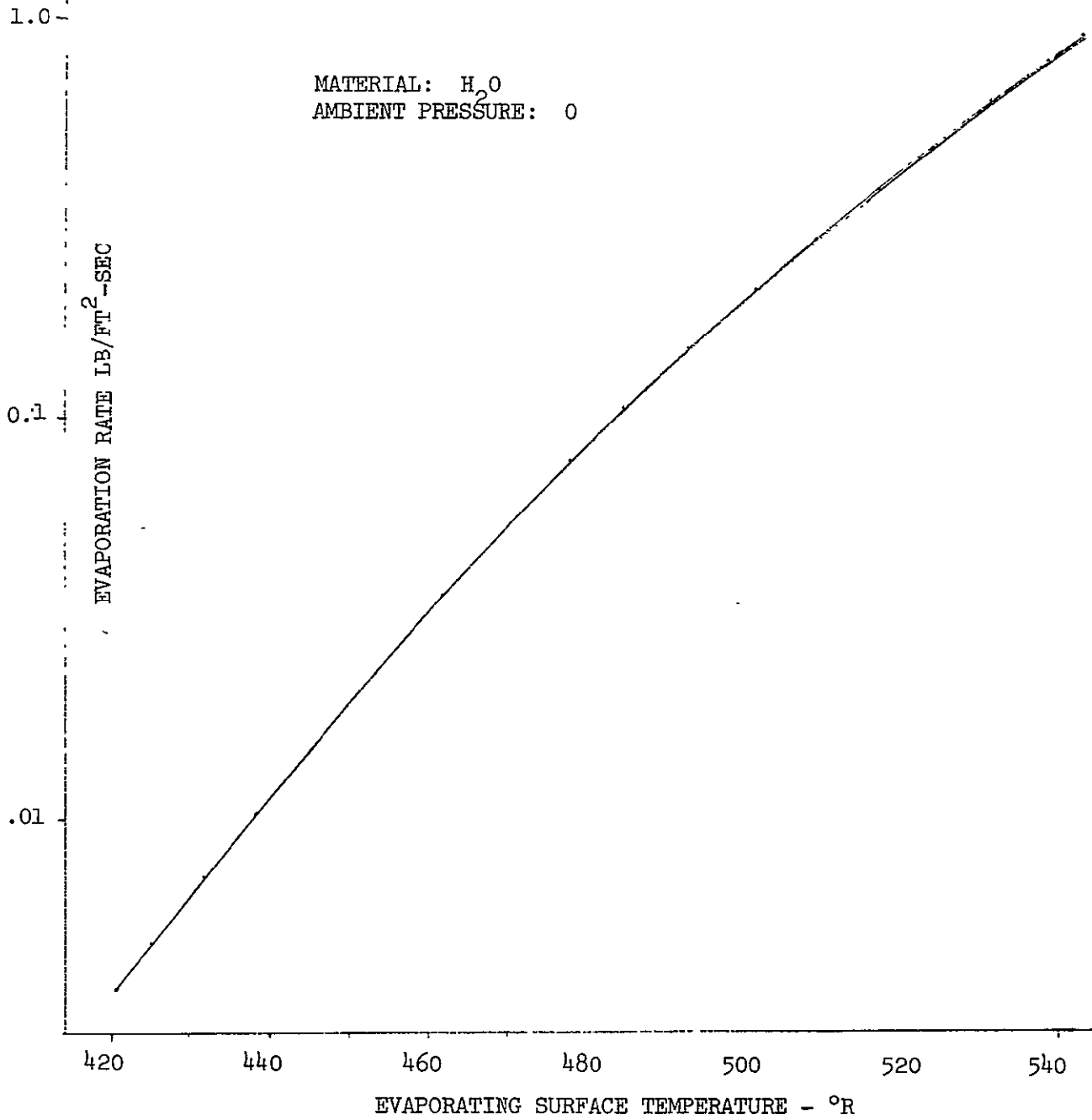


FIGURE 3A EVAPORATION RATES FOR WATER

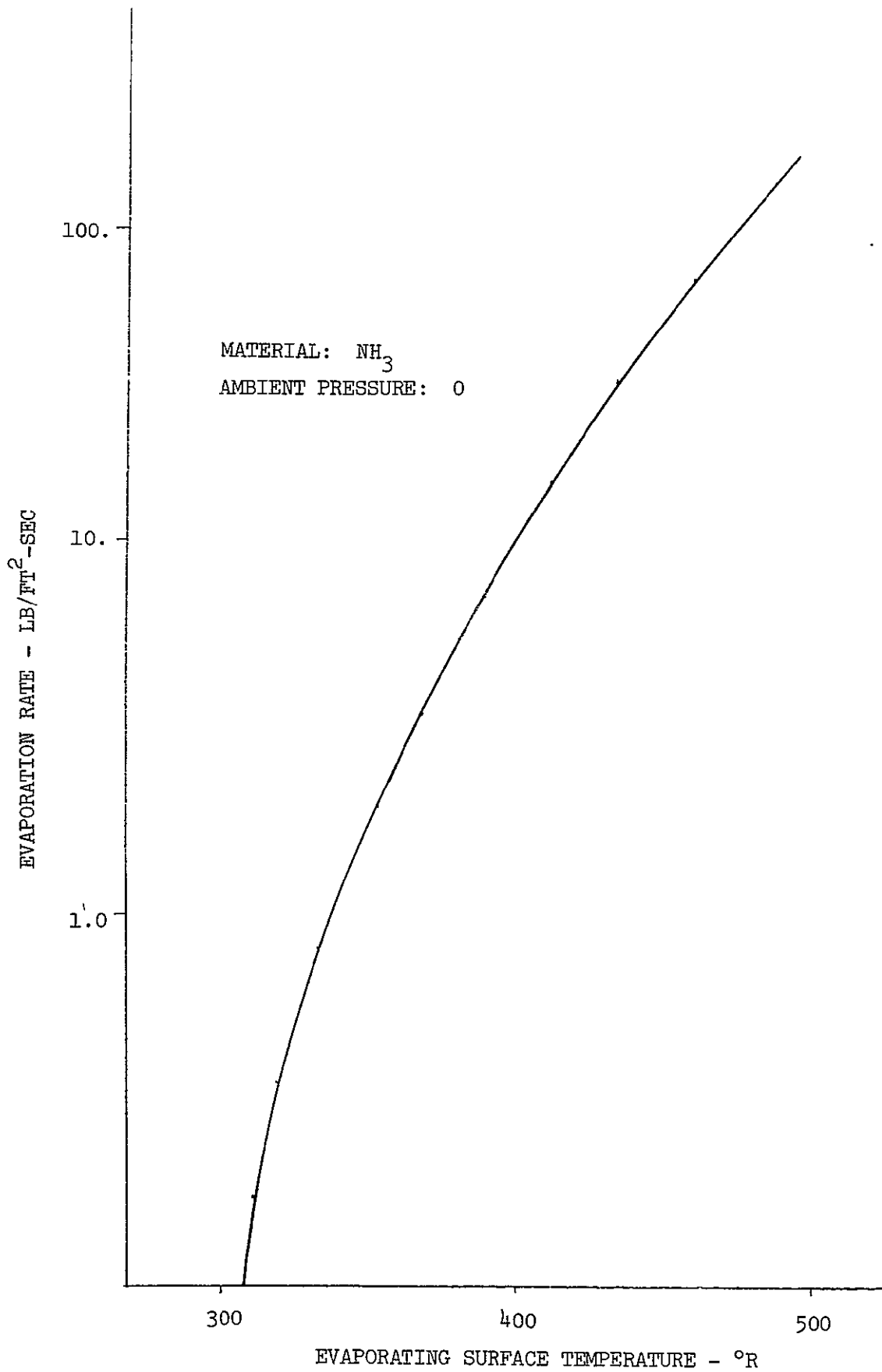


FIGURE 3B EVAPORATION RATES FOR AMMONIA

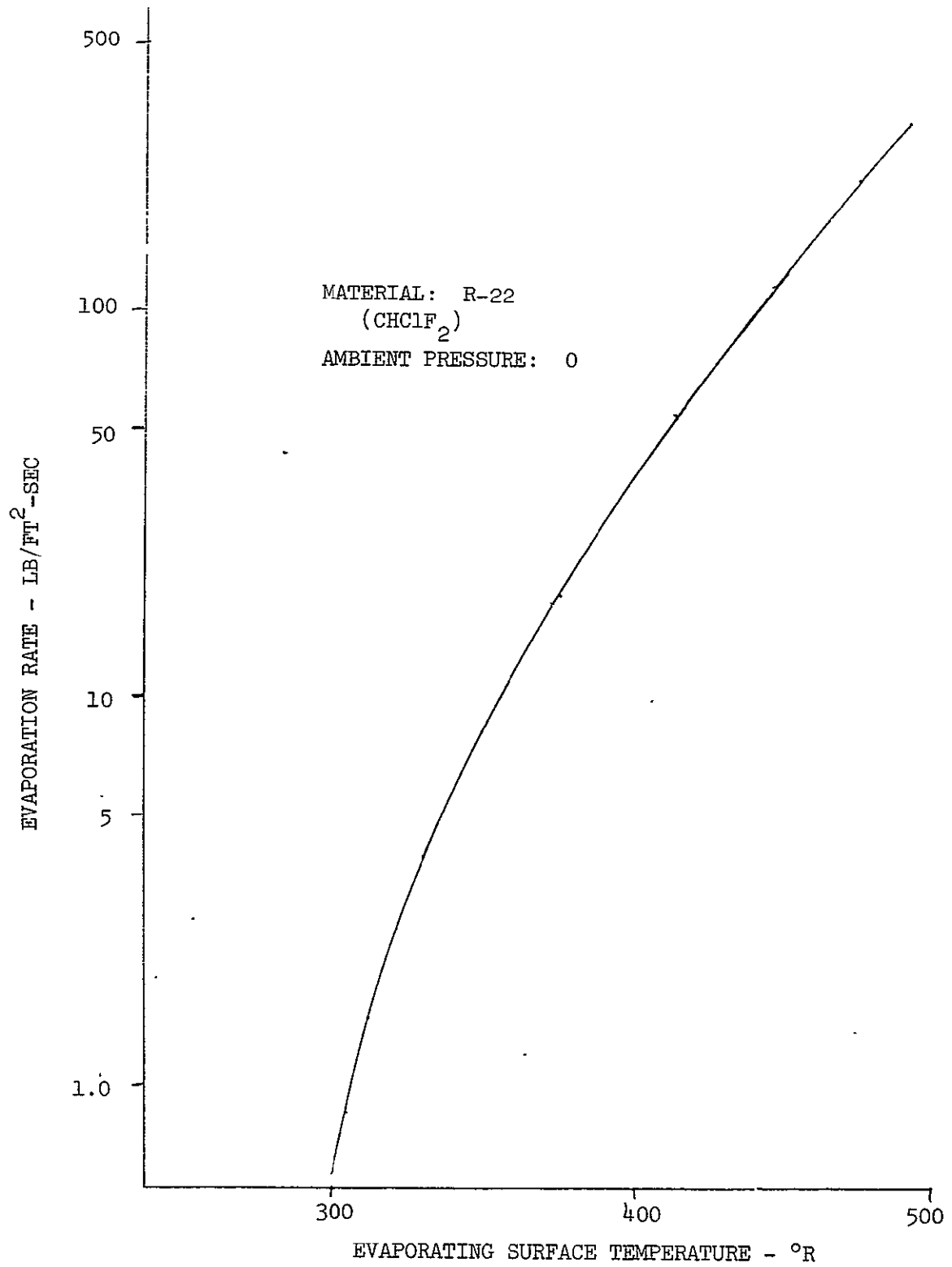


FIGURE 3C EVAPORATION RATE FOR FREON 22

3.3.2 Freezing Time

The droplet transit time for particles in vacuum is simply related to the velocity and distance from the nozzle to target. The fluid velocity is assumed to be given by

$$v = \left(\frac{2g_c \Delta P}{\rho} \right)^{1/2} \quad (2)$$

where ΔP is the pressure drop across the nozzle

ρ is the fluid density

v is the fluid velocity

This velocity has been verified for vacuum operation in References 5 and 6. In addition these references have shown an unexpected result. The particles in flight as photographed by high speed motion pictures, show clearly a "flicker" of reflection from as many as three spots on each droplet. When shown at normal speed, the particles appear to "revolve" at rates calculated up to 50,000 revolutions per second (Reference 6). This effect does not seem to affect the spray evaporator but is mentioned for interest only.

The size of droplets anticipated varies considerably with the spray device used. Figure 4 shows the droplet sizes obtained in a hollow cone atomizing type nozzle. These data are for water in atmospheric pressure; no vacuum studies are available for general nozzles.

There are several ways to analyze the freezing of a droplet by evaporation. The solution which takes account of all influences must be performed numerically and has been done for 100 and 1000 micron particles in Reference 6. In that work the particle was subjected to a vacuum and the particle initial temperature of 298K was employed. The analysis includes transient conduction in the interior liquid, propagation of the liquid-solid boundary, transient conduction in the ice shell, propagation of the evaporating boundary, and evaporation into a vacuum. The evaporation was reduced from its maximum theoretical value by some gas dynamic arguments deduced from one-dimensional (planar) flow considerations applied to the spherical case. Also, nucleation of the solid from liquid was assumed to occur without supercooling of the liquid phase.

Observation of the outcome of the calculations of the above described analysis leads to the understanding that the outer radius does not decrease significantly during freezing. Reference 7 extends a classical heat conduction solution to a spherical case with constant radius through both approximate analysis and numerical analysis. The result is reproduced as Figure 5 where the parameters $L = \frac{\lambda l_2}{c_p(T_f - T_s)}$ and

$\frac{4\beta^2 \alpha t}{r_0^2}$ are employed. In this solution, the liquid droplet is assumed

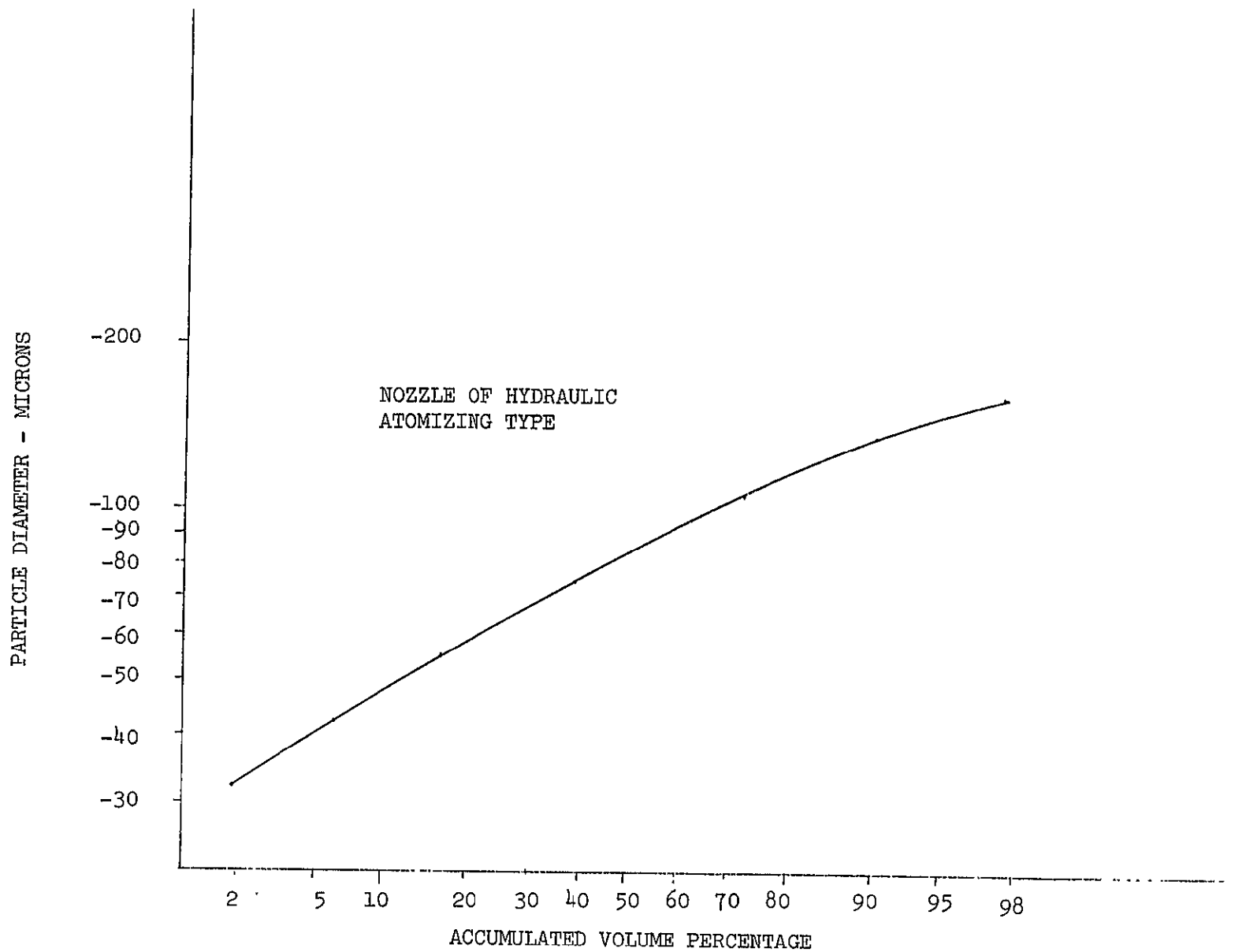


FIGURE 4 PARTICLE SIZE DISTRIBUTION PRODUCED BY TYPICAL NOZZLES

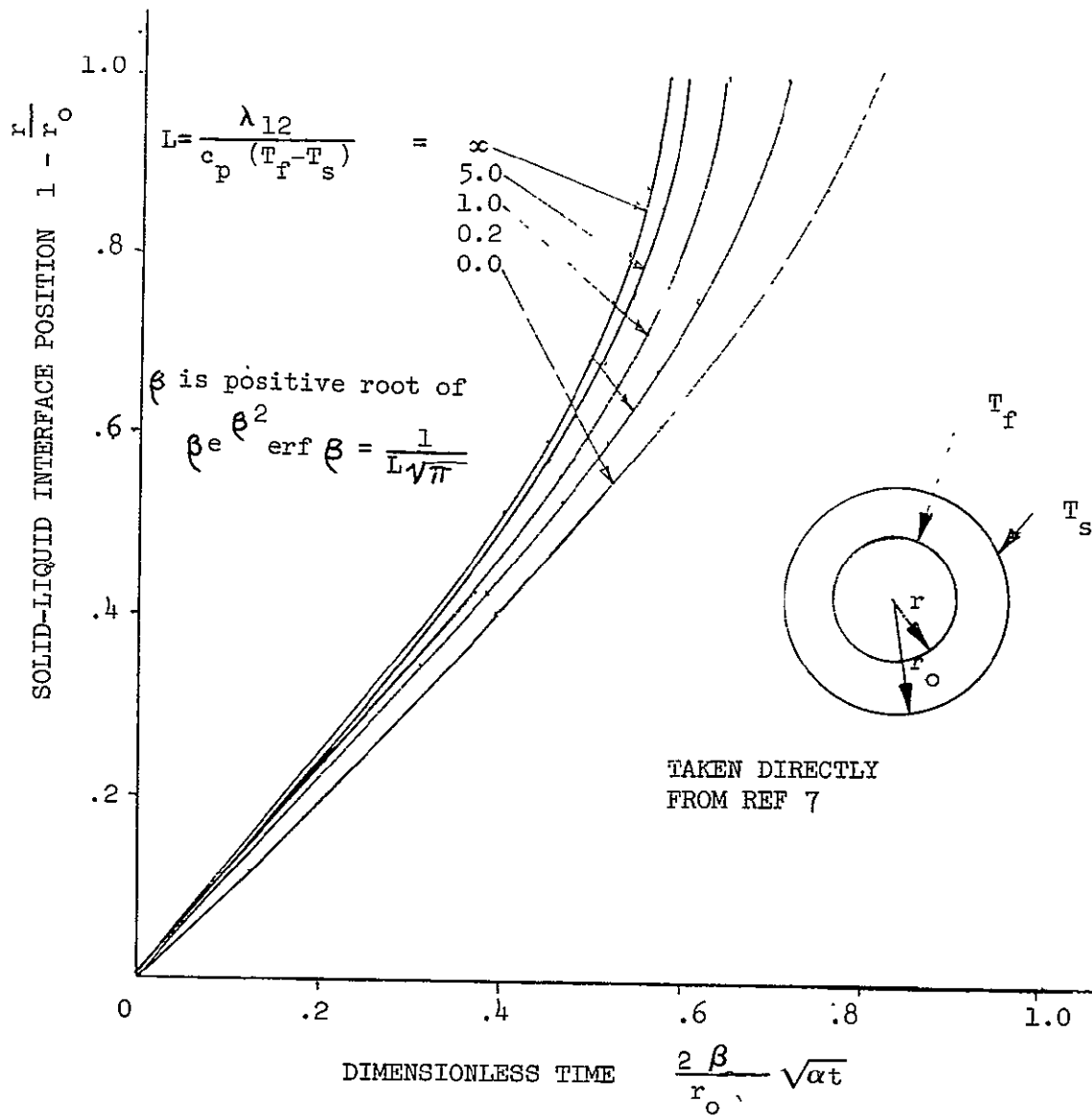


FIGURE 5 FREEZING CHARACTERISTICS OF LIQUID SPHERES

to be initially at the freezing temperature and the freezing interface propagates from a surface which is maintained at constant temperature. Table 2 compares the time to freezing as given by the foregoing theories. As can be seen, those facets ignored by the simplified theory are minor, including the effect of above-freezing initial temperatures. The temperature of the surface has a strong effect on the freezing rate, and is estimated using a simple heat balance iteration equating droplet enthalpy release and enthalpy leaving during freezing time.

An even simpler solution can be obtained assuming a particle of infinite conductivity so that the cooling is only dependent upon time. The time to freezing for this assumption is also shown in Table 2 and compares favorably with the other, more exact results. As expected, this analysis leads to a lower bound of the freezing time.

Apparently, there is little question concerning the length of time required for a particle to freeze completely, provided the projected evaporation rates are not suppressed as suspected by Reference 4. However, the amount of freezing which could be tolerated by a particle incident on a solid surface has not been accurately analyzed. The data which are available indicate that nearly completely frozen drops are still fluid enough to stick to a surface at about the exposure time corresponding to complete freezing.

It has been postulated that freezing of sprayed particles can occur within the range of expected transit times. It may be important, therefore, to predict the freezing time for a given set of conditions such as ambient pressure, particle diameter, and initial temperature. The simplified theory of Reference 7 predicts the effect of particle diameter shown in Figure 6, while the calculations of Reference 6 at 100μ and 1000μ are shown for comparison. The infinite conductivity model becomes less reliable for larger drops since the departure of surface temperature from the mean temperature becomes more significant for larger particles.

The initial particle temperature has such a minor effect on the freezing time that it may be ignored. However, the ambient pressure is quite important and its effect may be predicted readily from the theory of Reference 7. Figure 7 shows the time required to freeze a particle at various ambient pressures. From these data in Figure 7, one may predict the freezing tendency of a particular configuration. The path length of the spray is proportional to the square root of the area and inversely proportional to the velocity. For a fixed spray velocity and evaporator shape a set of curves like those of Figure 8 can be obtained. These curves show the diameters of particles which completely freeze in transit for the particular condition.

3.3.3 Evaporator Flooding

The following section addresses the problem of flooding of the evaporator surface. Two characteristic times are identified: (1) the

TABLE 2

COMPARISON OF METHODS TO COMPUTE FREEZING

<u>METHOD & DESCRIPTION</u>	<u>COOLING TIME AT WHICH FREEZING BEGINS</u>	<u>TIME TO COMPLETE FREEZING</u>
1. Exact (numerical) Initial temp = 77F Diameter = 100 μ Reference 6	.00035 sec	.00926 sec
2. Approximate method of Reference 7 Diameter = 100 μ Initial temp = 32F Surface temp = 20F	.0 sec	.012 sec
3. Infinite conductivity sphere Diameter = 100 μ Initial Temp = 77F	.00046 sec	.0064 sec

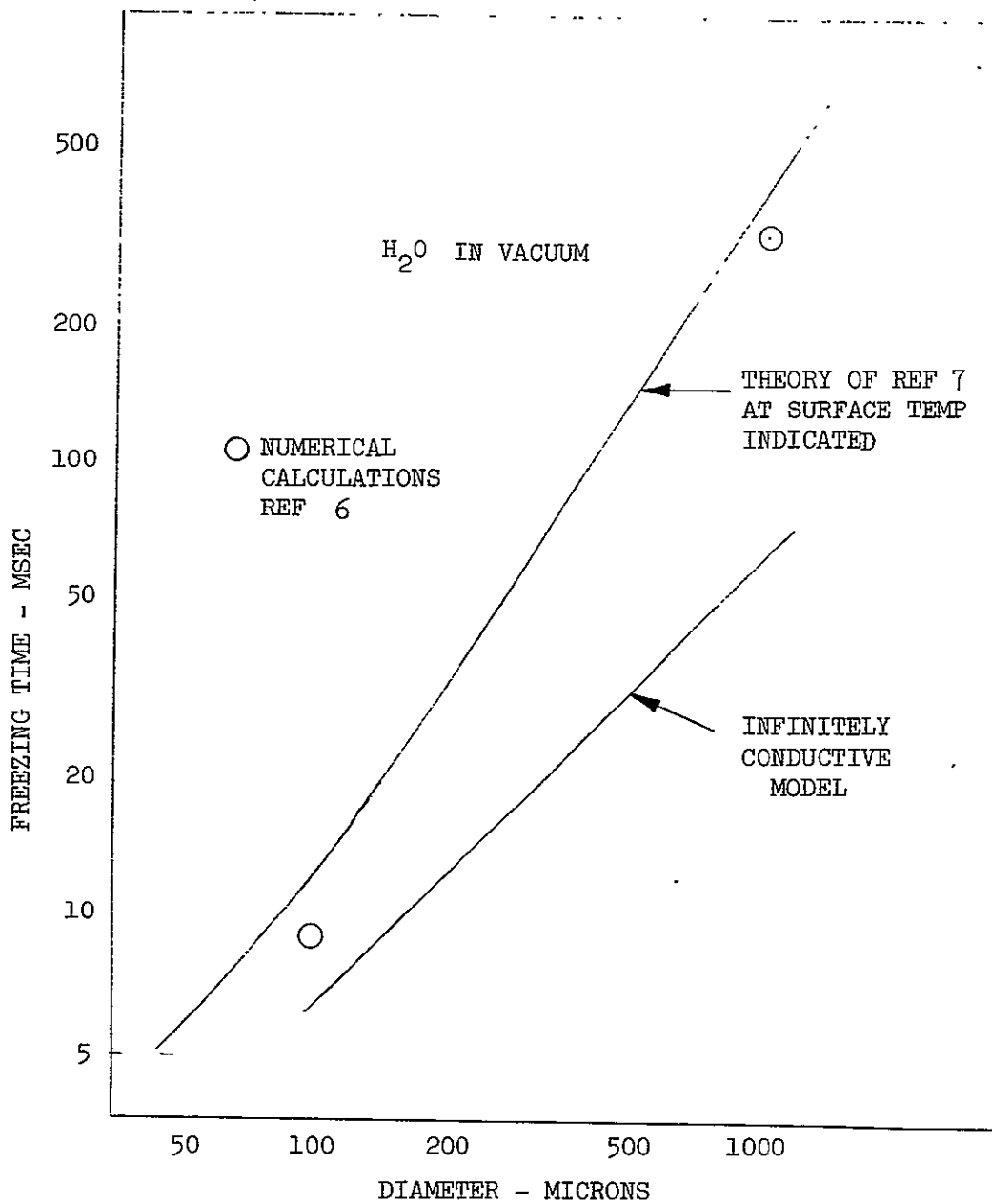


FIGURE 6 EFFECT OF PARTICLE DIAMETER ON FREEZING TIME IN A VACUUM

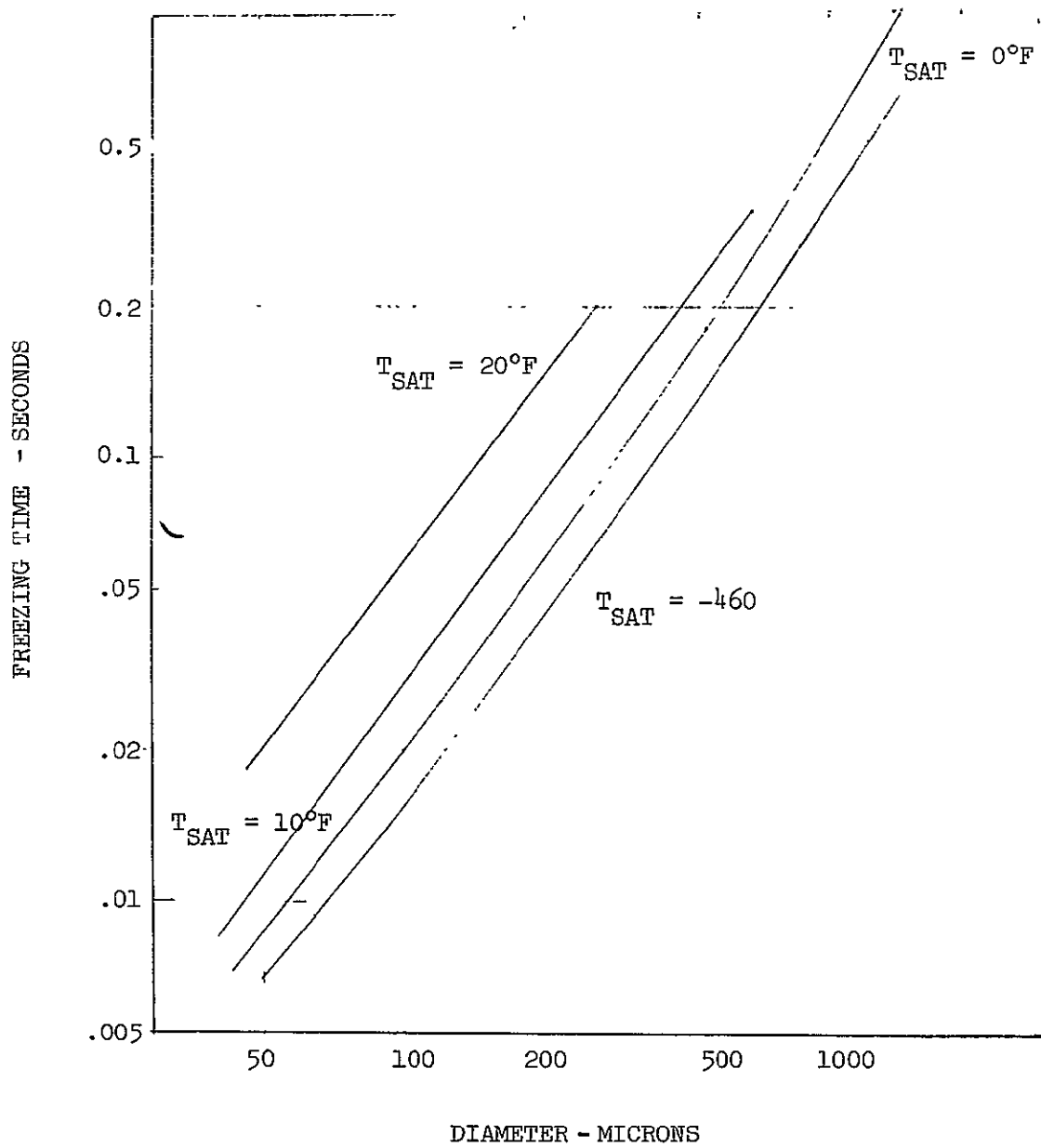


FIGURE 7 EFFECT OF AMBIENT PRESSURE ON FREEZING RATES

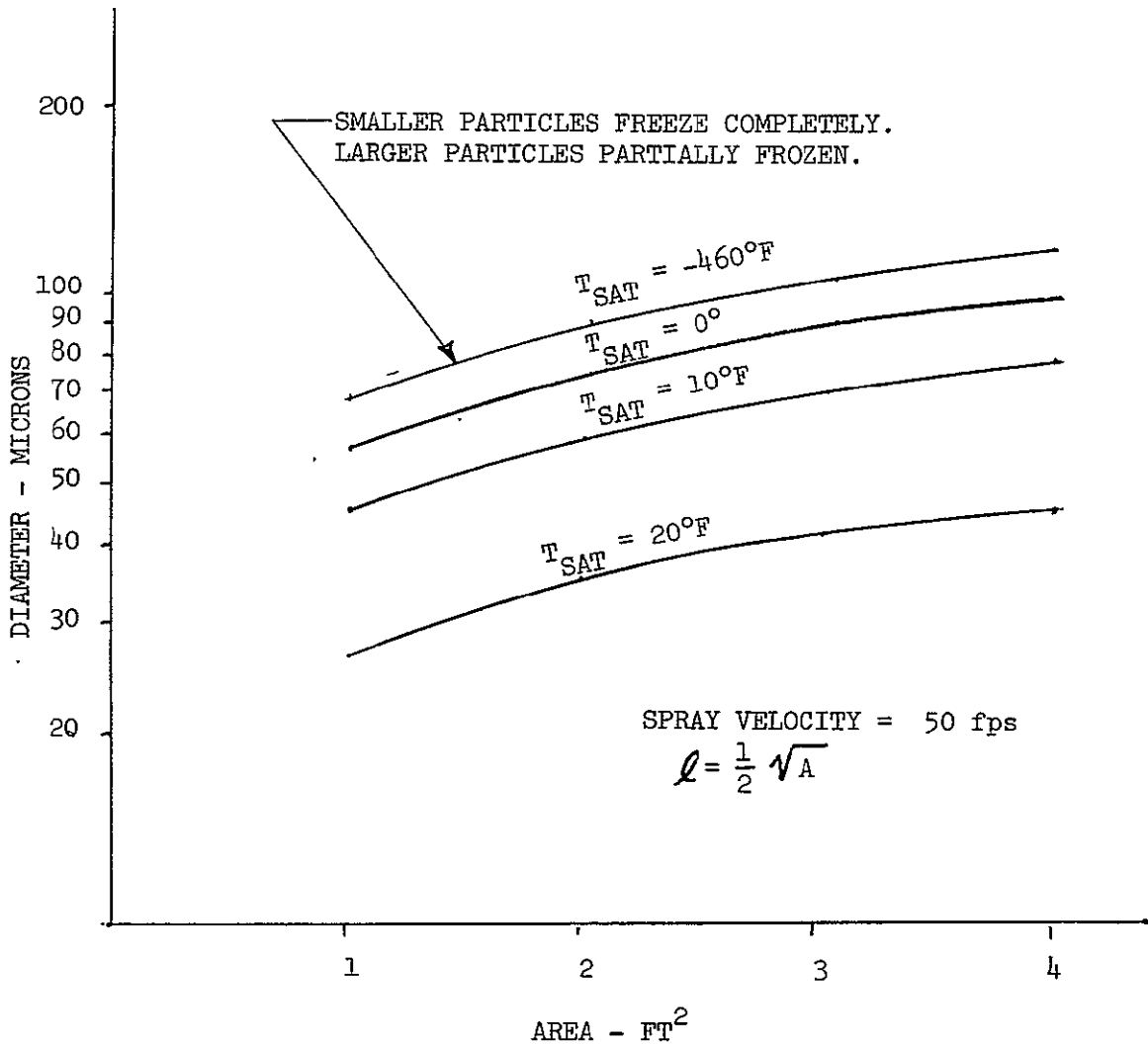
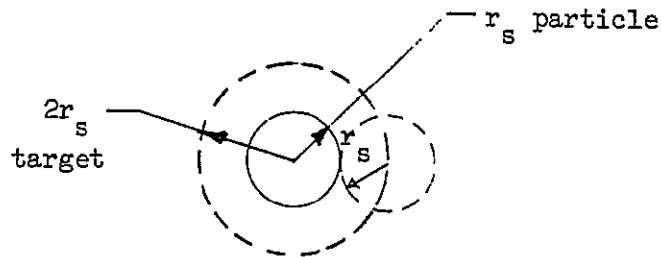


FIGURE 8 DIAMETER OF PARTICLES WHICH COMPLETELY FREEZE DURING TRANSIT

droplet supply time, and (2) the time of evaporation. Clearly when the supply time is approached by the evaporation time, an increasing number of particles will strike other particles which have not completely evaporated. There is a critical size of droplet which, on the average, will grow until some other mechanism removes it. This droplet size depends upon the two characteristic times identified. A crude rule followed herein that the design begins to "flood" when the characteristic times are equal. A considerable margin should be allowed with respect to this condition due to the approximate nature of the calculations involved.

3.3.3.1 Characteristic Droplet Supply Time

The rate per unit area of evaporant supply is an indication of the demand for evaporation. When the supply rate exceeds the evaporation rate, the surface becomes saturated and liquid buildup will begin. To calculate this effect, consider the mean time between droplet impacts. Begin with a droplet impact centered at a point. The droplet spreads to a radius r_s ; from whence, if another particle impacts with center within a target circle of radius $2r_s$ (see illustration below), the droplets will touch.



The area of the target is $4\pi r_s^2$ and the total area of the evaporator is A , so that there are $A/(4\pi r_s^2)$ targets. The mass of a single particle is $\frac{\pi}{6}\rho d_d^3$ and the mass supply rate is \dot{w} , so that there are $6\dot{w}/\pi\rho d_d^3$ particles per unit of time being produced. The particle and the impacted droplet must have the same mass, so if t is the droplet thickness,

$$\frac{\pi}{6}\rho d_d^3 = \pi\rho r_s^2 t$$

The average time to produce as many particles as targets is τ_s which is given by:

$$\frac{6\dot{w}\tau_s}{\pi\rho d_d^3} = \frac{\dot{w}\tau_s}{\pi\rho r_s^2 t} = \frac{A}{\pi 4 r_s^2}$$

$$\tau_s = \frac{A\rho t}{4\dot{w}}$$

(3)

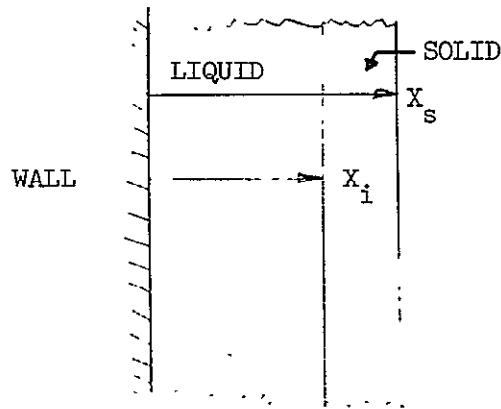
As expected, this time characteristic of droplet impact varies inversely with the volume supply flux $(\frac{\dot{w}}{A})$ of the spray, and is proportional to the drop thickness. It is reasonable to expect the droplet characteristic evaporation time to be independent of evaporator size and strongly sensitive to thickness at impact time. Some control can therefore be exerted by either droplet size (hence thickness) control or evaporator size. Increasing the area (A) of the evaporator will result in a more conservative design from the standpoint of flooding. The average impact times for the three fluids studied are shown in Figure 9.

The droplet spread time is apparently much faster than either the transit time or the evaporation time. The transit time is of the order of 10^{-2} seconds and the evaporation is of the order of 10^{-1} to 10^0 seconds. Reference 8 presents a test designed to determine, among other things, the droplet spreading characteristics. The data are for larger droplets at slower speeds but show the spreading phenomenon to occur within about .005 seconds. Smaller droplets at higher impact velocities are expected to spread in shorter times so that the spreading time can be neglected for practical purposes.

3.3.3.2 Characteristic Droplet Evaporation Time

The actual droplets striking the wall have definite temperature distributions, which upon impact are stretched and convulsed in a way judged impossible to determine. Any preliminary calculations quickly indicate that the evaporation time is fairly long compared with the time required for a heat pulse to pass through the droplet, so that (1) the complicated initial temperature distribution will smooth out, and (2) the entire evaporation process occurs at nearly steady state. The shape of the droplet on the wall is conveniently taken to be a cylinder whose height-to-diameter ratio can be varied parametrically. Two cases will be considered concerning the formation of solid: (1) the solid begins to form immediately at 32°F , and (2) the solid nucleation is zero (or no solid forms).

The sketch below shows a section out of an evaporating drop.



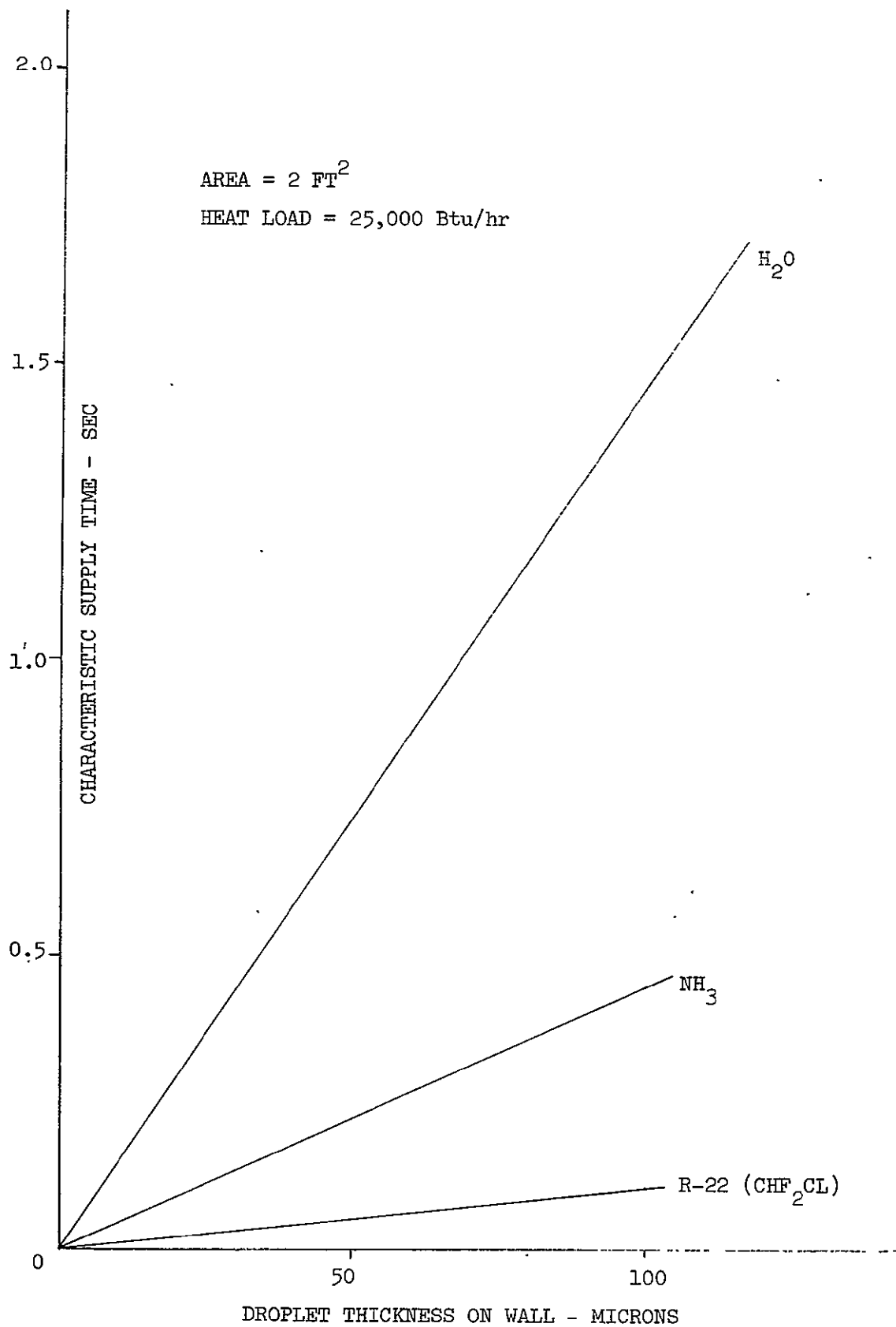


FIGURE 9 . CHARACTERISTIC SUPPLY TIME FOR THREE FLUIDS

The droplet cools until a layer of ice forms with the interface moving toward the wall and the ice boundary also erodes due to sublimation. The surface temperature regulates the sublimation rate according to

$$\left(e \frac{dx_s}{dt} = - \frac{\dot{m}}{A} \right) @ T_{\text{surface}}$$

The surface heat balance may be used to establish the value of surface temperature with quasi steady heat flow as

$$\lambda_{13} \frac{\dot{w}}{A} = K_1 \frac{T_s - T_i}{X_i - X_s} \quad (4)$$

The liquid/ice interface moves according to

$$\lambda_{12} \frac{dx_i}{dt} = K_2 \frac{T_w - T_i}{X_i} - K_1 \frac{T_i - T_s}{X_s - X_i} \quad (5)$$

These two equations, with \dot{w}/A given by Figure 3A may be solved by several methods. Herein a simple Euler integration scheme was employed. The results which are most pertinent are shown in Figure 10 which displays the movement of the boundaries with time.

A simpler model of the evaporation process is that of a non-freezing layer. In this scheme, the surface erosion is according to

$$\left(e \frac{dx_s}{dt} = - \frac{\dot{m}}{A} \right) @ T_{\text{surface}}$$

The surface temperature heat balance is

$$\lambda_{23} \frac{\dot{w}}{A} = K \frac{T_w - T_s}{X_s} \quad (6)$$

In this simple model there is a unique evaporation rate for each thickness independent of the initial thickness where in the other model there is not. The value of time to evaporation of the initial droplet is shown in Figure 10 which compares favorably with the ice layer model for the 10^{-4} ft. thickness. The remainder of the calculations use the simpler model for convenience.

Repetitive calculations of the type just mentioned are not necessary to determine evaporation times of arbitrary sized particles. Rather the time to evaporation is a function which may be calculated in the mathematically equivalent condensing situation in which the layer builds up to a certain thickness in a certain time. The only parameter is that of

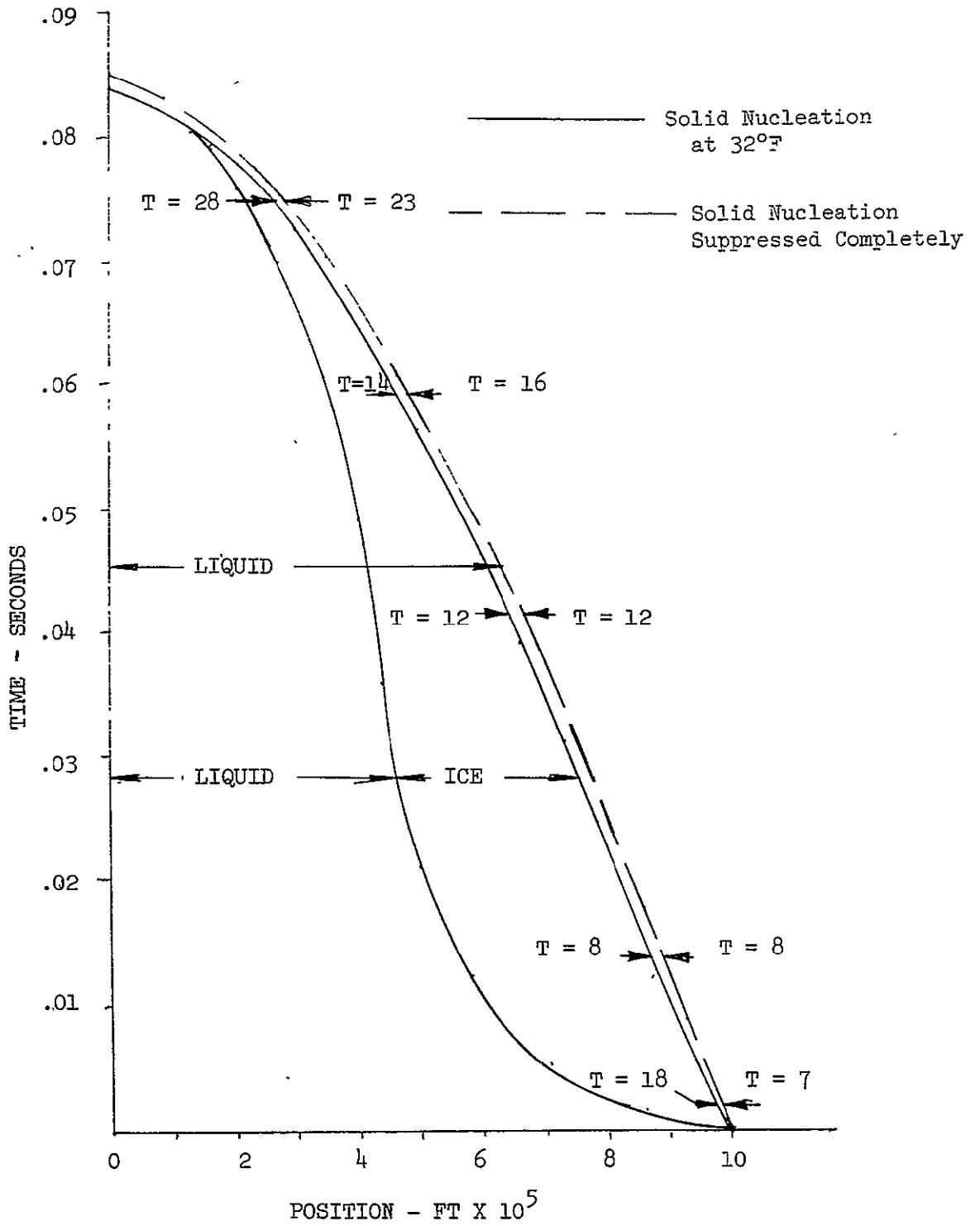


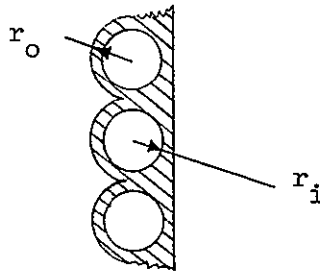
FIGURE 10 PHASE-POSITION HISTORY FOR A .0001 FT. THICK DROPLET
ON A 60 DEGREE F WALL IN A VACUUM

wall temperature as shown in Figure 11. The curve is actually a sub-parabola; i.e., time (thickness)ⁿ, 1 < n < 2. Since the supply rate was found to be a linear function of thickness, the thicker droplets result in a more marginal design.

The curves of evaporation time and supply time are superposed in Figures 12a, b, and c. The parameters of evaporator area and wall temperature are evidenced as is the droplet thickness. In wetting combinations of surface and evaporant the spattered drop size is expected to be about 10 times as large as the impinging droplet size, such that the thickness is very slight. In cases where wetting is not achieved well, the diameter to thickness ratio is estimated to be about 6:1. Using this as a "worst case" to estimate the average droplet thickness, a ratio of thickness to original droplet diameter of 0.265 is achieved. For the 98 percentile droplet of Figure 4, the droplet thickness on the wall is thus 42.5 microns and the margin against accumulation is positive for evaporator areas greater than about 0.75, 0.2 and 1.5 ft² for H₂O, NH₃, and CHF₂Cl, respectively.

3.3.4 Transport Fluid Design

The transport fluid design is straightforward forced convection heat transfer. The design calculations herein are based on round tubes laid side by side without gaps as shown in the following sketch



Calculations have been made for (1) single tube series turbulent flow circuits and (2) laminar flow, with water; (3) single tube series turbulent flow and (4) multiple parallel tube turbulent flow, with Freon 21.

Heat transfer coefficients are based on the familiar developed flow equation

$$h = .023 \frac{K}{d_i} (Re_{di})^{.8} Pr^{1/3}$$

Pressure drops have been calculated from

$$\Delta P = \frac{.046}{(Re_{di})^{.2}} \frac{4L}{d_i} \frac{1}{2\rho} \left(\frac{\dot{w}}{A}\right)^2$$

The area for internal heat transfer is $\pi d_i L$, of which only a fraction is fully effective for heat transfer. Some preliminary calculations

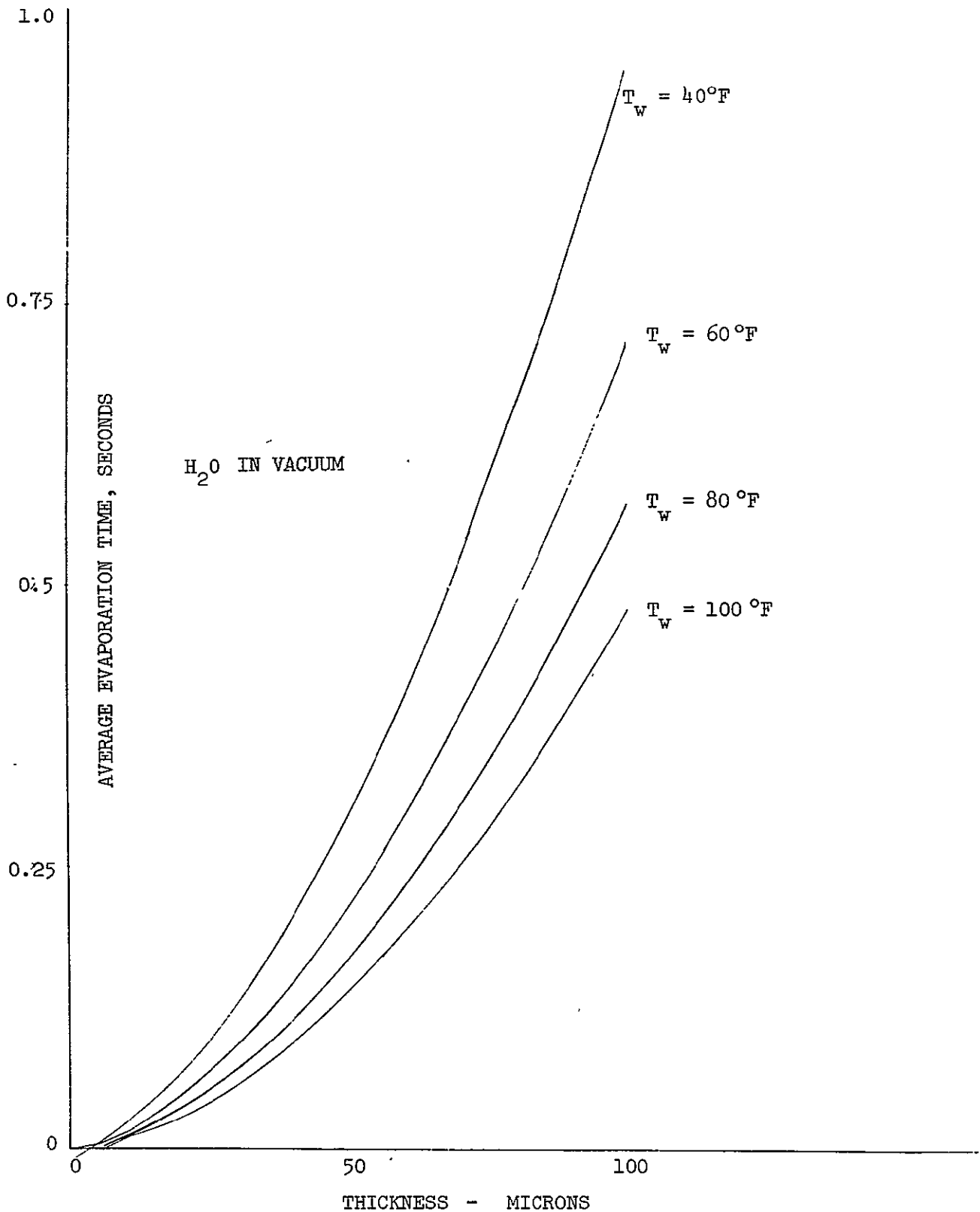


FIGURE 11 VARIATION OF EVAPORATION TIME WITH THICKNESS AND WALL TEMPERATURE

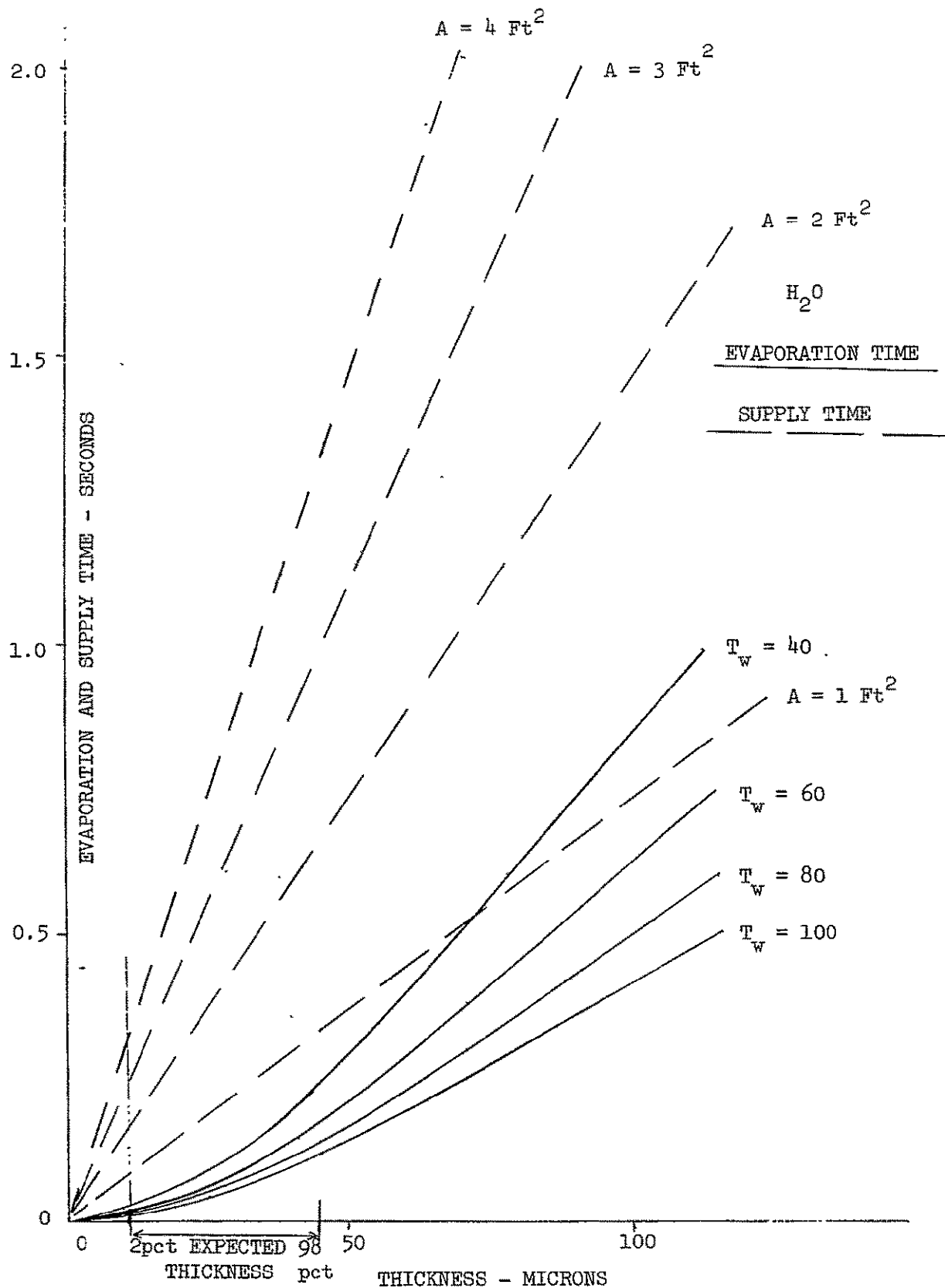


FIGURE 12a. EVAPORATION AND SUPPLY TIMES FOR WATER

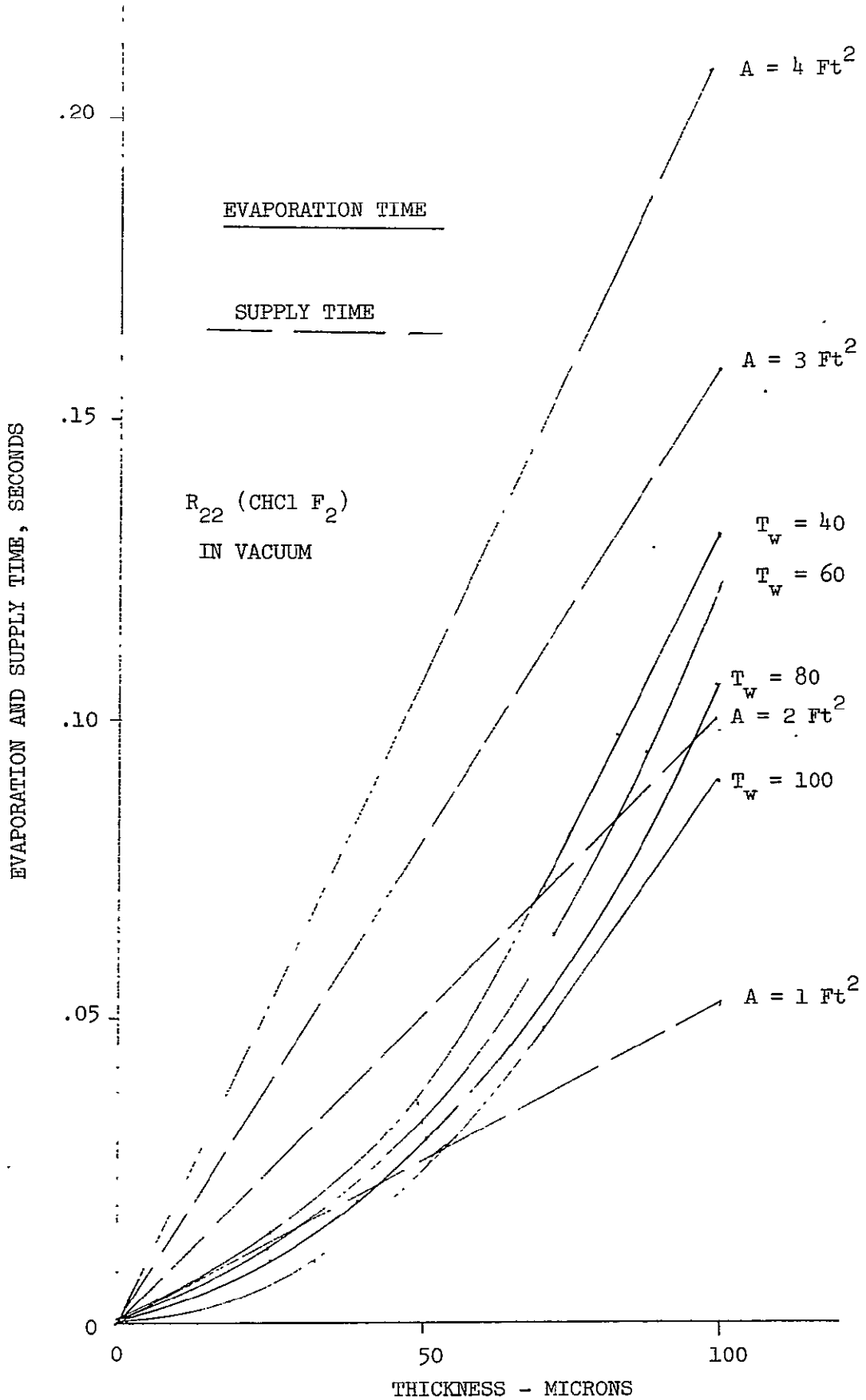


FIGURE 12B EVAPORATION AND SUPPLY TIMES FOR FREON 22

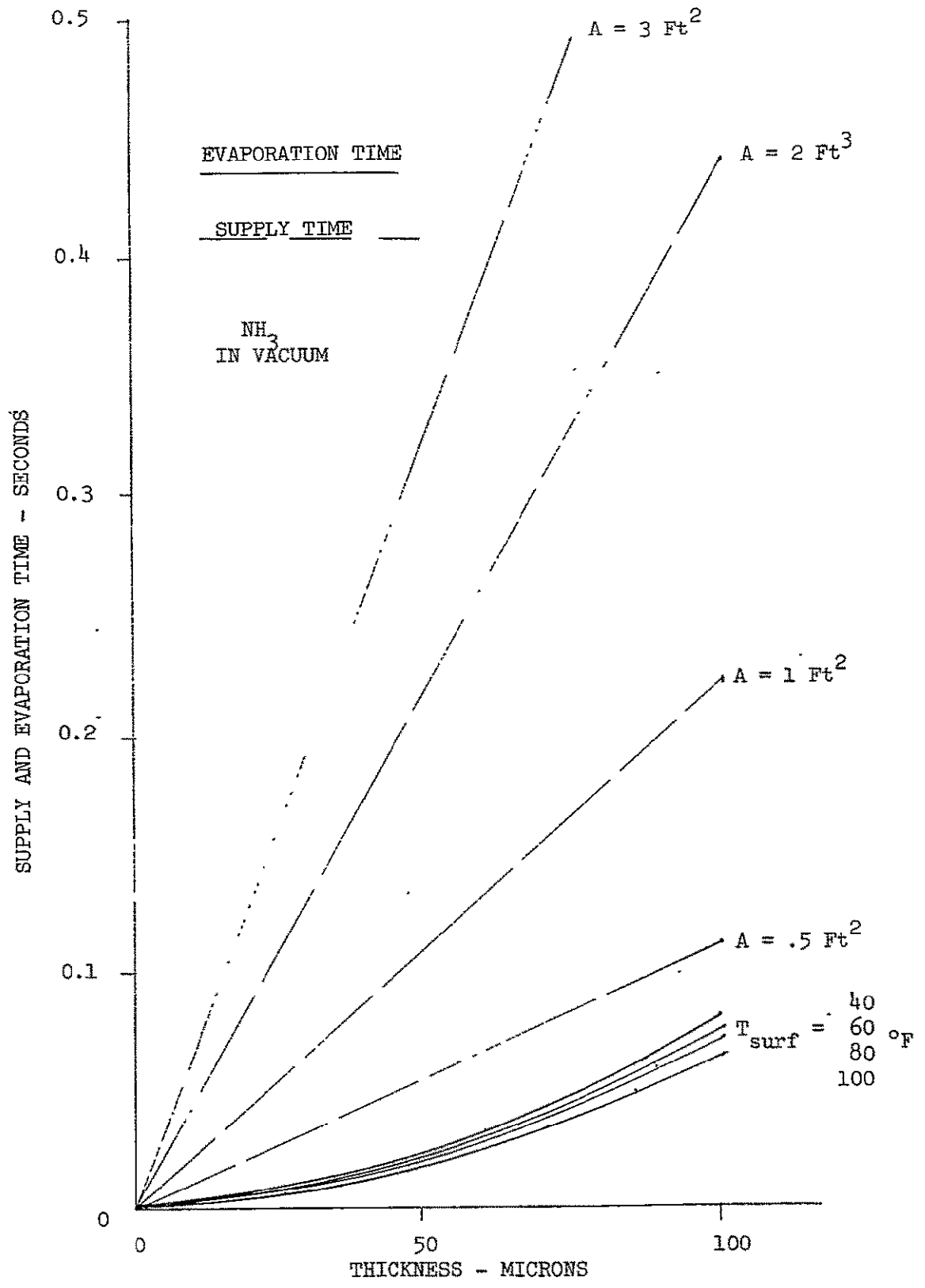


FIGURE 12C EVAPORATION AND SUPPLY TIMES FOR AMMONIA

indicate that (1) the wall conduction loss (for aluminum or better conductors) is not large and (2) the effective heat transfer area approximates dL which is the active evaporator area. The length of tubing is calculated from A/d for the pressure drop estimates and will be larger in the application since an additional tube length will be associated with the evaporator than that which just covers the active surface.

The wall temperature is less than the bulk fluid temperature by the amount

$$T_f - T_w = \frac{Q}{hA}$$

Figure 13 shows the value of pressure drop and temperature difference for the series turbulent flow of water through the device. In general the temperature drop decreases as the area increases while the pressure drop increases.

It is probably not possible to obtain multi-tube turbulent flow with water at the anticipated flow rates. However, the use of laminar flow in many channels is considered. In this event the pressure drop should be quite low. Exact results for developing laminar flow in non-round channels is generally not available. The typical curves of $StPr^{2/3}$ vs Re as in heat exchanger measured data do not present the required local heat transfer coefficient, but rather the mean coefficient. A word concerning the need for the local coefficient will be presented shortly. Typical curves of the local heat transfer coefficient in terms of Nusselt number are found for example in Kays (Reference 9). These data show that the developed and minimum Nusselt number is about 4 while close to thermal entry positions it may attain 20. To equal the turbulent flow coefficients shown of about $1000 \text{ Btu/hr-ft}^2\text{-}^\circ\text{F}$, the value of hydraulic diameter must be as shown in the following table.

<u>Case</u>	<u>d_h Required for $h = 1000$ with H_2O</u>
Max (Nu = 20)	.072 inch
Min (Nu = 4)	.014 inch

These hydraulic diameters imply passages which are less than their dimension. It is difficult to achieve excellent control while manufacturing extremely small passages and these passages will promote clogging at some condition. The significant observation is that reductions in area may only be obtained with highly effective heat transport surfaces. The surfaces will need effective fins and small passages to provide evaporator size reductions with laminar flow.

Figure 14 shows the results of single tube turbulent flow with Freon 21. The obvious difference in the Freon and water designs is the necessity of using larger tubes and generally larger evaporators. In contrast with water, the Freon flow rate is high enough to support turbulent flow in parallel circuits. Results for 2, 4, 8, 12, 16, 20, and 24 tube

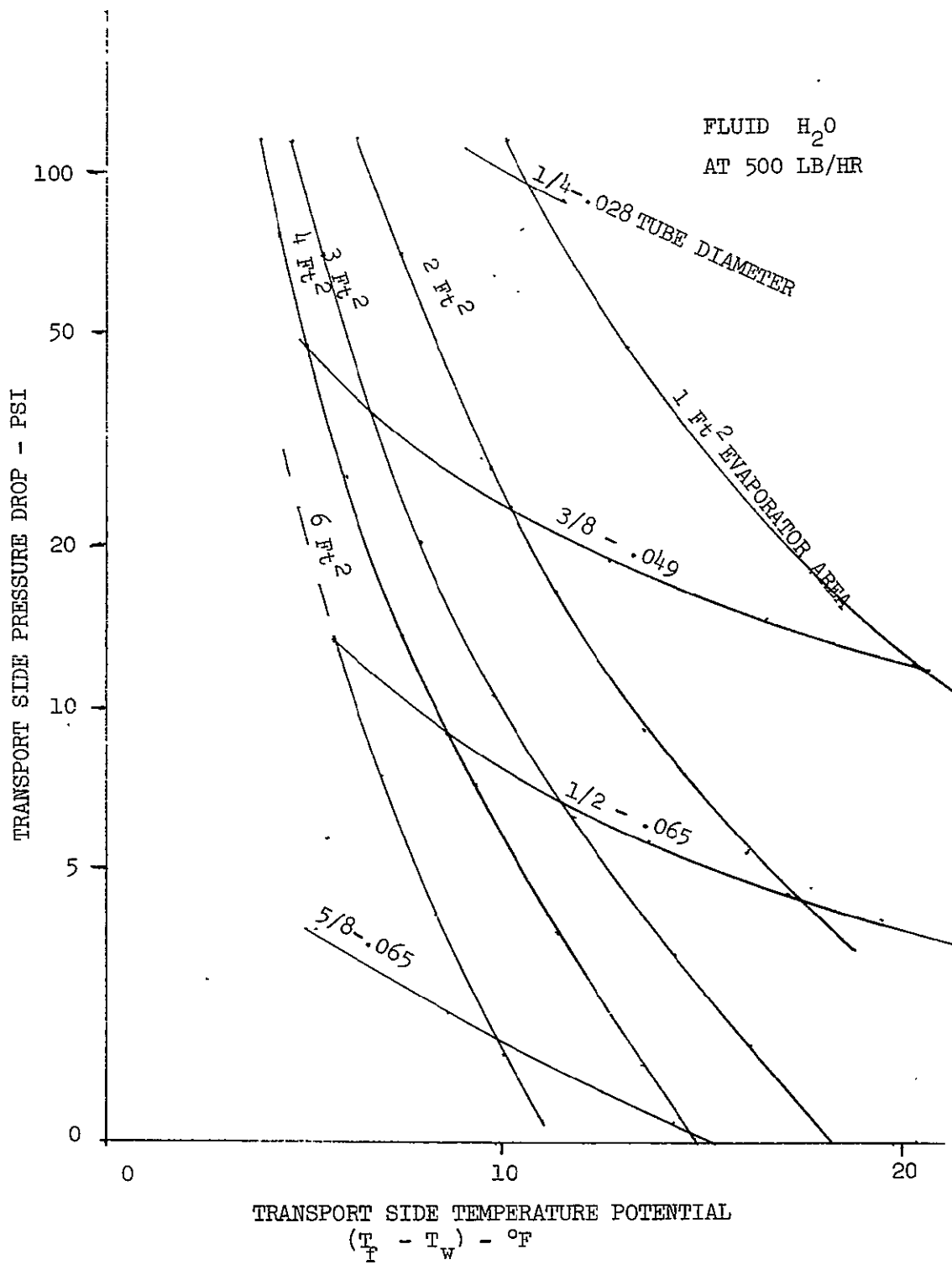


FIGURE 13 TRANSPORT SIDE PRESSURE AND TEMPERATURE CHARACTERISTICS

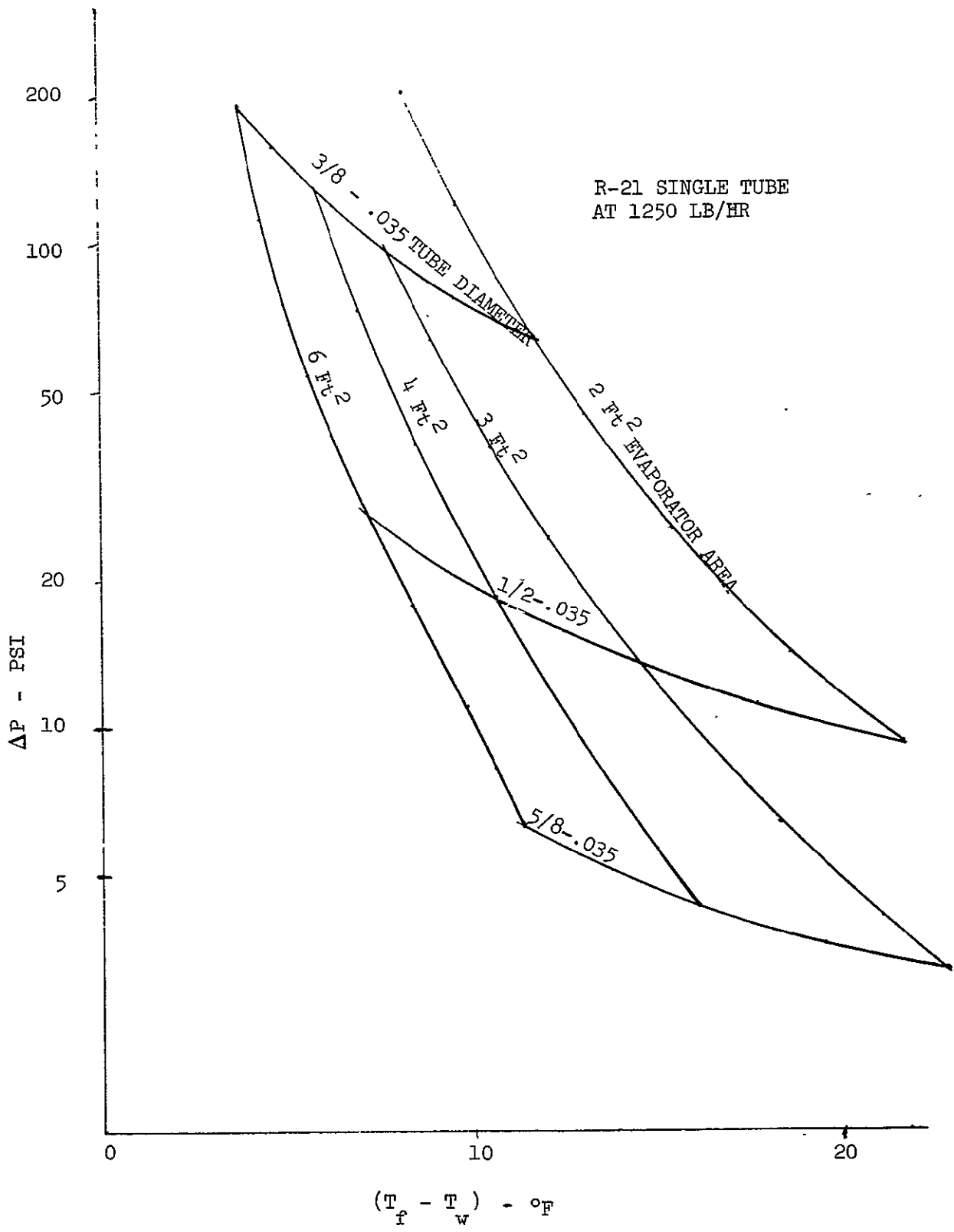


FIGURE 14 TRANSPORT SIDE PRESSURE AND TEMPERATURE CHARACTERISTICS

systems have been analyzed. The 16-tube results are shown in Figure 15 for example. As can be seen the design is better, achieving lower pressure drops and areas within the same temperature difference levels.

From the results of the multi-tube analysis a single condition of $\Delta P = 5$ psi and $\Delta T = 10^\circ\text{F}$ results in an area requirement which varies with the number of tubes. This relation is shown in Figure 16. It is clear that increasing the number of tubes permits lowering the area of the evaporator with a plateau reached at about 20 tubes. Further addition to the number of tubes does not permit additional area decrease. One effect not taken into account is the gradual tendency of the effective heat transfer area to grow as the tube diameter decreases. At the point of diminishing returns, the evaporator size is roughly the same as for water as fluid and a decrease below 4 ft^2 will require a geometrical passage change to raise the heat transfer coefficient or the amount or effectiveness of the fin.

At this point a consideration of some facets of the transport fluid design is interjected. The area of the evaporator is effectively controlled by the transport fluid channel design, since the margin against spray accumulation is approximately 400% at an area of 4 ft^2 .

The minimum heat transfer coefficient has been used to characterize the transport fluid surface. This is because the lowest wall temperature is the point at which either water as transport fluid tends to freeze or flooding of the surface is most likely for any transport fluid. The wall temperature will be lowest where the combination of parameters evaporant supply rate, heat transfer coefficient and bulk temperatures combine at their worst condition. This condition may be reached at almost any point in the evaporator at low load conditions and will be affected by spray density variations from average of an unknown amount and by heat transfer coefficient variations. In typical heat exchanger surfaces the minimum heat transfer coefficient occurs near the outlet and may only be a small fraction of the surface-averaged value.

The aforementioned variation in spray deposition rate is partly possible to aid by selection of the surface shape so that higher deposition is allowed only at the higher temperature inlet sections. This is not a good practice entirely since the control mode may be such that all positions in the evaporator are equally sensitive at certain times during its operation. For example in pulse mode control (off-on) and inlet temperature 47 degrees (just on the operational threshold) the response of nearly all the evaporator will be in proportion to the local spray deposition and heat transfer coefficient, and will not be affected by proximity to the inlet or outlet.

3.4 Control Schemes

Several control schemes have been considered for the flash evaporator. These control schemes are used to automatically match the evaporation rate to the heat load. The requirement is to deliver the

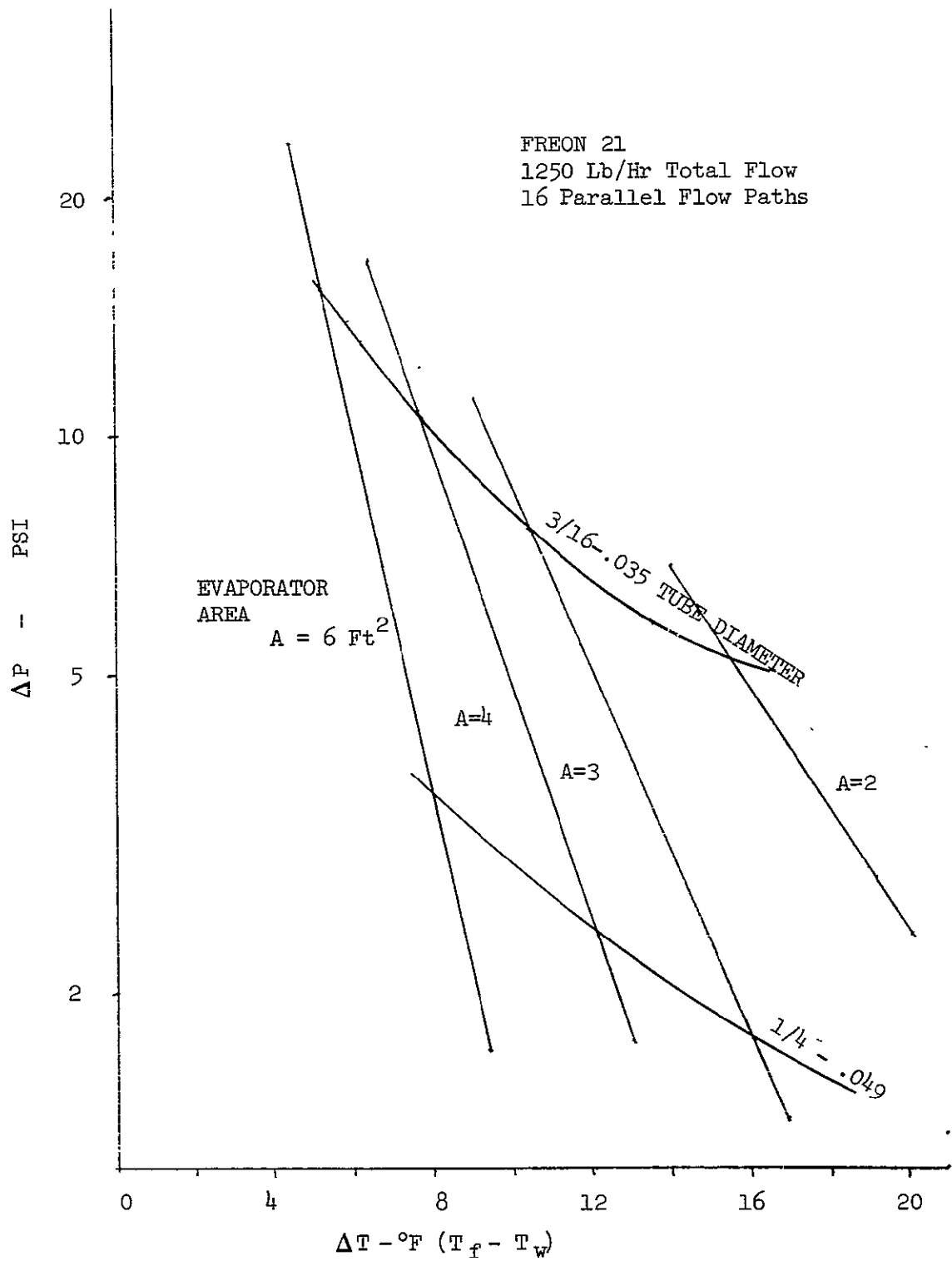


FIGURE 15 SIXTEEN PARALLEL FLOW PATH RESULTS WITH FREON 21
 TRANSPORT FLUID

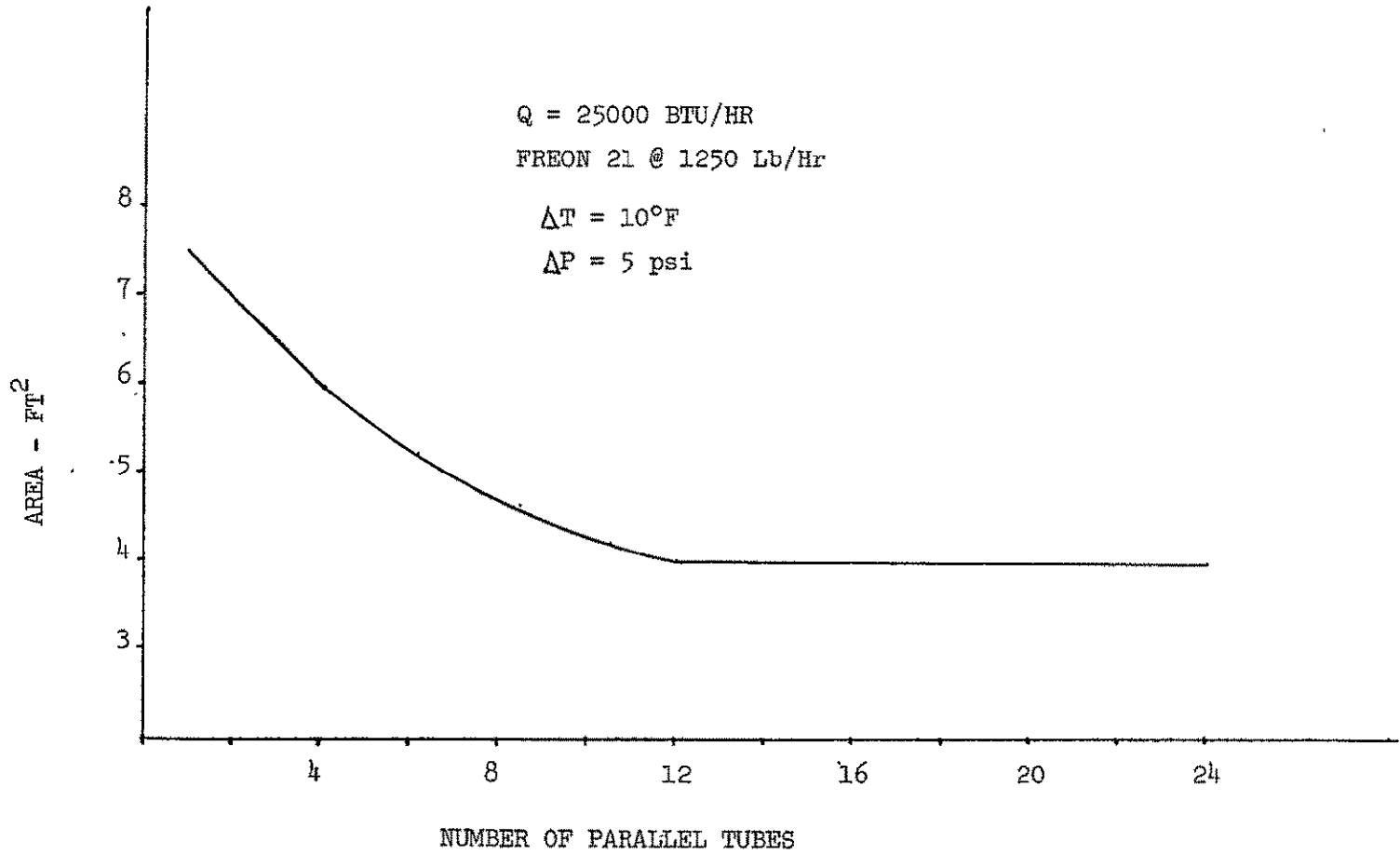


FIGURE 16 AREA REQUIRED WITH VARIOUS TUBE NUMBERS

transport fluid within a definite temperature range which is herein specified as 35 to 45°F. The table below illustrates several control schemes which have been considered.

CONTROL MODE	OPERATING PRINCIPAL	REMARKS; ADVANTAGES
Off-On	Turns evaporant flow on and off according to a selected transport fluid system temperature.	Simplest system. Will incur difficulties with non-uniform cooling. Cyclic rate fairly high.
Proportional Control	Evaporant flow is modulated in magnitude to achieve a selected transport fluid system temperature.	Common type of system. Limited range of evaporant flow is achievable. More limited range is available without outlet hole size control (back pressure control).
"Organ Pipe"	The total capacity of the evaporator is divided into several smaller units. These units turn on to maintain system outlet temperature.	Eliminates overshoot in outlet temperature. Minimizes number of cycles. Will probably result in increased manufacturing costs. Is easily modularized.
Calculated Pulse Rate	Predetermined pulse rate according to sensed requirement.	Eliminates overshoot at expense of some electronic complexity.

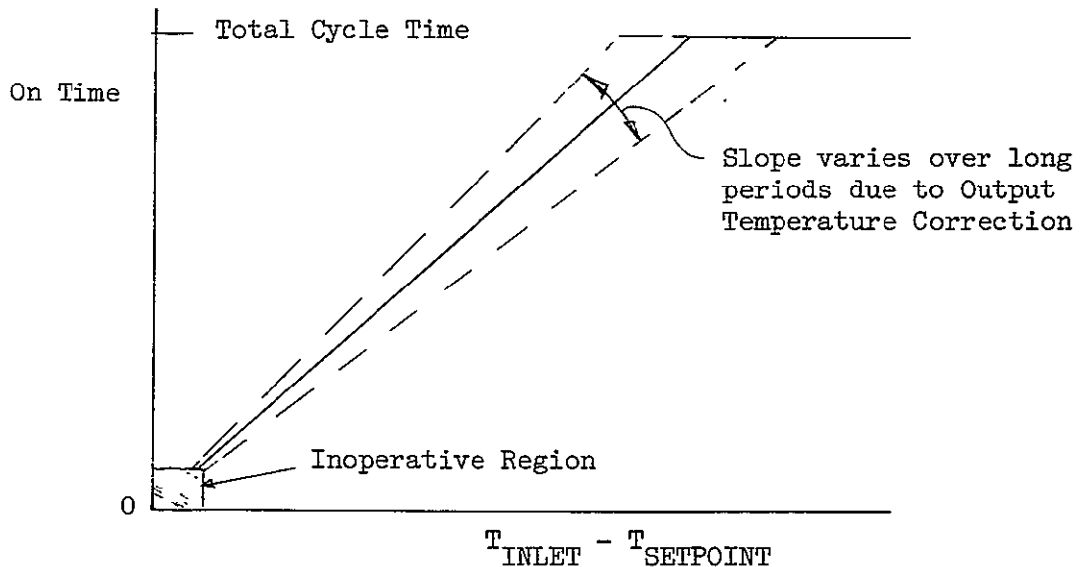
The off-on control is familiar, having the evaporant supply on if the controlling sensor is above a temperature T_{high} and off if the sensor falls below a temperature T_{low} ; $T_{high} > T_{low}$. The fluid flow is expected to cycle to provide the imposed heat load whenever the latter is less than the design heat load. The important characteristics of the control system are: (1) thermal overshoot at the outlet, (2) cyclic rate, and (3) response capability. In addition, when water is the transport fluid, the extreme low temperature excursion of the wall must be known.

The proportional control scheme allows for a continuously variable spray rate with at most a coarse type of back pressure control. The outlet temperature can in principle be controlled to within an arbitrarily close range. Problems associated with this method are that of varying supply pressure (or varying flow by another method) and maintaining the back pressure during spray variation to within an acceptable range. These problems are estimated to be sufficient to discourage its use.

The "organ pipe" control scheme is described as follows for a six evaporator design. Each evaporator is allotted 1/6 of the heat load. The number of evaporators is chosen to yield the result that the temperature change due to one evaporator's effect is less than the control band. The outlet temperature of the entire assembly is monitored, and whenever it falls below T_{min} , one evaporator is turned on. It is necessary to install a time lag so that the effect of one action is allowed to propagate to the sensor before initiating a second action.

The "organ pipe" scheme offers several advantages and several disadvantages. The probability of a single failure grows as the number of evaporators increases. Even so the joint probability that any five of eight units will operate far exceeds the probability that one of one operates. The ability to achieve the equivalent reliability of redundant, full-sized units may be accomplished with 8 or 9 one-sixth full load units. Obviously this is accompanied by a weight savings which may be of significance. On the other hand, the increased number of items required is expected to result in an increased price.

Finally a calculated pulse rate control scheme is one illustrated schematically below.



In this scheme, the on and off times are determined beforehand using a fixed total time and an on time which is a function of load. The on time increases in proportion to $(T_{\text{inlet}} - T_{\text{setpoint}})$ with the proportionality constant adjustable over a limited range by a survey of the outlet temperature. The proportionality constant change must be accomplished over long time periods because it is not intended to function as a primary control but rather adjusts for flow rate and other system tolerances.

3.5 Design of Configuration

It is desired to configure a concept which allows for the operation of the device as outlined theoretically and experimentally in the foregoing sections. In addition the concept is desired to display easy fabricability and provide for integration into the space shuttle. The transport fluid characteristics already have indicated that about 4 ft² of active area is required.

3.5.1 Liquid Spray Devices

There are several liquid spray devices which are available. The principal axisymmetric types of spray nozzle are straight, full conical, and hollow conical. Other types include pneumatic atomizing nozzles and

flattened spray nozzles which employ an object in the flow to initiate spreading. The straight nozzle consists of a straight orifice with non-swirling flow and produces a stream which breaks up at a certain distance from the nozzle into a fan of spray droplets. The full conical nozzle presents a moderate rate wheel-type rotation to the nozzle orifice. Since the angular momentum of the fluid particles vary from zero to some maximum amount, the spread of fluid occurs within a full cone. The hollow cone nozzle is formed due to a free vortex of high rotation rate generated upstream of the nozzle orifice. In this situation the liquid forms a conical liquid sheet which breaks up to form droplets.

Droplet sizes for the various nozzle types are dependent on the type of nozzle, flow conditions fluid properties, and upon the ambient condition of the spray-receiving volume. A considerable amount of effort has been expended to determine the drop size distribution of sprays in fuel injection systems. Reference 10, for example, gives typical distributions which have been deduced to correlate experimental data. A list is provided below which enumerates the axis positions in the matrix of conditions which represents all situations.

1. Type of nozzle (straight, full conical, hollow conical, flat, gas atomized).
2. Flow conditions (supply pressure, dissolved gases, relation of ambient to vapor pressure).
3. Fluid properties (non-dimensional surface tension (Weber Number), viscosity (Reynolds Number)).
4. Ambient condition (back pressure, external fluid velocity)

The conditions at which these have been evaluated are numerous but do not exhaust the possible matrix. Fuel injection research has explored the various types of nozzles with numerous external fluid velocity conditions. Some of this work has been carefully measured and documented while much of it has been directed toward development of devices and is stored largely as engineering experience. Some recent research has been directed to the study of liquid injection into a vacuum environment. References 5, 6, and 11 all report various nozzle configurations spraying into a vacuum environment. These investigations have centered on determining the effect of the low back pressure on the nozzle flow phenomena. Notable absences of data exist in the areas of vacuum effects on droplet size variation on flow distribution in the spray.

References 5 and 6 report a preliminary agreement of droplet size in vacuum with those expected in atmospheric environment. The mode of breakup is that of an instability due to surface tension on an extended cylinder of fluid. Such an instability results in a preferred wavelength for breakup and pertains only to the straight nozzle flow. Reference 10 gives the following expression for the wavelength.

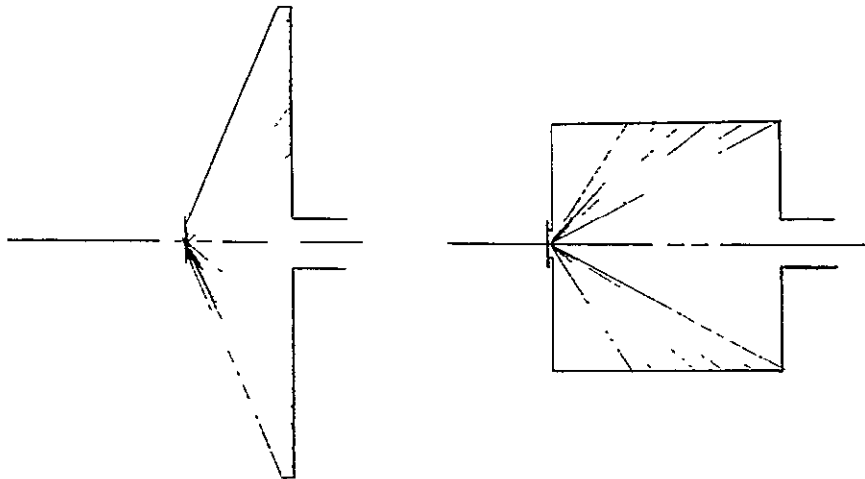
$$\frac{\ell}{d} = \sqrt{2} \pi \left[1 + \left(\frac{2\mu}{\sigma d} \right)^2 \right]^{\frac{1}{2}} \frac{1}{2}$$

The dimensionless ratio $\mu^2/\rho d$ is normally very small for liquids of interest such that $\ell/d = 4.45$ results. Here ℓ is the preferred wavelength of instability and d is the fluid cylinder diameter which is assumed to break into lengths ℓ . The volume of fluid is $(\pi/4)d^2\ell$ which forms a spherical droplet of volume $\pi/6D^3$, yielding equal volumes at $D/d = 1.88$. Droplets whose diameter is approximately twice that of their parent orifice are commonly reported for the full jet type nozzle sprayed at atmospheric pressure as well as the straight nozzles in vacuum conditions. For the hollow cone spray patterns, however, the drop sizes are normally much smaller. In these hollow cone devices, the liquid forms a conical sheet which thins toward the edge, but tends to develop thickened strands or ligaments embedded in the sheet. At some distance from the orifice, the sheet breaks up along a ragged edge with the ligaments forming droplets. These droplets are quite small, hence this type of nozzle is sometimes called a "pressure atomizing" nozzle.

As an example of the droplet size distribution which is attained in pertinent circumstances, consider the distributions of Figures 8 and 17. These distributions are valid for water spraying into air at atmospheric pressure, but are considered to be representative of vacuum results since the dominant droplet breakup mode does not involve air resistance. As is shown, the full conical spray size is larger than that of the hollow cone spray by a considerable margin. This spray size affects both freezing times and evaporation times and thus may affect the design of a spray evaporator.

3.5.2 Evaporator Shape and Size

The basic cylindrical design and the plate design sketched below were considered to fulfill the requirements imposed on the design.



The active surface of these configurations is shown resulting from the anticipated spray deposition patterns.

(41)

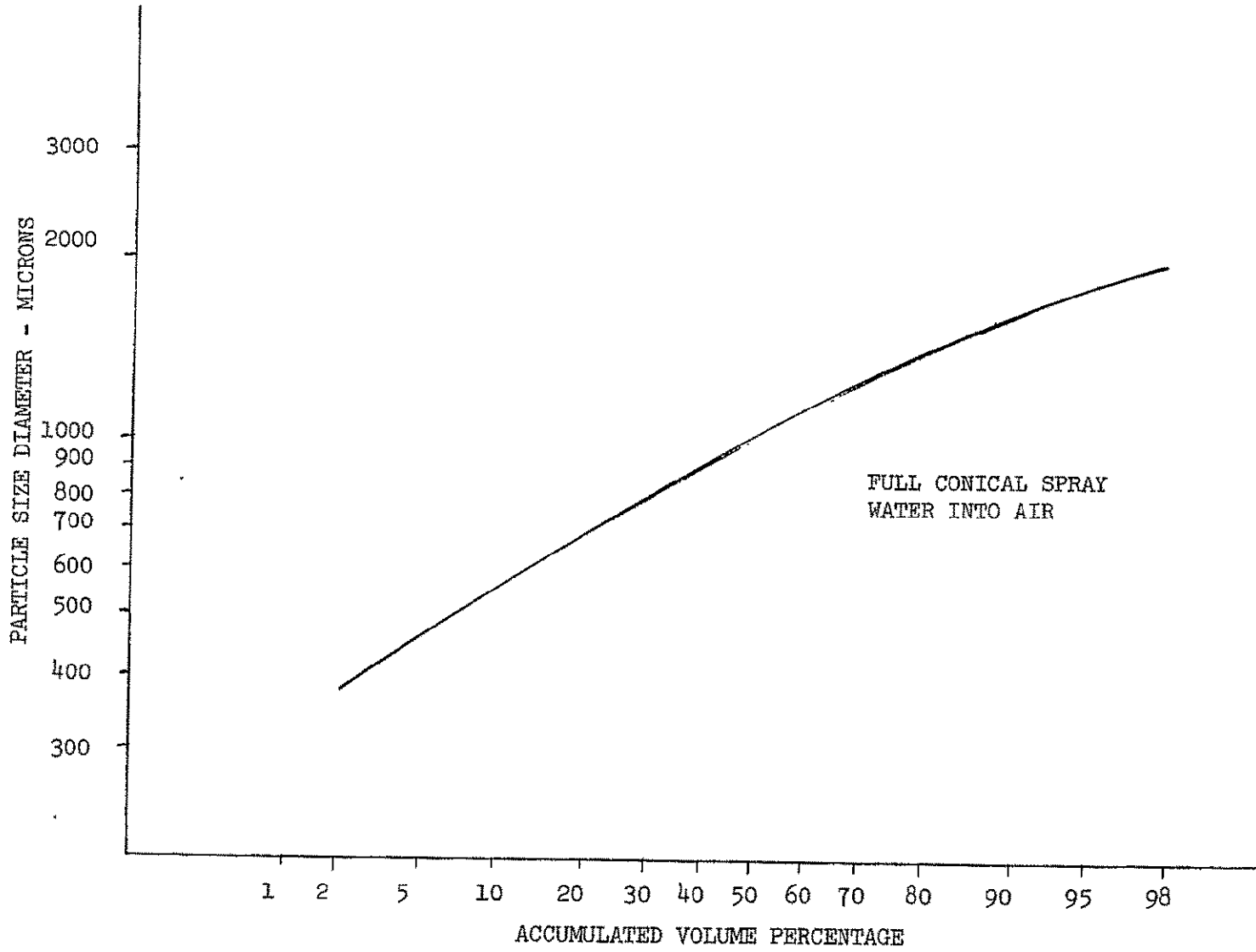
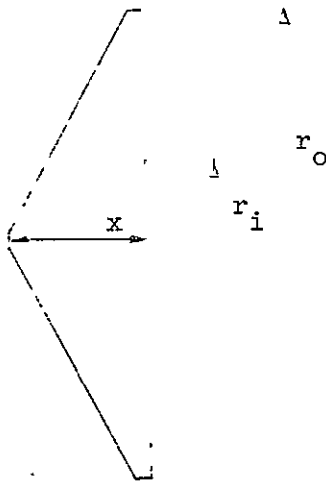


FIGURE 17 PARTICLE SIZE DISTRIBUTION IN FULL CONE SPRAY

The water active wetted area was selected to size the evaporators since the other evaporants can tolerate the lower wall temperatures dictated by higher flow densities. For this purpose the spray limits observed during preliminary testing were employed. These limits are an inner cone of 30 degrees and an outer cone of 60 degrees from nozzle axis. Setting the sizes to achieve a 4 ft² evaporator active area results in the dimensions shown below.

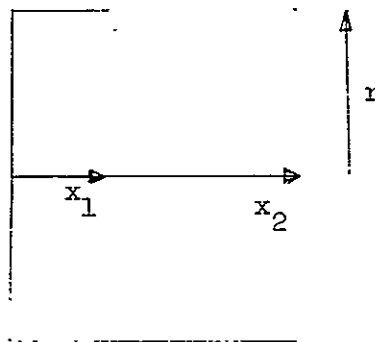
$$A = \pi (r_o^2 - r_i^2)$$

$$\begin{aligned} x &= 8.0'' \\ r_o &= 13.5'' \\ r_i &= 4.5'' \end{aligned}$$



$$A = 2\pi r(x_2 - x_1)$$

$$\begin{aligned} r &= 9'' \\ x_2 &= 15.5'' \\ x_1 &= 5.5'' \end{aligned}$$



These two configurations allow for different variations of flow within the hollow cone. If the flow is heavier toward the center, the cylinder will achieve more uniform cooling. If the flow is more dense toward the outer edge the plate will achieve more uniform flow. Otherwise there is little difference in the expected performance of the configurations. The plate evaporator will probably be easier to package within the space shuttle since it has considerably less depth. Also the total surface area of the plate configuration is less, such that it is favored from a weight standpoint.

3.5.3 Exit Vapor Port Sizing

There are other considerations in the conceptual design which are important. A later section will treat the control problem separately. Also the vapor vent line must be sized to allow most favorable operation. The density of NH₃ and Freon vapor will be greater than water vapor due

to the higher pressures during their operation. Therefore the size established for H₂O will accommodate these fluids as well. The first test (see 3.7) established the dependence of efficiency on the operating pressure. At pressures below .01 psia, evaporation efficiency is lowered and above .06 psia, the difference between wall temperature and saturation temperature is insufficient to preclude accumulation. Therefore operation between these pressures is desired. The vent will be choked whenever the chamber pressure is more than about twice the ambient pressure. At this condition, the vapor flow and pressure are related through the relation

$$\dot{w} = \frac{P \cdot A \cdot \text{Const}}{\sqrt{T}}$$

When the pressure is low, \dot{w} is about 70 percent of the injection flow rate and rises to 100 percent at higher pressures. An area A_{\min} can be defined in

$$0.70 \dot{w}_{\text{liq}} = P_{\min} A_{\min} \frac{\text{Const}}{\sqrt{T}}$$

This area insures that at the low pressures where low efficiency occurs, the pressure will rise to P_{\min} after steady operation is achieved. With such an area of vent the pressure will rise to P_{\max} when the higher efficiency is achieved.

$$P_{\max} = \frac{\dot{w}_{\text{liq}}}{A_{\min}} \frac{\sqrt{T}}{\text{Const.}} = \frac{1}{0.7} P_{\min} \quad (7)$$

If this P_{\max} is below the desired limit, the area is satisfactorily sized.

Actually the acceptable limit pressures are separated by more than the factor 1/0.7 so that considerable latitude can be exercised.

The characteristic evaporator pressure rise time may be approximated by calculating the mass of vapor in the volume divided by the flow rate. If this time is short compared to the length of flow duration in a pulse, only a slight loss in overall efficiency will be experienced. Indeed, pressure rise times of about 0.1 second are anticipated so that pulses of a few seconds duration should yield nearly no net effect of efficiency loss during start up of the process.

Both of the concepts have been shaped assuming the spray to be the hollow cone pattern between 30 and 60 degrees from nozzle axis. This conforms to the observed H₂O spray envelope in the first test and to available devices for NH₃ and R-22. These latter fluids have a similar flooding tendencies as has been shown, but also have a considerable amount of liquid which becomes effectively vapor driven thus distorting the spray. These effects are difficult to analyze so that the test will be used to demonstrate their resolution.

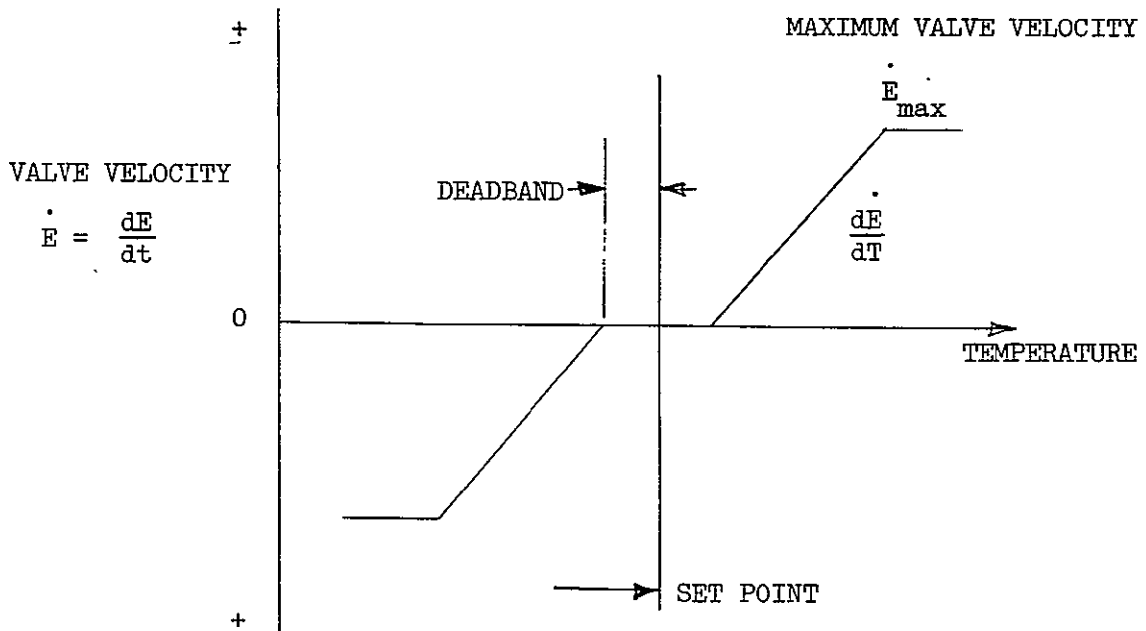
3.6 Thermal Model Development

A thermal model of the evaporator was constructed to aid in data analysis, project test results, and perform parametric studies. The features which were deemed most important about the model are the consistency of velocity and thermal propagation rates, a reasonable model of the evaporation process, and the capability to supply various control modes. These requirements led to the selection of CINDA (Chrysler Improved Numerical Differencing Analyzer) as the most attractive program. This program can integrate any of its internal subprograms with newly supplied subprograms to generate a particular program. VMSC is currently developing a new program for thermal analysis which incorporates many of the desirable features of CINDA and other programs with VMSC innovations. However, this program was insufficiently developed to assist in the current effort. Subprograms were developed for the control logic required, and for the evaporation model. Finite difference nodal models for five different situations were constructed and will be individually reported.

3.6.1 Control Models

1. Proportional Control Model

In this model the inputs are: valve initial position, set point temperature, dead band width, valve velocity slope per degree, maximum valve velocity, and control sensor identification. The output is simply valve position and results from a diagram of valve rate of change shown in the Figure below.



The position of the valve is projected to be $E_{(NEW)} = \frac{dE}{dt} (\Delta t) + E_{(OLD)}$. This position (E) then is used to modify a specified maximum flow rate such that $\dot{w} = E \cdot \dot{w}_{max}$. The response of the evaporator to changes in heat load may be increased by increasing the slope of the curve of $\frac{dE}{dt}$ versus sensor temperature. A maximum rate is allowed in the input data which usually is not reached in well designed systems.

2. Off-On Control

This type of control is straight-forward: the evaporant is turned "on" when the sensor temperature exceeds the top end of the control band and turns "off" when the sensor temperature falls below the bottom end of the control band. Only full on or off operation occurs; no fractional evaporant flow is sustained.

3. Organ-Pipe Control

This type of control was covered particularly in Section 3.4 where an account of its relative merits was included.

4. Dual Sensor Off-On Control

A dual sensor control simply incorporates two discriminating circuits, each having the authority to turn the evaporator off. Both sensors would be required to exceed their respective temperatures before "on" operation would be initiated.

3.6.2 Evaporation Models

The evaporation model incorporated herein is intended to be a complement to the control analysis rather than an evaporator design tool. A more elaborate model which would calculate the efficiency loss based on local conditions within an evaporator could be constructed. If this performance is based on analytical calculations it is unproven, and experimental performance data in sufficient detail have not been produced. The evaporation efficiency is intended by design to be as high as possible so that analysis would not predict any losses in normal operation. For this reason, the evaporation rates have been assumed to be of a form specified as a total liquid flow rate, an enthalpy of vaporization, and a node distribution pattern. The liquid flow rate is the product of $E \cdot \dot{w}_{max}$, where E is the spray fraction assigned by the control system and \dot{w}_{max} is the full open flow rate.

3.6.3 Flash Evaporator Thermal Models

Model 1 - Model 1 is a thermal model of the exploratory test item and resembles a tin can with one open end having a cylindrical section which is 12 inches in both length and O.D. It is constructed of 1/2 inch thick soft aluminum having the following assumed properties; (1) $\rho = 169 \text{ lbm/cu.ft.}$,

(2) $C_p = .208 \text{ Btu/lbm-}^\circ\text{F}$, and (3) $K = 118 \text{ Btu/hr-ft-}^\circ\text{F}$. The nodal breakdown for this thermal model evolved from attempts to conduct a transient thermal analysis on the test article from the first series of tests which were conducted in October 1970 and from the need to duplicate thermocouple placement on the test article (see Figure 18). Since there is no heat transport fluid in this model all nodes are of the solid diffusion type (i.e., have a positive capacitance and have the ability to store energy). There are 14 nodes, 11 along the cylindrical section, and 3 on the back plate (see Figure 19). The Appendix illustrates the required computer inputs for using this model.

Model 2 - Model 2 represents the test article used in the second series of lab tests. Figure 20 shows the nodal breakdown. The material properties used are for copper as follows $\rho = 558 \text{ lb/ft}^3$, $C = 0.091 \text{ Btu/lb-}^\circ\text{F}$, $K = 200 \text{ Btu/hr-ft-}^\circ\text{F}$, and water is the heat transport fluid. It was assumed that the loosely wrapped copper tubing was spaced 2 inches apart. Tube size for the model is $3/8$ inch throughout.

To gain insight into the role a flash evaporator would play in a total ECS, this model also includes a simple representation of radiator panels and an environment controlled cabin. Figure 21 shows the additional nodes required to represent the cabin and radiators. Physically, nodes 41, 42, 46, 47, 49, 52, 53, 56, and 57 are 10 foot lengths of $3/8$ inch O.D. copper tubing. Nodes 48 and 58 are 5 foot lengths of the same tubing. Nodes 43, 44, and 45 represent the cabin and are 10 inch lengths of pipe having a six inch O.D. and 3 inch I.D. These nodes are made purposely heavy to simulate the slow cabin thermal response. The material heat capacity was assumed to be $\rho C = 521 \text{ Btu/cu-ft-}^\circ\text{F}$. The radiators are represented by nodes 50, 51, 54, and 55. Each radiator was assumed to be constructed of aluminum ($C_p = .208 \text{ Btu/lbm-}^\circ\text{F}$) having an area of 130 ft^2 and $\epsilon = .9$.

The details of the node breakdown are indicated in the Appendix. Of note in the analysis is that the fluid throughput time is of the order of 1-5 seconds per typical node, while the "natural time increment" is generally shorter. This "natural time increment" is the stability limit for forward difference calculations, and is a reference point to compare the velocity and thermal propagation rates. In the case at hand the thermal time increment is less than the time step desired for most accurate velocity propagation. Therefore an implicit scheme was used (mid-difference or Crank Nicolson type) with time increment corresponding to the most accurate velocity calculations. This implicit scheme is unconditionally stable and results in accurate calculations based on the experience of the user.

Whenever a run of the evaporator alone is desired, an additional node is inserted immediately upstream of the evaporator node. This additional node can be prescribed a temperature-time relation and thus serves to allow a test type of inlet condition to be applied to the evaporator. This model has been used in the control system conceptual studies and parametric runs.

— Thermocouple Locations

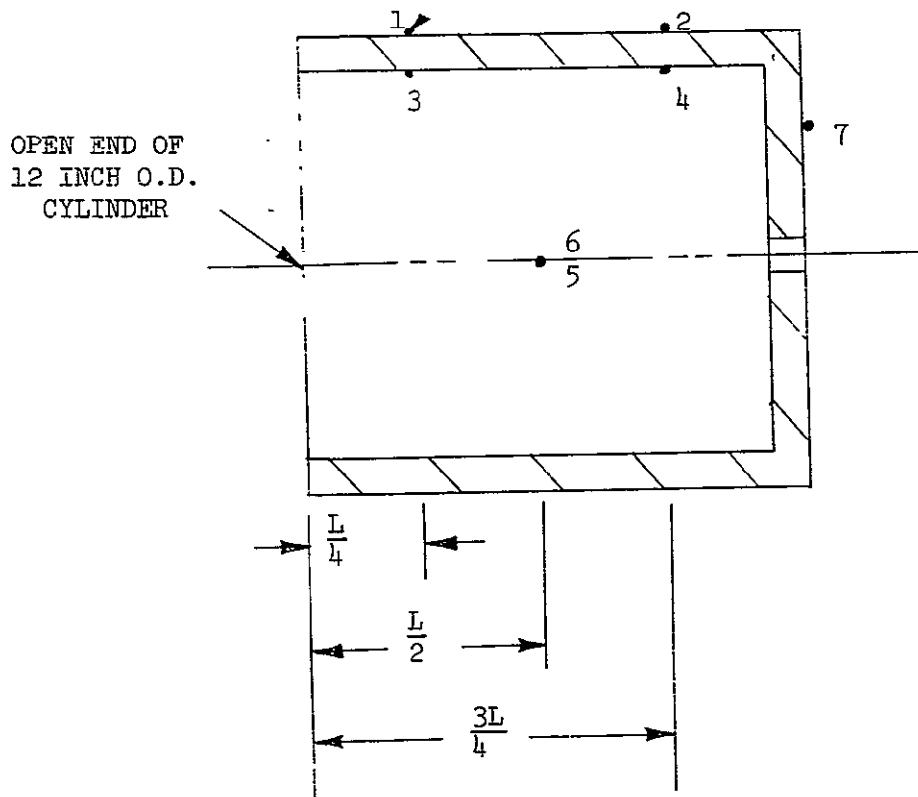


FIGURE 18 TEST ARTICLE SHOWING THERMOCOUPLE LOCATIONS

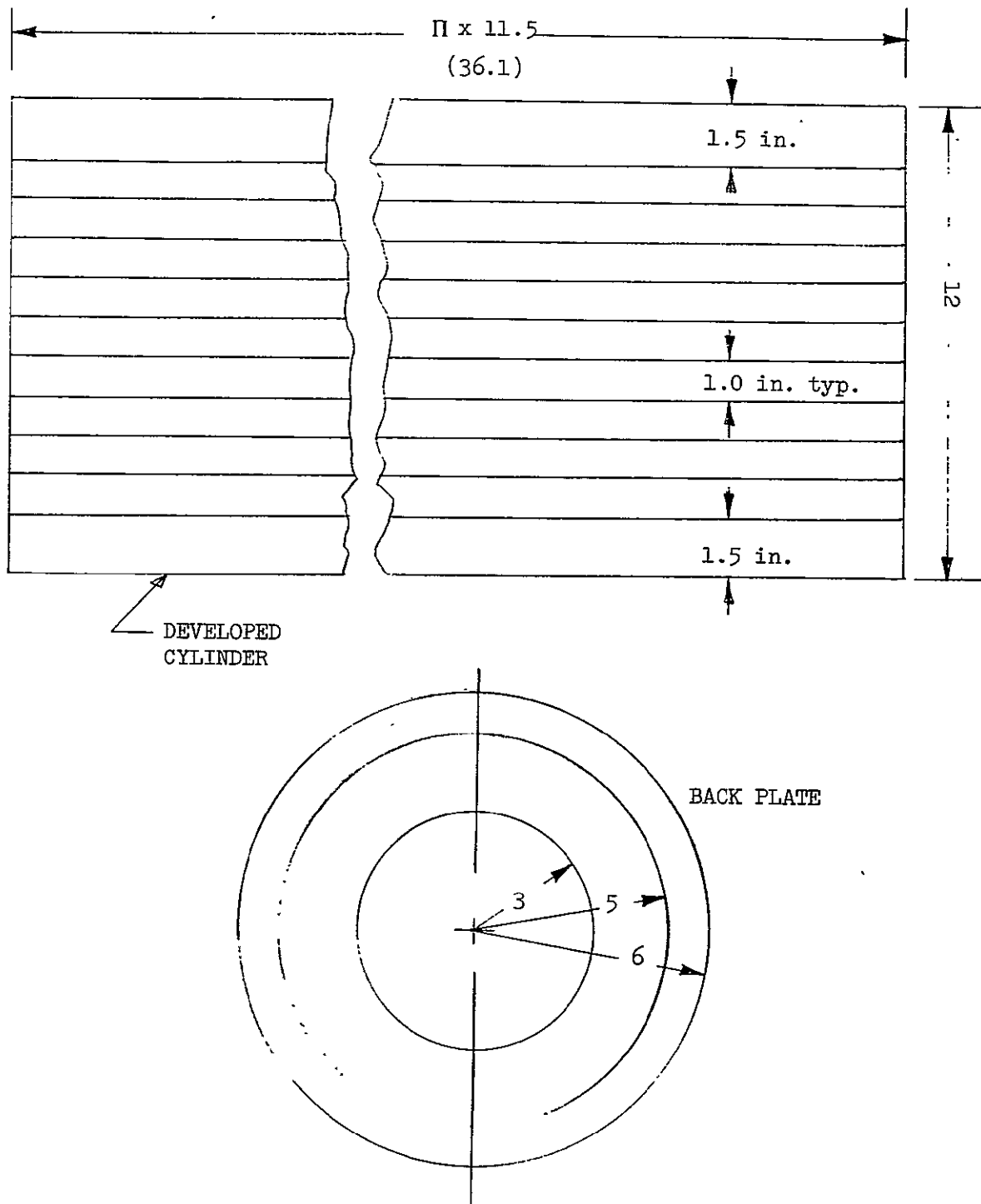
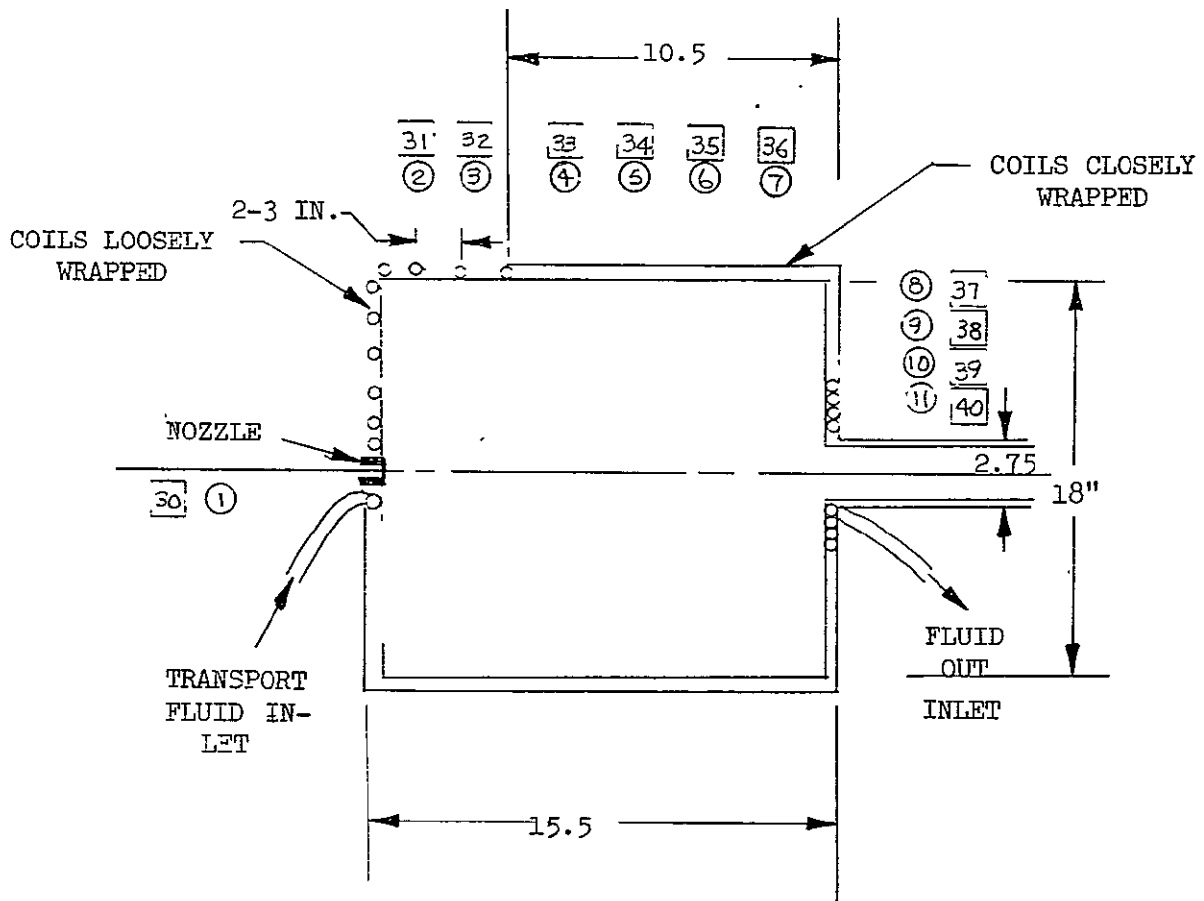


FIGURE 19 THERMAL MODEL DEVELOPMENT



- FLUID NODES
- STRUCTURE NODES

DURING THE TEST, THE FLUID FLOW WAS IN THE DIRECTION OPPOSITE TO THAT SHOWN

FIGURE 20 MODEL 2 AND 3 CYLINDRICAL EVAPORATOR DETAILS

(50)

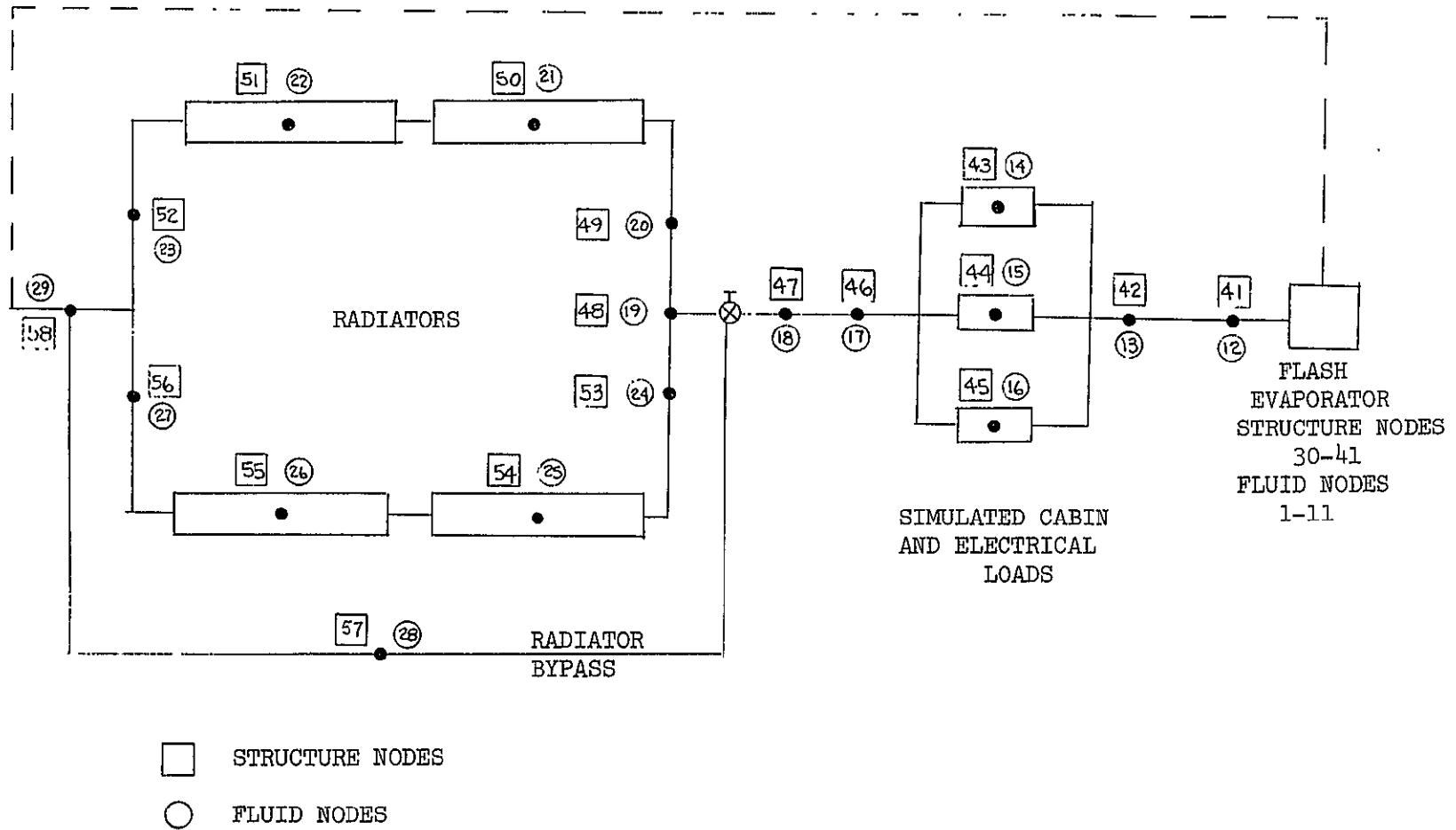


FIGURE 21 ECS SCHEMATIC WITH FLASH EVAPORATOR

Model 3 - Model 3 is for the most part identical to model 2 except that this model was sized to accommodate Freon 21 as the heat transport fluid. This was accomplished by increasing the diameter of the tubing to 5/8 inch. The number of nodes remains unchanged although the length of the nodes representing the flash evaporator did change somewhat. This results in a change in the throughput time and thus in the required calculation intervals.

3.6.4 Results

Model 1 - An attempt was made to duplicate the test results achieved with H₂O and NH₃ using this thermal model. The test data are taken from Reference 12. The evaporant heat of vaporization was determined from the following relationship

$$W_{\text{evaporator}} \cdot C_p \cdot \Delta T = W_{\text{evaporant}} \cdot \Delta h$$

The weights of the evaporator and expended evaporant along with the total temperature drop can be obtained from the test data. These values are for the water run #36

$$W_{\text{evaporator}} = 27.4 \text{ lbm}$$

$$W_{\text{evaporant}} = .19 \text{ lbm}$$

$$\Delta T = 30.5^\circ\text{F}$$

$$\text{Then, } \Delta h = \frac{(27.4)(.208)(30.5)}{.19} = 915 \text{ (Btu/lbm)}$$

The nodal breakdown which is illustrated in Figure 19 was achieved by a trial and error method through successive attempts to match test data and theoretical predictions.

Figures 22, 23, and 24 show the calculated effect of spreading the evaporant deposition over the first 5, 6, and 7 nodes. Figure 23 which shows evaporant deposition on nodes 1 through 6 gave the best correlation with the test data. It should be noted that the temperature histories from the test data lag about 10 seconds behind the theoretical predictions. This difference arises out of difficulty in determining time zero from the test data.

In a like manner, an attempt was made to duplicate the test results achieved with NH₃ on Run #44 of Reference 2. The heat of vaporization was calculated to be 435 (Btu/lbm). During this run in the lab a thick fog was produced within the evaporator. Consequently, it was realistic to divide the total evaporant flow rate into two deposition rates. Deposition rate #1 represents that part of the total flow rate which evaporated on first contact with the evaporator end plate. Deposition rate #2 represents that fraction of the total flow which was dispersed in a fog along the cylinder wall of the evaporator. At the present time the best correlation of test and theoretical results is shown in Figure 24. Deposition rate #2 accounts for 15% of the total evaporant flow which is proportioned over cylinder nodes 1 through 7. Proportionately, nodes 5 through 7 have twice as much deposition as nodes 1 through 4.

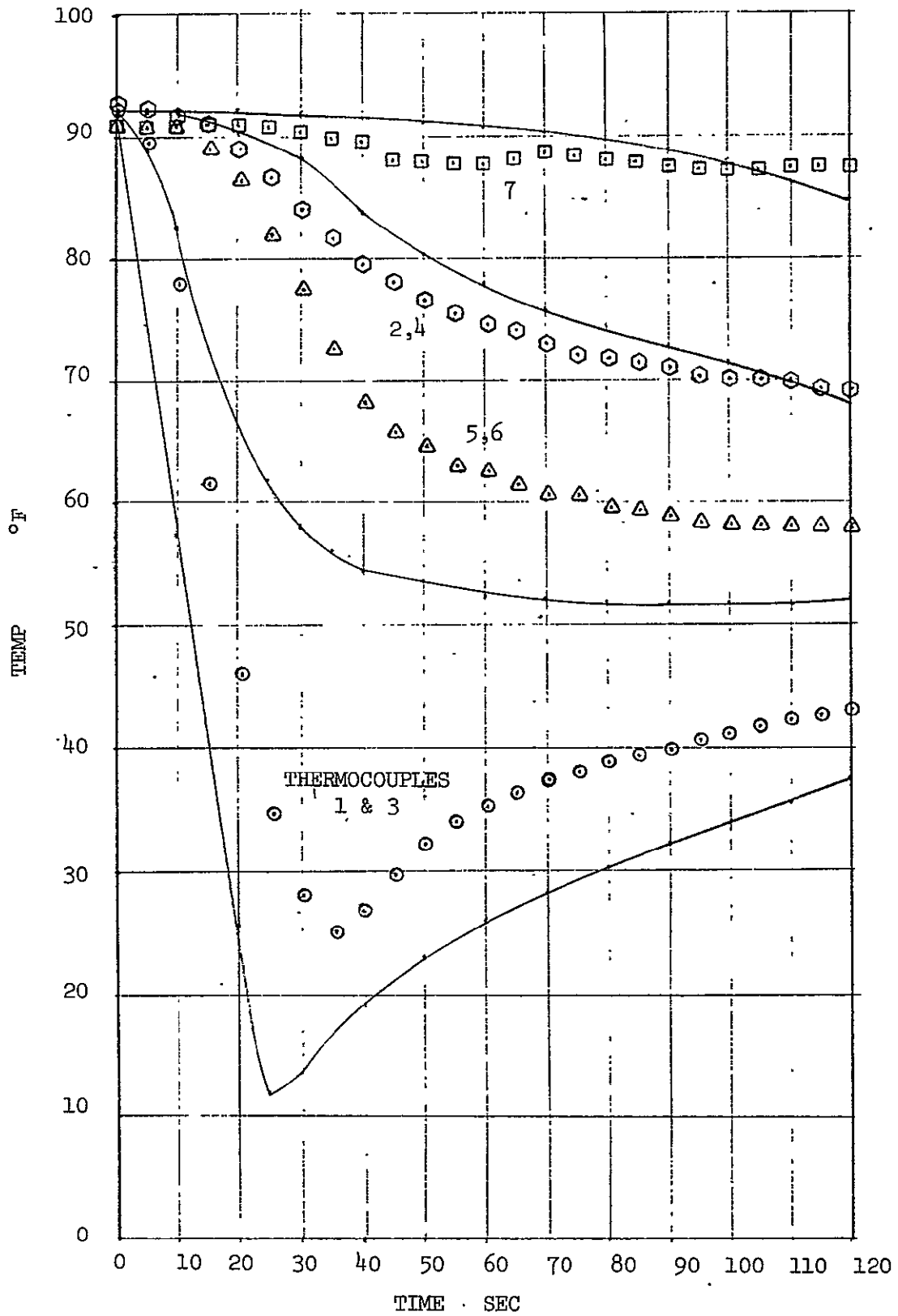


FIGURE 22 EVAPORANT DEPOSITION ON THE FIRST FIVE NODES

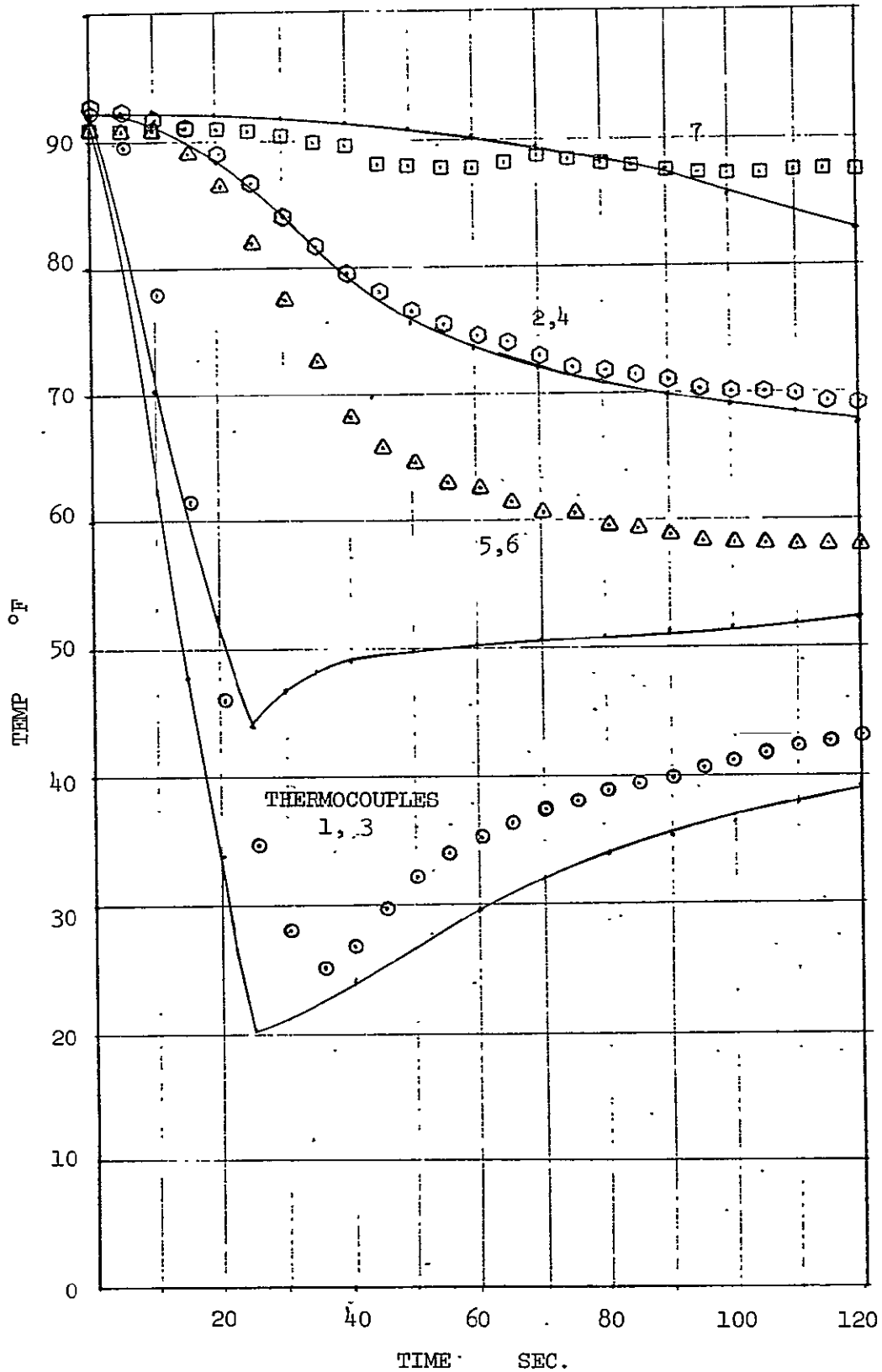


FIGURE 23 EVAPORANT DEPOSITION ON FIRST SIX NODES

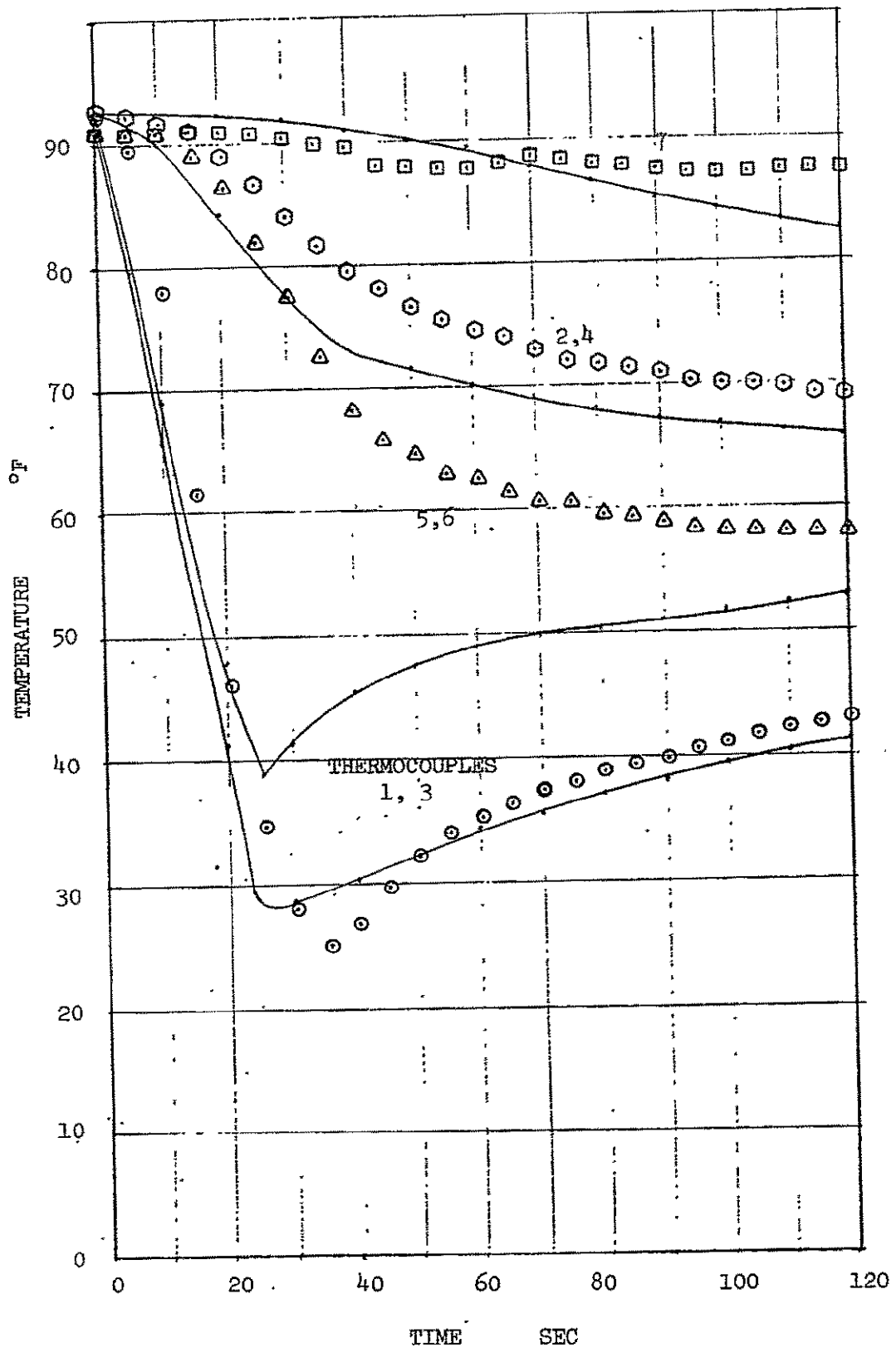


FIGURE 24 EVAPORANT DEPOSITION ON THE FIRST SEVEN NODES

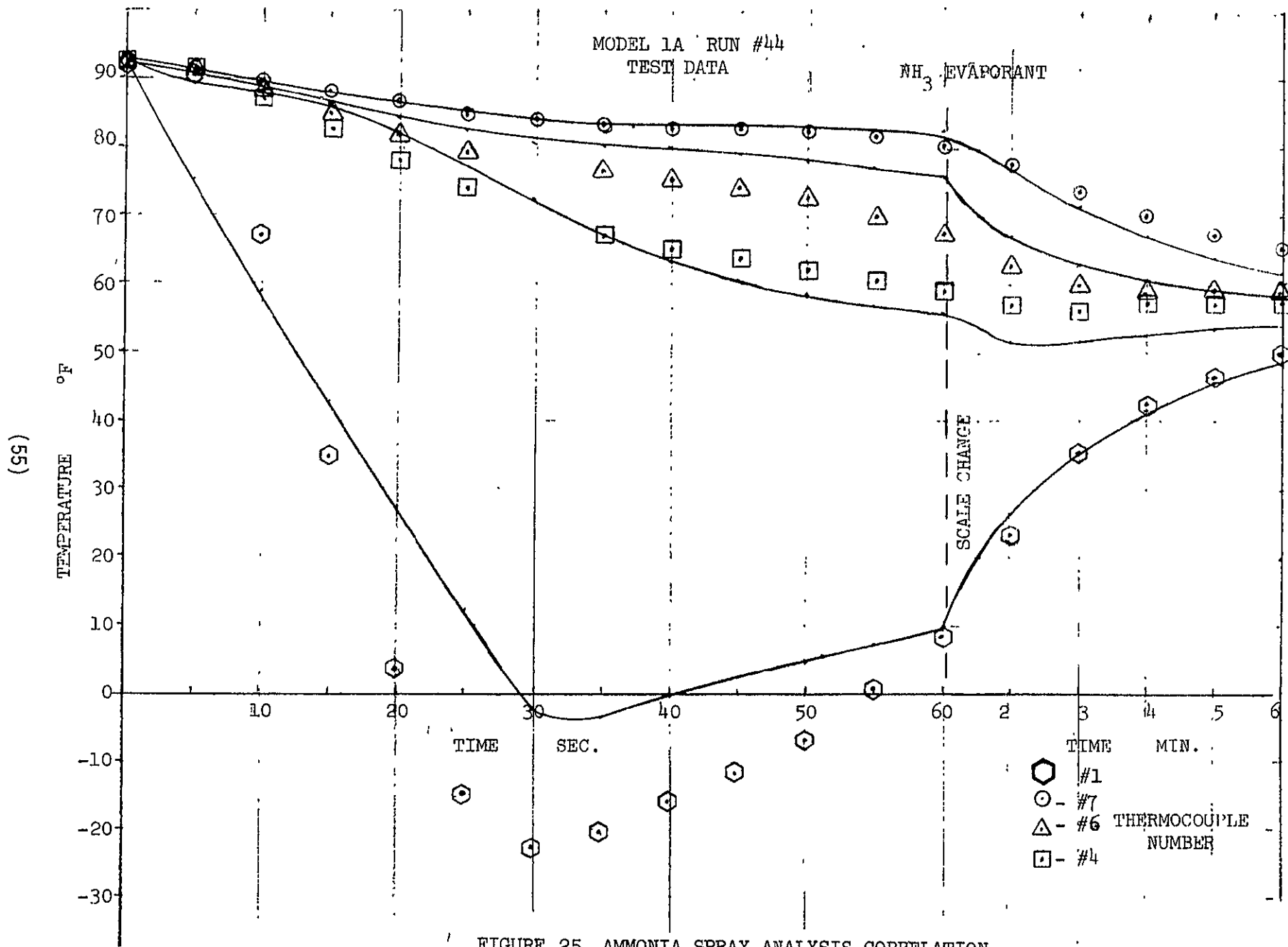


FIGURE 25 AMMONIA SPRAY ANALYSIS CORRELATION

Model 2 - Thermal model 2 was used to estimate several properties of the expected control system performance. Preliminarily, the proportional and organ pipe control models were run to demonstrate their capacity for performance. Figure 26 shows the response of a proportional control evaporator to the indicated profile. The deadband for this calculation was $+5^{\circ}\text{F}$ and the maximum overshoot was minimal. This type control is shown therefore to be capable of excellent modulation, since the overshoot is anticipated to be independent of the deadband selected. Figure 27 shows the response of a 6 unit organ pipe control unit. As the heat load ramps up to its maximum, the six distinct temperature drops accompanying the operation of the individual evaporators are evident. The control band for this calculation was between 35 and 45°F which supposedly could be changed while maintaining the small amount of overshoot noted in Figure 27.

Ideally, the on-off control scheme can function as well as any considered. This operation would occur with a uniform deposition of evaporant and proper sensor location. The sensor was located at or near the most downstream cooled evaporator position. Its position was varied to determine the sensitivity of the mentioned characteristics. Before discussing this influence, however, the effect of temperature deadband on cyclic rate is shown in Figure 28. As would be anticipated, the larger deadband leads to decreased cyclic rate, while the overshoot is nearly the same. It should be emphasized that the overshoot is that at the sensor location and not at the outlet of the device. Depending on the length of tubing between the sensor and the outlet, a considerable thermal damping can be achieved.

The effect of sensor position on outlet temperature variation is depicted in Figure 29. If the sensor is located upstream of the most downstream cooled location, the outlet temperature is biased to lower temperatures. If the sensor is located downstream of the cooled section, the delay in responsiveness of the sensor causes increased overshoot and increased cycle length.

The response of the evaporator to load transients has been evaluated by subjecting the evaporator to inlet temperature transients of about 12.5 degrees per minute (equivalent to a total load decrement in four minutes). This is greater than the anticipated transients by several fold. Figures 30 and 31 show the inlet temperature transients which were assumed, together with the control temperature variation which resulted during the profile illustrated for three values of temperature deadband. In each case, the predictions show the outlet control to be maintained in a quasi-steady state oscillation mode during the transients.

The final result concerns the amount of damping provided by the non-cooled fluid passage between the control sensor and the outlet. Figure 32 shows the magnitude of temperature excursion achieved by the outlet compared to the excursion at the control point with the outlet located at various downstream lengths. These results are obtained for a particular set of parameters and are not intended to be general in applicability.

(57)

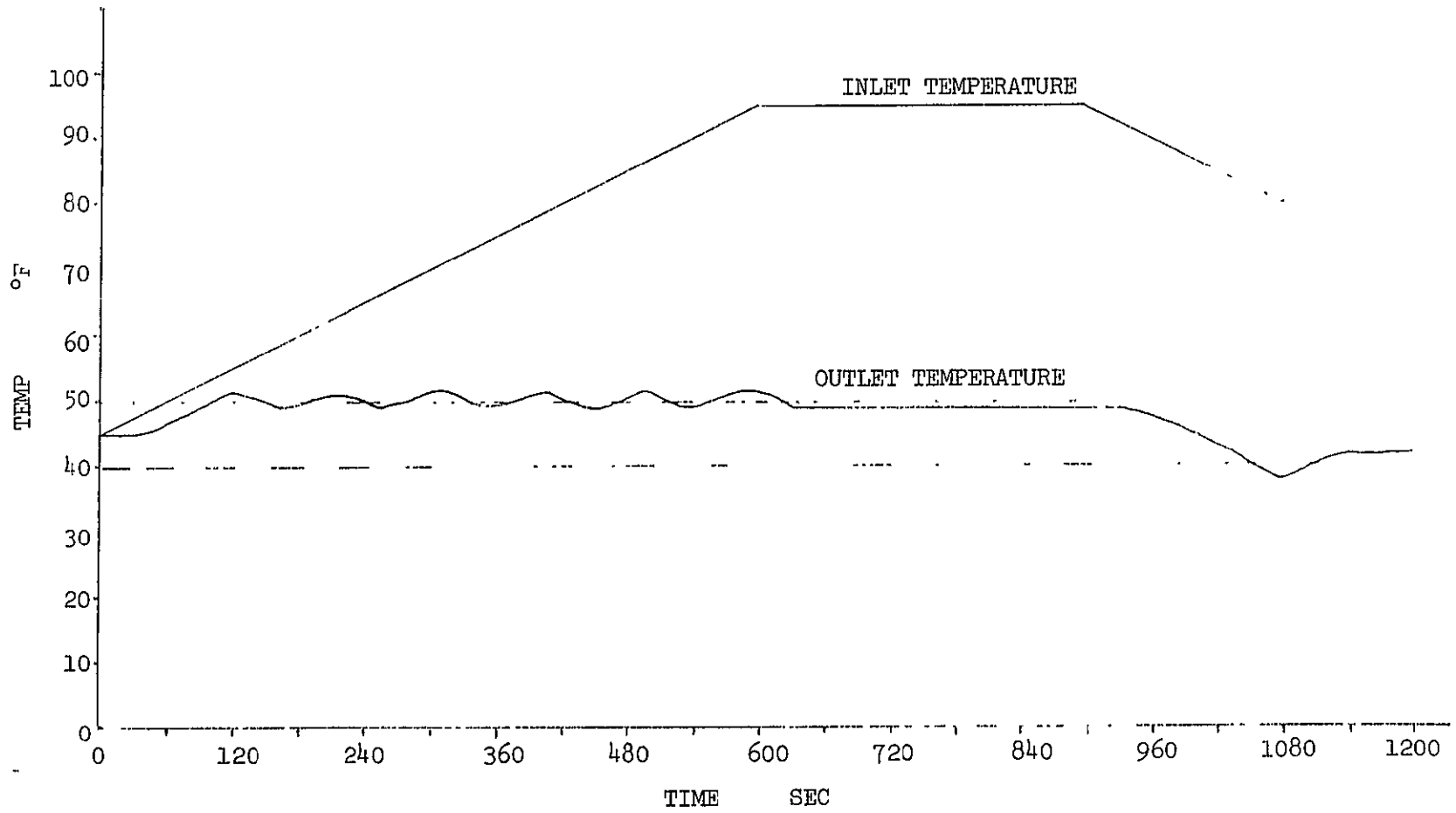


FIGURE 26 PROPORTIONAL CONTROL RESULTS

(85)

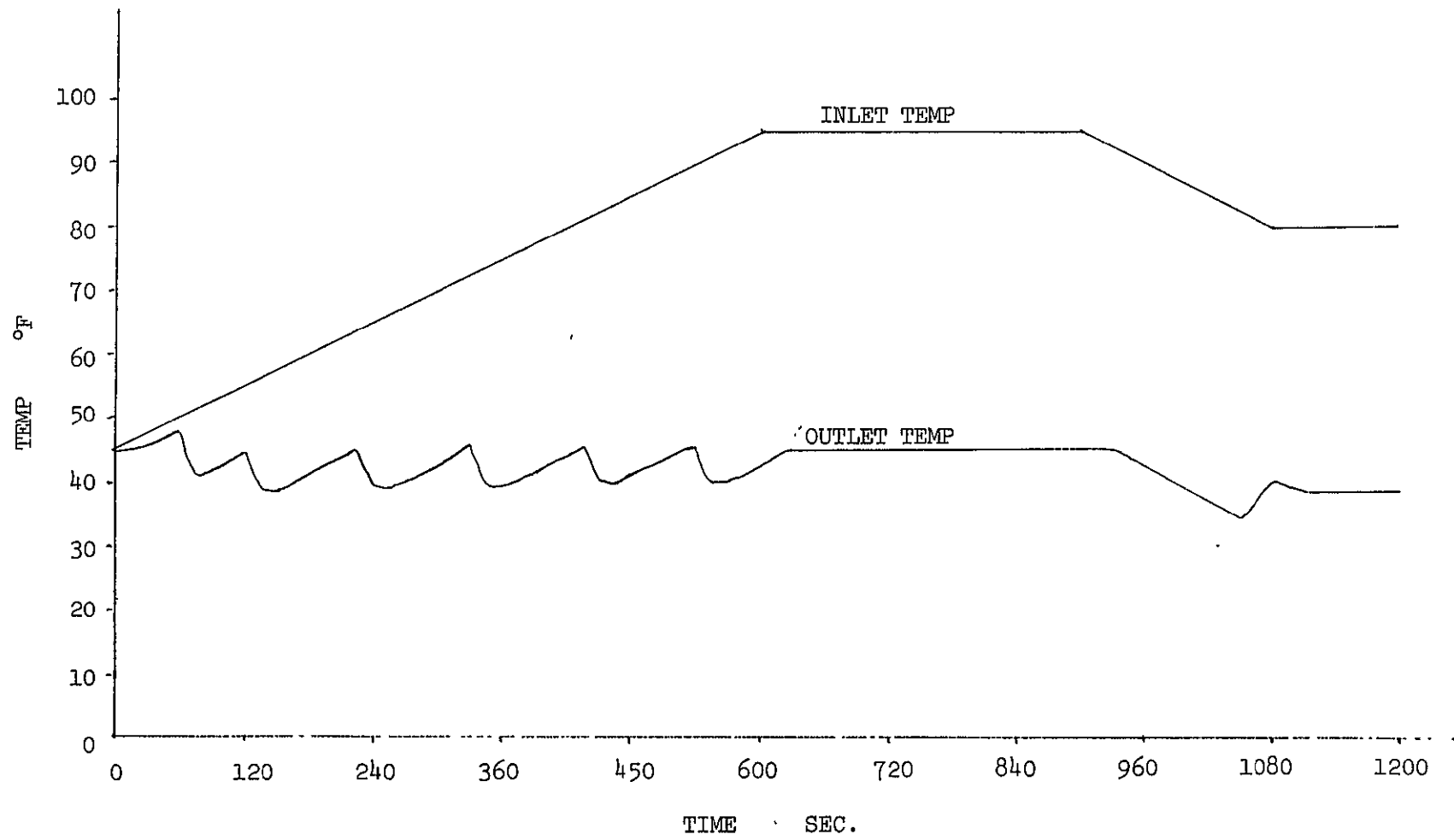


FIGURE 27 ORGAN PIPE CONTROL RESULTS

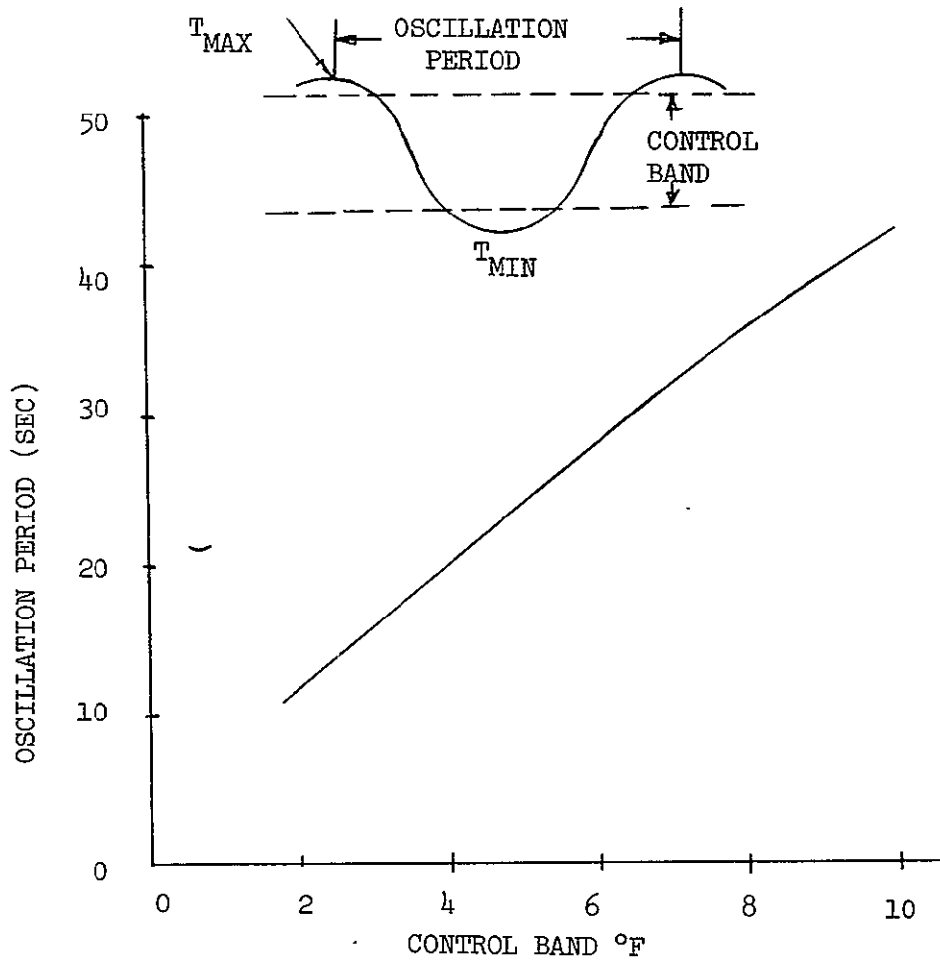
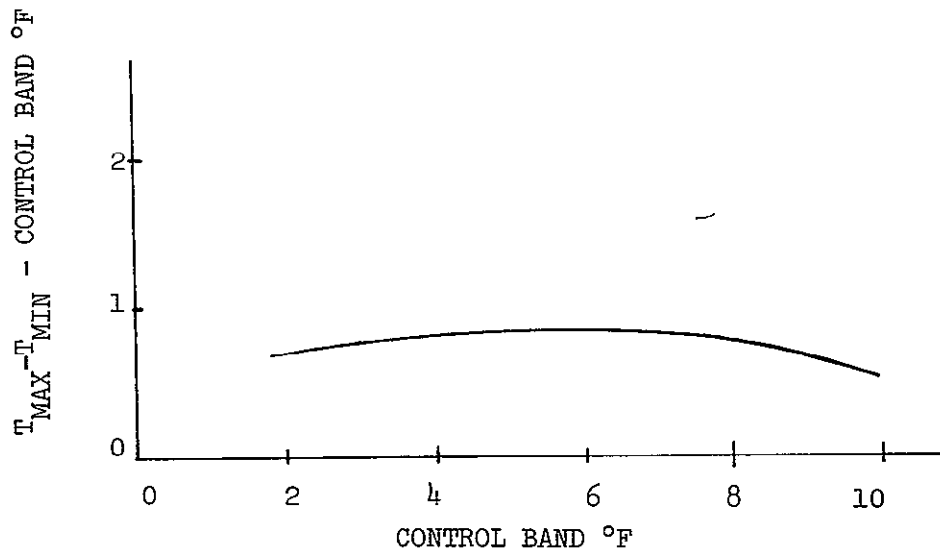
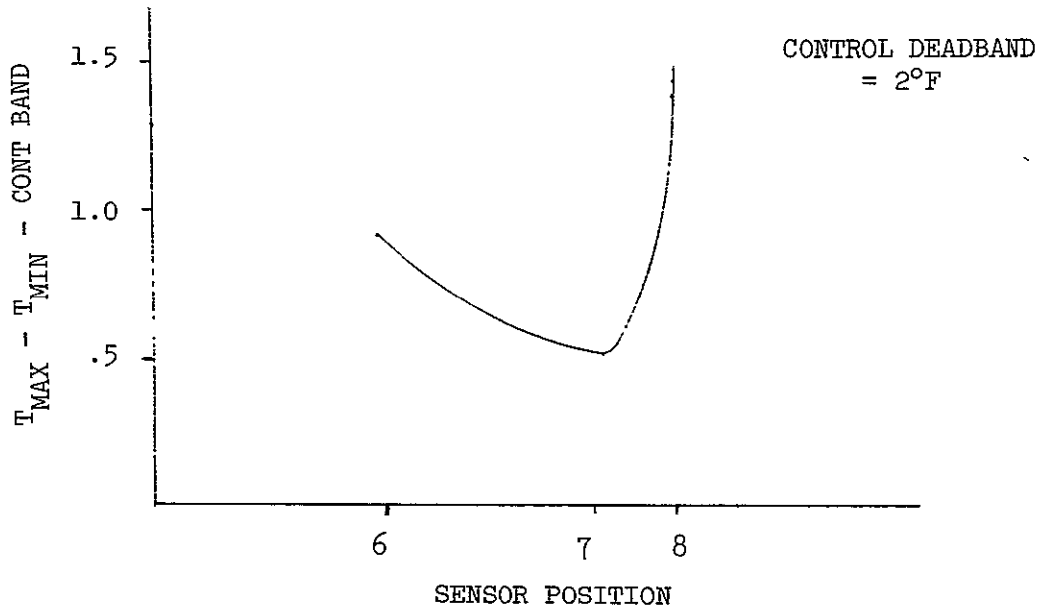


FIGURE 28 EFFECT OF CONTROL BAND ON OVERSHOOT AND OSCILLATION PERIOD



REFERENCE: COOLED LENGTH = 132 FT,
THROUGHPUT TIME = 19.5 SEC

POSITION INDEX	REMOVED FROM END OF COOLED SECTION	
	LENGTH	TIME
6 UPSTREAM	33 ft	4.6 sec
7	0	0
8 DOWNSTREAM	10.6 ft	1.5 sec

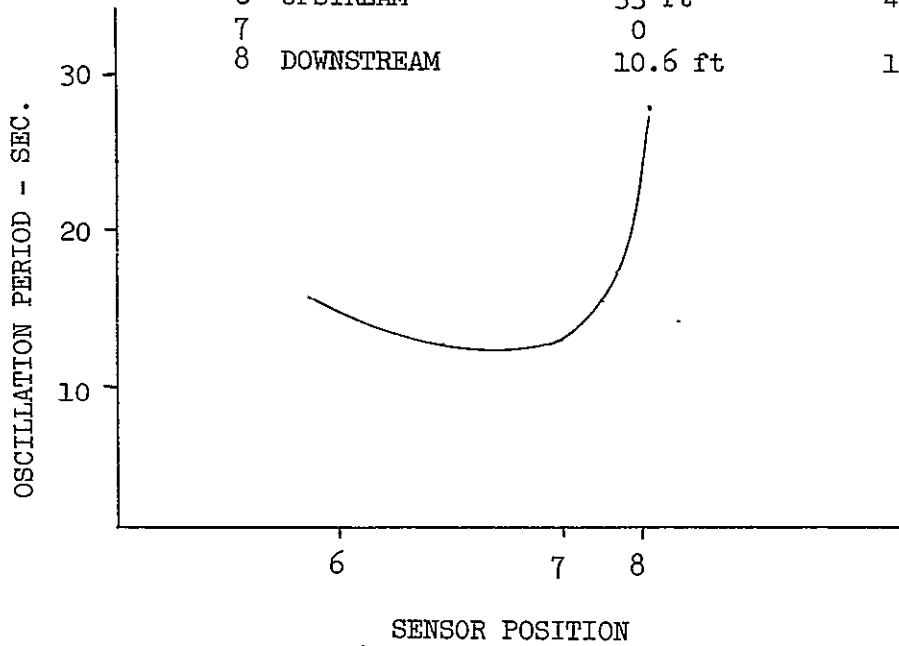


FIGURE 29 EFFECT OF DOWNSTREAM POSITION ON OVERSHOOT
AND OSCILLATION PERIOD

(T9)

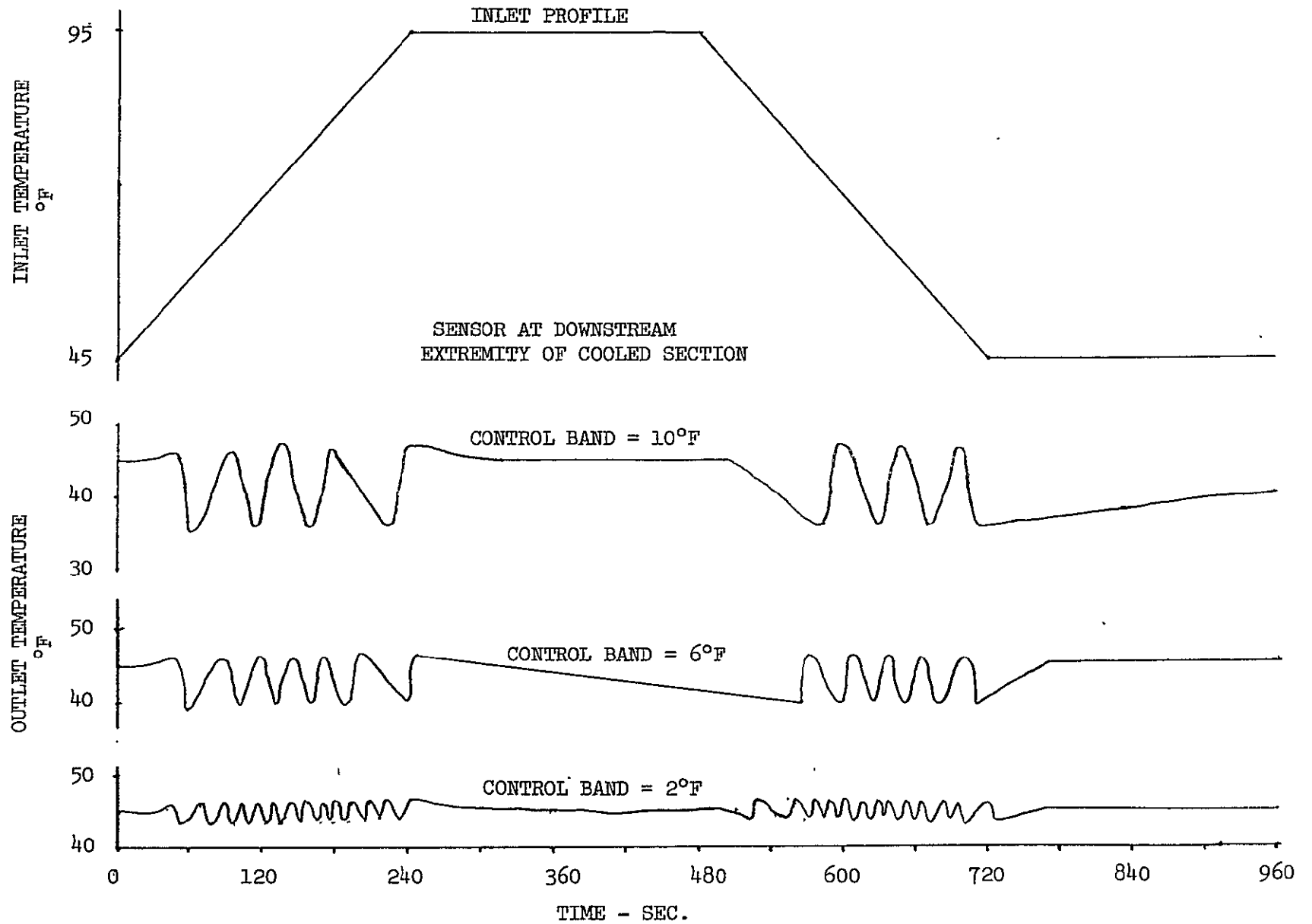


FIGURE 30 COMPUTED RESPONSE TO HIGH LOAD PROFILE

(62)

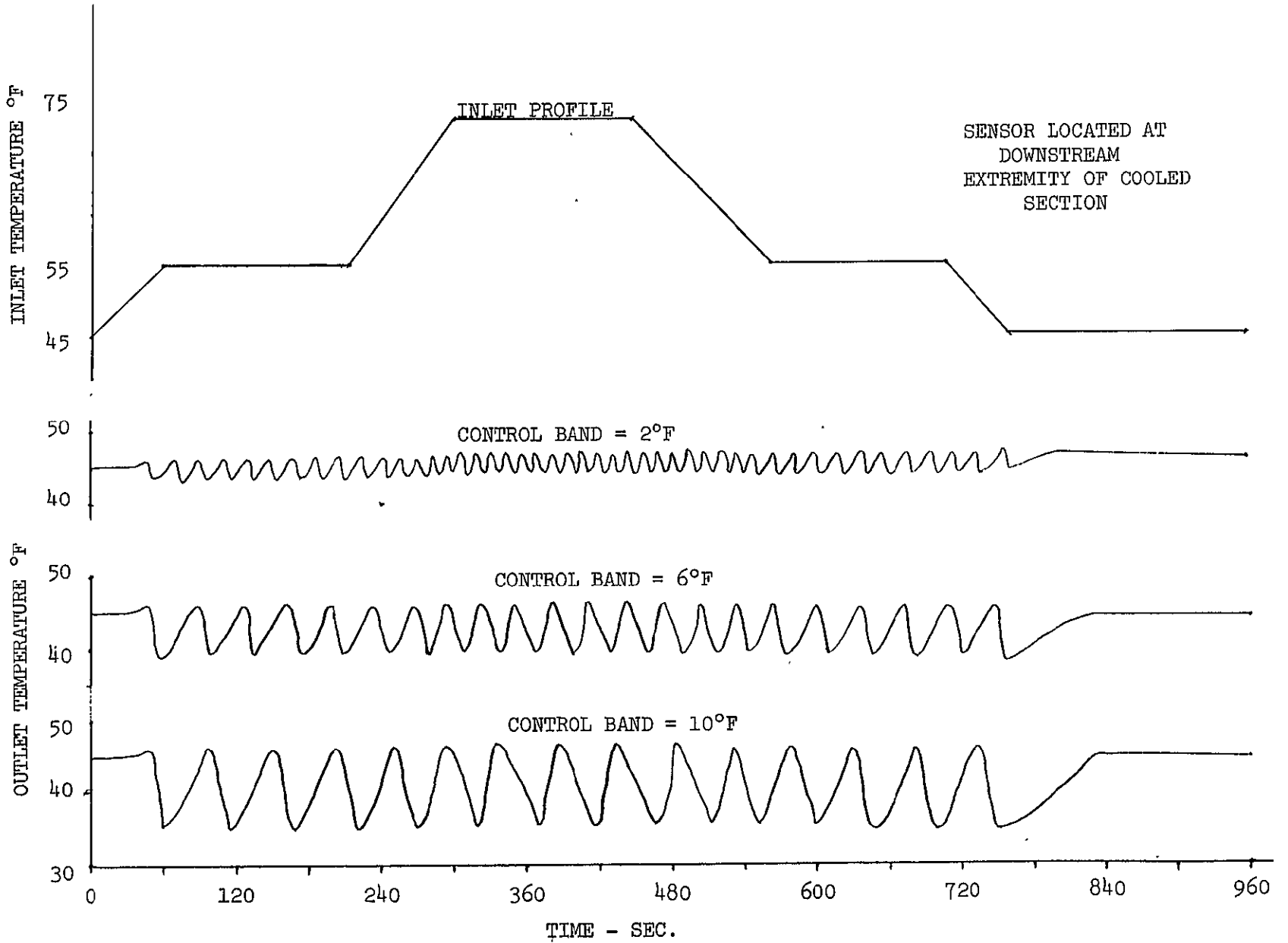


FIGURE 31 COMPUTED RESPONSE TO LOW LOAD PROFILE

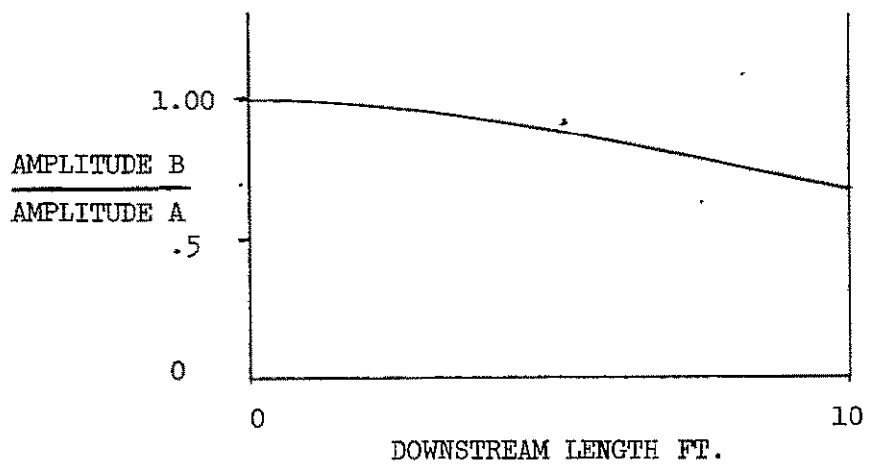
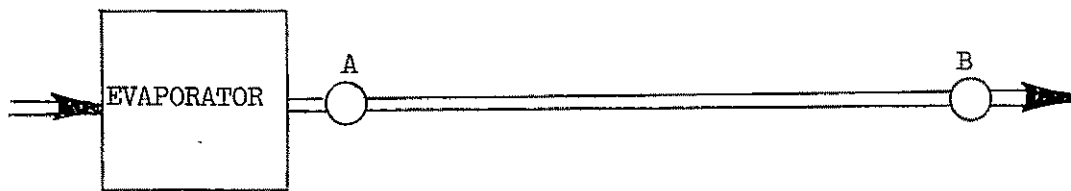
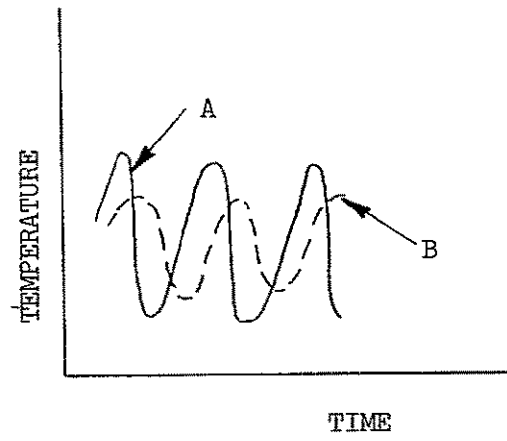


FIGURE 32 EFFECT OF TUBING EXTENSION ON AMPLITUDE OF TEMPERATURE VARIATIONS

3.7 Exploratory Tests

In support of the analytical design work it was judged profitable to perform some rudimentary testing. This testing was required to demonstrate (1) nozzle function in vacuum conditions, (2) freezing characteristics of water particles, (3) feasibility of "dry wall" evaporation, and (4) operability at high "g" levels. The basic data of the test is compiled in Reference 12, from which the significant data is extracted herein. In addition the test log contains certain other informal entries not contained elsewhere.

The basic test concept was that a solid, fairly heavy test article could simulate an evaporator. The test article stored energy is analogous to the convective energy flow of the evaporator transport fluid. Small heaters were used to raise the temperature of the test article, and the material was allowed to achieve a uniform heat distribution. At that time in the sequence the evaporant was sprayed on the evaporator for a prescribed time, then shut off. After several minutes, the temperatures of the evaporator model became uniform again. The energy difference of the evaporator before and after the evaporant flow (excluding external gains and losses) must be identical with the evaporative effect of the spray. The following simple energy balance equation has been used to assess all evaporation efficiencies.

$$W_f \cdot \Delta h = W_e C_{p_e} (T_{\text{initial}} - T_{\text{final}})$$

Here W_f is the expended evaporant weight, Δh is the enthalpy rise actually imparted to the evaporant, W_e is the weight of the evaporator, C_{p_e} is the specific heat of the evaporator, and the temperatures are those of the evaporator before and after spraying.

Before the evaporators were run, several of the spray nozzles were run to determine the spray patterns and flow coefficients. Reference 6 has shown a considerable variation in flow coefficient when boiling within the nozzle is possible. In general, the liquid flow becomes full of vapor nuclei of lower density causing the average flow density and hence flow coefficient to decrease. Because of such a decrease, measured relations shown in Figure 33 of flow rate versus pressure drop were obtained to later set up the pressures to achieve a desired flow rate.

During one test series a container of water was saturated with hydrogen by first bubbling the hydrogen for about 10 minutes through the water and then allowing the hydrogen at 60 psig to remain covering the water for over 48 hours. No difference in spray pattern or flow coefficient was noted due to the dissolved hydrogen as shown in Figure 33.

Figure 34a, b shows a water spray at atmospheric pressure through a full cone spray of large size and a hollow cone spray of small size. Figure 34c shows the same hollow cone spray in the vacuum condition. These pictures are representative of all of the configurations achieved. The Freon spray

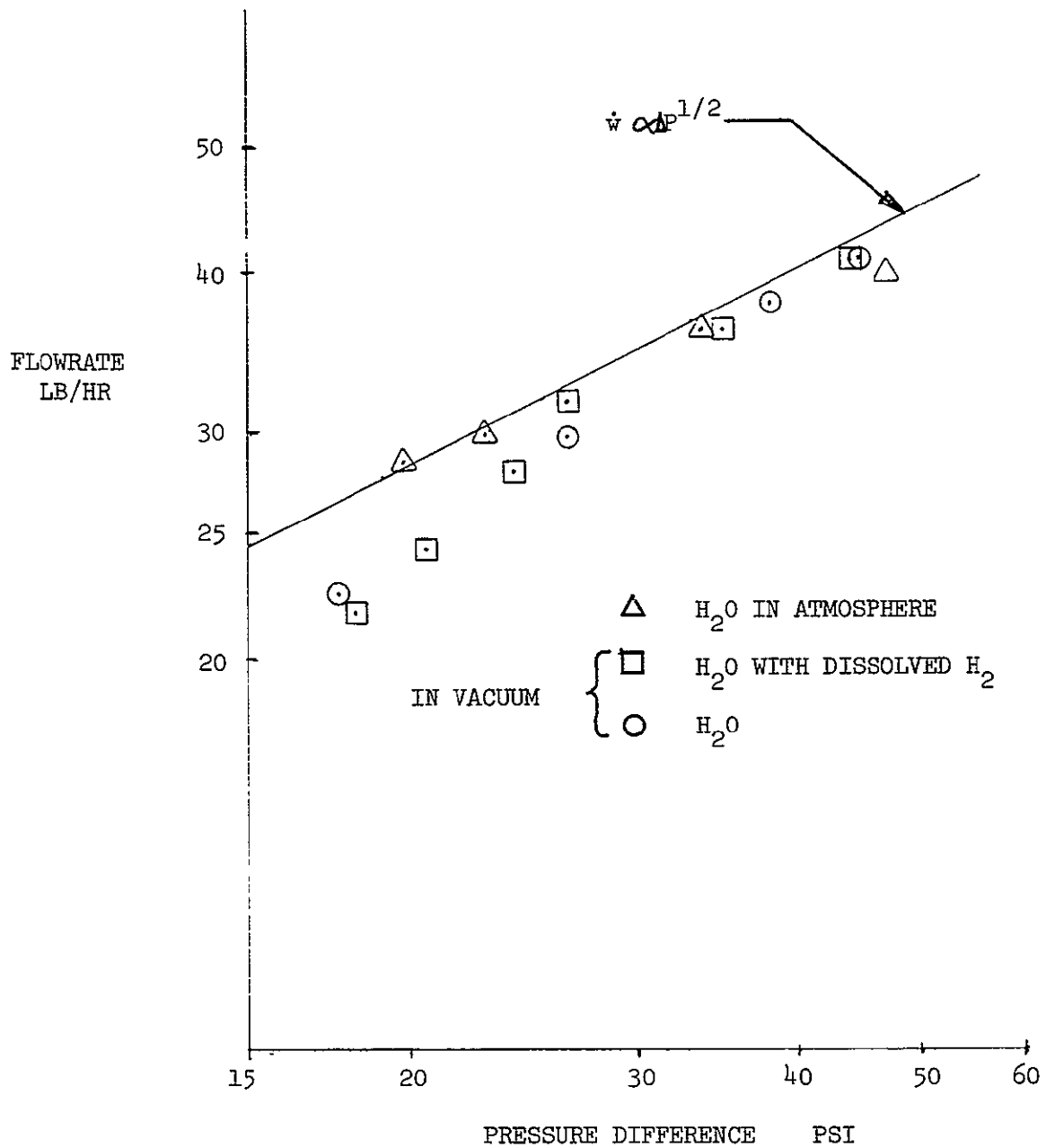
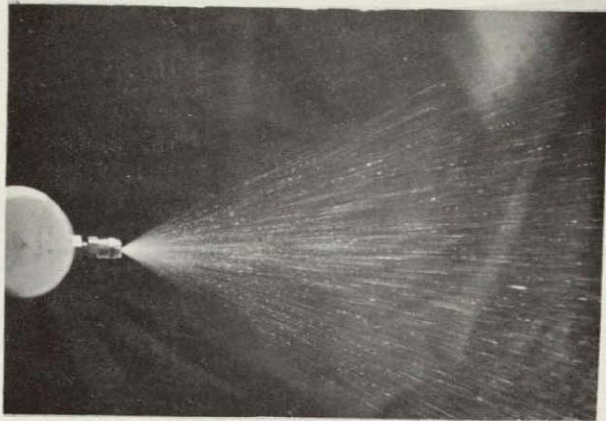
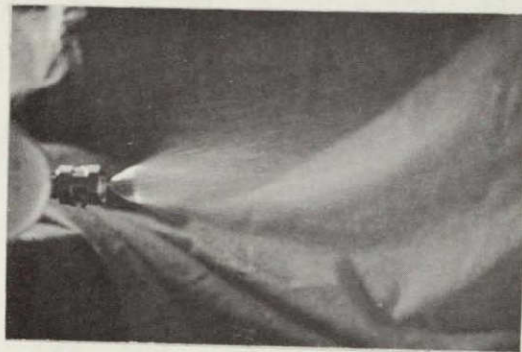


FIGURE 33 ORIFICE FLOW DATA MEASURED FOR ATMOSPHERIC AND VACUUM CONDITIONS

FIGURE 34 TYPICAL SPRAY PATTERNS



(A)
Large full cone spray
at atmospheric pres-
sure with water



(B)
Smaller hollow cone
spray at atmospheric
pressure with water



(C)
Smaller hollow cone spray
in vacuum with water.
Supply pressure identical
with above.

had an appearance nearly identical to that of Figure 34a and the ammonia spray to that of Figure 34b. At reduced pressures a tendency to increase the envelope of each of these was noted. The exact angle of the water spray coverage in the vacuum condition was judged from the location of frost on the container. The frost line covered from 5 inches to 15 inches downstream of the nozzle at a radius 9 inches from the jet axis. From this it was judged that the envelope of the spray is between 60 degrees and 30 degrees measured from the spray axis. The deposition was difficult to judge but appeared to be fairly uniform without any apparent holes or excesses. However, this judgment could be in error easily by a factor of two.

Deliberate attempts to obtain a frozen nozzle were made. The nozzle was cycled on and off at various intervals. Even though the liquid hold up was noted to freeze promptly at the orifice the ice formations would either fall off or be ejected upon a new start up. No freezing problems could be encountered.

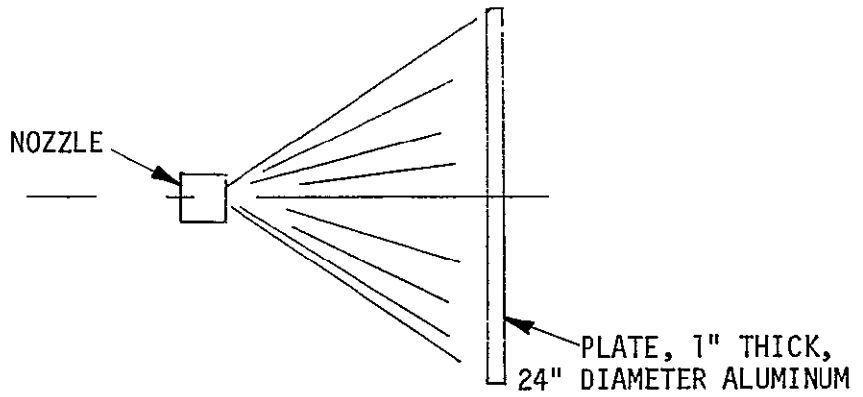
During the evaporator testing, the three basic configurations shown in Table 3 were subjected to 45 runs, of which 5 runs were null; two due to plugged nozzles (from debris), two from failure to turn on the reference junction (which was shut off during pumpdown to avoid corona discharge on the slip rings in 4 g tests) and one from a solenoid valve failure to shut off. In addition, two runs had questionable evaporant measurements, and one run suffered extreme accuracy loss from not allowing sufficient time to equalize temperatures before and after spraying.

The basic accuracy of the test measurements were dependent upon the conditions of the run and upon basic instrumentation inaccuracy. The thermal capacity of the evaporator was known to within about 2 percent; the value of uniform temperatures were known generally to within a basic accuracy of about one degree. Expended evaporant was known to within five percent for water, 3 percent for NH_3 , and one percent for R-22. The liquid holdup within the solenoid and nozzle was measured as 10 cc or about 10 percent of the expended volume of water on an average run. This latter factor causes considerable difficulty in interpreting the results because the holdup volume generally extruded from the nozzle as ice pellets about 5 mm in characteristic dimension. These pellets were repeatedly observed to persist past the time when the final temperature measurement was generally taken so that they could not have added significantly to the energy removed from the evaporator.

Pressures (evaporant supply, chamber) were believed to be accurate to well within their range of significant effect. An uncertainty in the non-vacuum runs arose due to the heat transfer with the environment, particularly during the spin rig tests. In each of these cases, the initial temperature and evaporant expended amount were selected to achieve the condition where the final temperature was as close as possible to ambient temperature. Also, the spin rig was stopped quickly after the 4 g tests while the temperatures equalized in the simulated evaporator. Radiation interchange during the water runs calculates to be well within 5 percent for the extreme case. Care was taken to avoid excessive heating by the lamps used for observation.

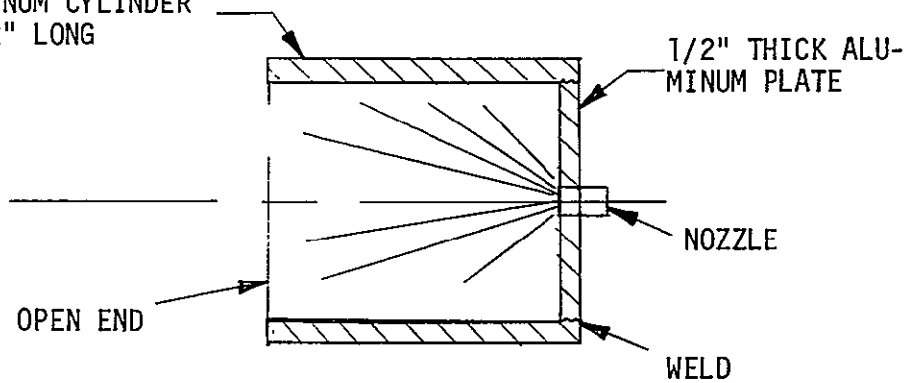
TABLE 3 PRIMARY CONFIGURATIONS

CONFIGURATION 1

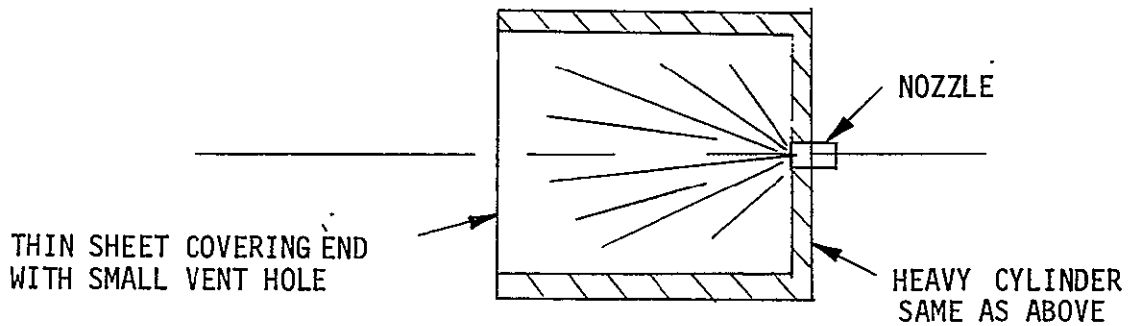


CONFIGURATION 2

12" O.D. ALUMINUM CYLINDER
1/2" THICK, 12" LONG



CONFIGURATION 3



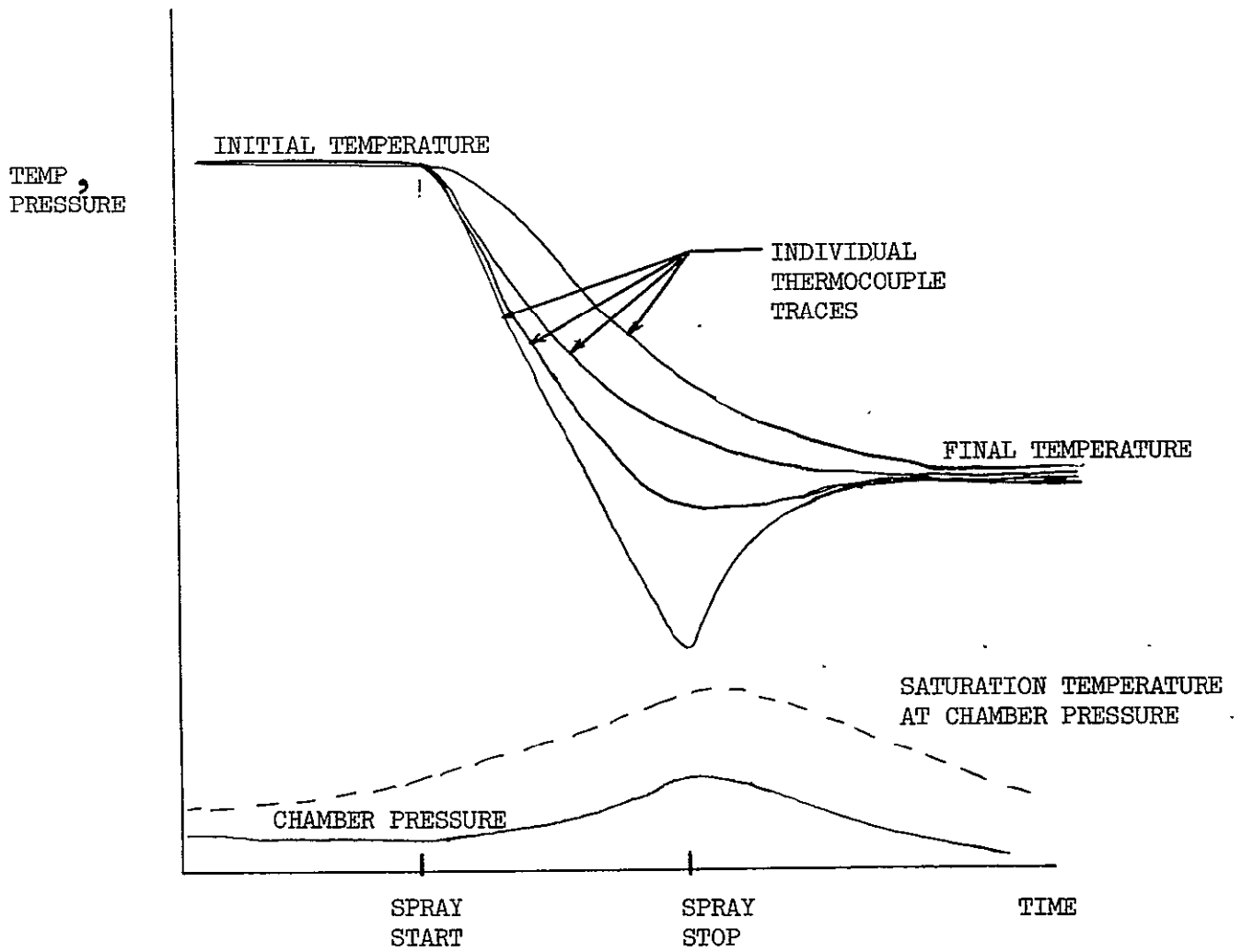


FIGURE 35 ILLUSTRATION OF DATA FEATURES

The first three runs were conducted with water and the configuration 1 (plate) evaporator. The chamber pressure was maintained to below 0.01 psia for each run. Visual observation indicated (1) that many spray particles bounced off the evaporator at first impingement and (2) that in one area the spray density must have been higher such that a patch of frost about 3 x 5 in. developed to a thickness of about 1/4 inch. The evaporator was faced upward with only a slight slope and the frost layer persisted for over 1/2 hour when it was removed by tipping the evaporator plate and allowing it to slide off.

The evaporant weight as recorded by the load cell on the first two runs disagreed with the nozzle calibration. The third and later runs agreed, and it was concluded that the expended weight from the nozzle calibration was the favored datum. The evaporation enthalpy of the water on these two runs was 590, 633, and 437 Btu/lb, respectively. The last run was a lesser amount due to the effect of the lower surface temperatures achieved during the test. On runs 1 and 2 the temperature was above 30°F while on run 3, the temperature was as low as 15°F. Below 30°F the evaporation is surely suppressed since the droplets would freeze on the wall even if they were liquid upon impingement, and the rates of heat transfer diminish rapidly at lower temperature.

Runs 4-18 were conducted with water at various chamber pressures for configuration 2. The nozzle employed was the hollow cone type which wet about one half of the cylindrical wall section. A typical result is shown in Figure 35 to illustrate the type of data obtained during the run. Table 4 lists several of the important data obtained in this test group. The evaporation amount is obtained from use of the entire liquid flow and the initial-to-final evaporator temperature changes in the heat balance equation. The enthalpy value obtained by deleting the 10 cc of liquid from the total expended fluid weight is also shown.

The value of lowest minimum temperature (Column 4 in Table 4) seems to be capable of causing a lower evaporation energy to occur when it drops much below freezing. Also for each run having sub-zero saturation temperatures the evaporation energy was lower. On these runs there was visual evidence of particles freezing and bouncing out of the evaporator. The effect of these parameters was correlated according to basic causes as follows.

Figure 36 shows a plot of evaporation enthalpy versus the difference in minimum wall temperature and maximum saturation temperature. Two envelopes of data are identified which discriminate the data according to the maximum saturation temperature, which is shown in parenthesis by each point. The low saturation temperature runs suffer presumably because of particles freezing in transit. The other evaporation enthalpies suffer because of possible accumulation. This accumulation arises when the potential difference of the wall and liquid surface temperatures reduces the evaporation rate considerably. The runs at about 950-1000 Btu/lb enthalpy effectively demonstrate high liquid utilization. Maximum droplet evaporation enthalpy proved difficult to judge experimentally but can be inferred from the predicted, evaporating surface temperature. The surface was analyzed in Section 3.3.3.2 to be at about 20°F, at which the vapor enthalpy is 1070 Btu/lb compared to saturated liquid enthalpy of 38 Btu/lb at the

TABLE 4 SUMMARY OF TEST RESULTS WITH WATER

RUN	INITIAL TEMP. °F	FINAL TEMP. °F	LOWEST EVAP- ORATOR TEMP °F	HIGHEST SATURATION TEMPERATURE (@ CHAMBER PRESSURE - °F	EXPENDED FLUID WEIGHT LB.	EVAPORATION ENERGY (RAW) BTU/LB	EVAPORATION ENERG CORRECTED BY (10c LIQUID LOSS)
4	116	66	26.6	10	.40	716	751
5	97	59	14.2	-10	.40	545	572
6	99	55	44.6	27	.40	630	661
7	55	20	18.	15	.40	500	525
8	101	48	37.	30	.40	760	797
9	89	50	8.	Below -20	.40	557	585
10	109	60	38.	15	.31	910	975
11	116	97	66.	-10	.19	572	640
12	97	78	62.	Below -20	.19	572	640
13	106	74	36.	Below -20	.27	680	735
14	98	60	31.	10	.25	870	948
15	108	78	37.	2	.20	860	955
16	113	75	44.	20	.25	870	947
17	75	49	26.	15	.21	710	790
18	128	93	50.	15	.22	910	1000

(72)

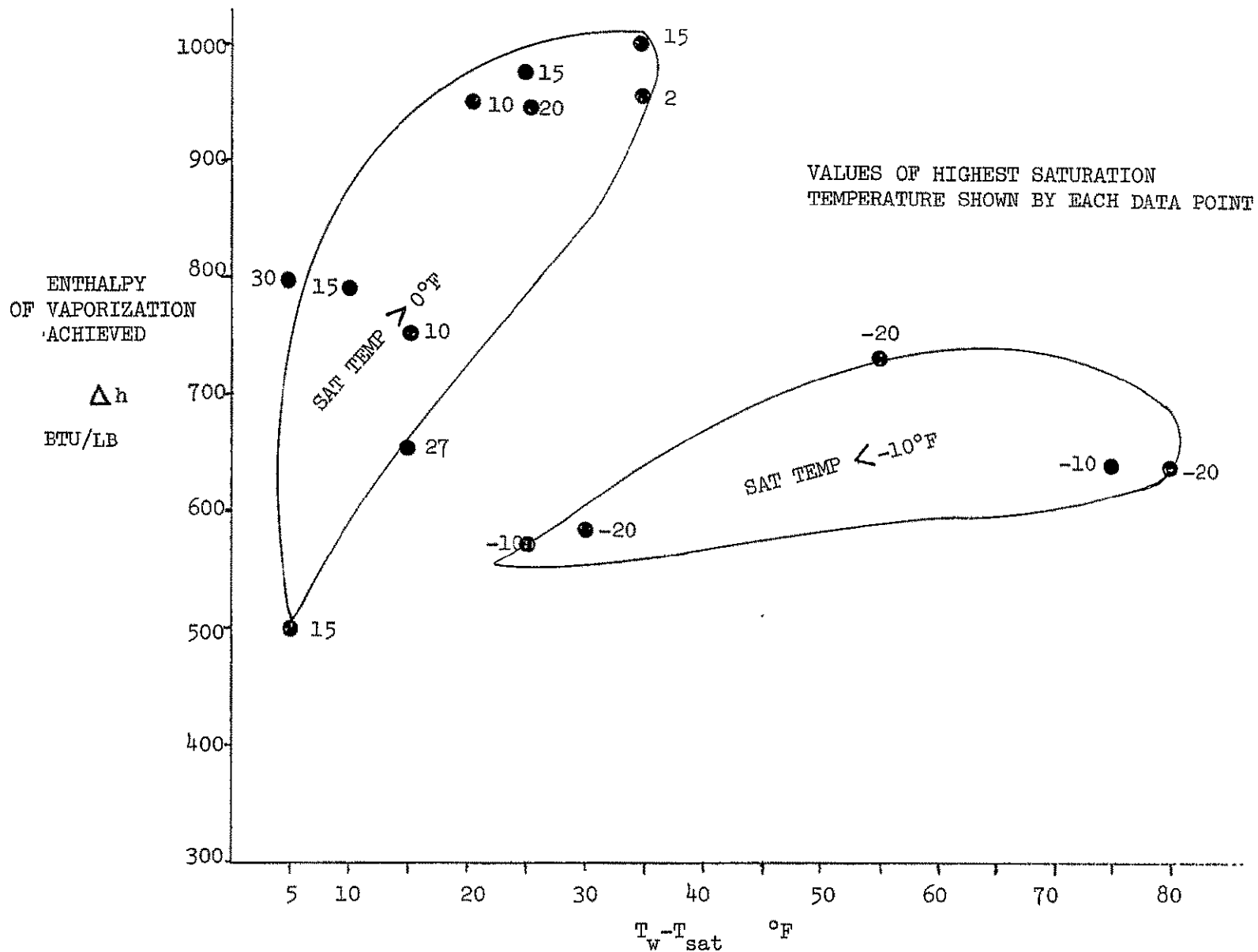


FIGURE 36 RESULTS OF PRELIMINARY WATER TEST

inlet. The maximum theoretical enthalpy of evaporation then is 1032. The instrumentation accuracy inherent in this first test was incapable of better than +50 Btu/hr probably so liquid utilization may only be judged close to 100 percent. To demonstrate that the gross efficiency dependence on ambient pressure was correctly assessed, a slight modification of configuration was adopted. An end plate was affixed having a 2.25 inch hole in it. This hole would cause the internal pressure to rise to about 0.05 psia (20°F saturation temperature) where the high efficiency operation was noted. With this change, the evaporator was run with the chamber at a pressure below 0.01 psia and high efficiency was achieved.

In the Freon runs which followed, it was noted visually that the open cylinder configuration produced a large mist flow out the open end. Since the particles in the cloud clearly could not participate in evaporator cooling, the evaporation efficiency suffered accordingly. In the remaining runs, the open end of the evaporator was covered with a small hole remaining to exhaust the flow. These later runs resulted in increased evaporation efficiencies. Figure 37 shows the evaporation enthalpy amounts achieved versus the evaporation pressure. Also shown is the maximum enthalpy expected which is the enthalpy of liquid sprayed subtracted from the saturated vapor temperature at the appropriate exit pressure. In the higher efficiency, closed evaporator runs, some liquid still must escape to account for the reduced enthalpy difference. Indeed, the liquid Freon was observed to pool in the bottom of the evaporator and drip out. In addition, some mist still escaped from the exit port.

The implication of the pooling of Freon is fairly clear. First, the liquid accumulated on the wall. Second, its presence poses the potential for strong local cooling. The first test did not establish whether any local cooling problems existed nor whether a control problem could result.

For the 4-g runs the evaporator (Configuration 3) was mounted on a spinning frame which rotated nominally at 77 RPM. The nozzle exit was positioned at a radius of 19 inches. This radius was calculated by error to yield 4 g whereas the true acceleration was only 3.3 g at that point. A substantial acceleration gradient was present, and the spray had a coriolis acceleration which was much higher than the normal acceleration. Thus, the acceleration of some points in the evaporator were up to 9 g, and of others were lower, down to 1.2 g. The coriolis accelerations in the spray ranged up to about 40 g. The effect of the acceleration is twofold. The evaporant distribution is changed due to normal and coriolis accelerations but chiefly by the latter. Also the liquid behavior on the wall is subject to the normal acceleration. The spin tests were intended to test for only the normal accelerations, so any suspected effect of the coriolis acceleration should be analyzed in an attempt to separate its effect.

The water spray tests at 4 g were found to exhibit less evaporation efficiency and it was suspected that the cause lay in the possibility that the spray had been deflected so as to miss the evaporator. (Even though the end of the can was covered, hitting the end cover constitutes a "miss" since the spray freezes there and never cools the evaporator). To determine how much flow could be involved a simple analysis was performed of the spray trajectory. The sketch below depicts the situation analyzed.

(7L)

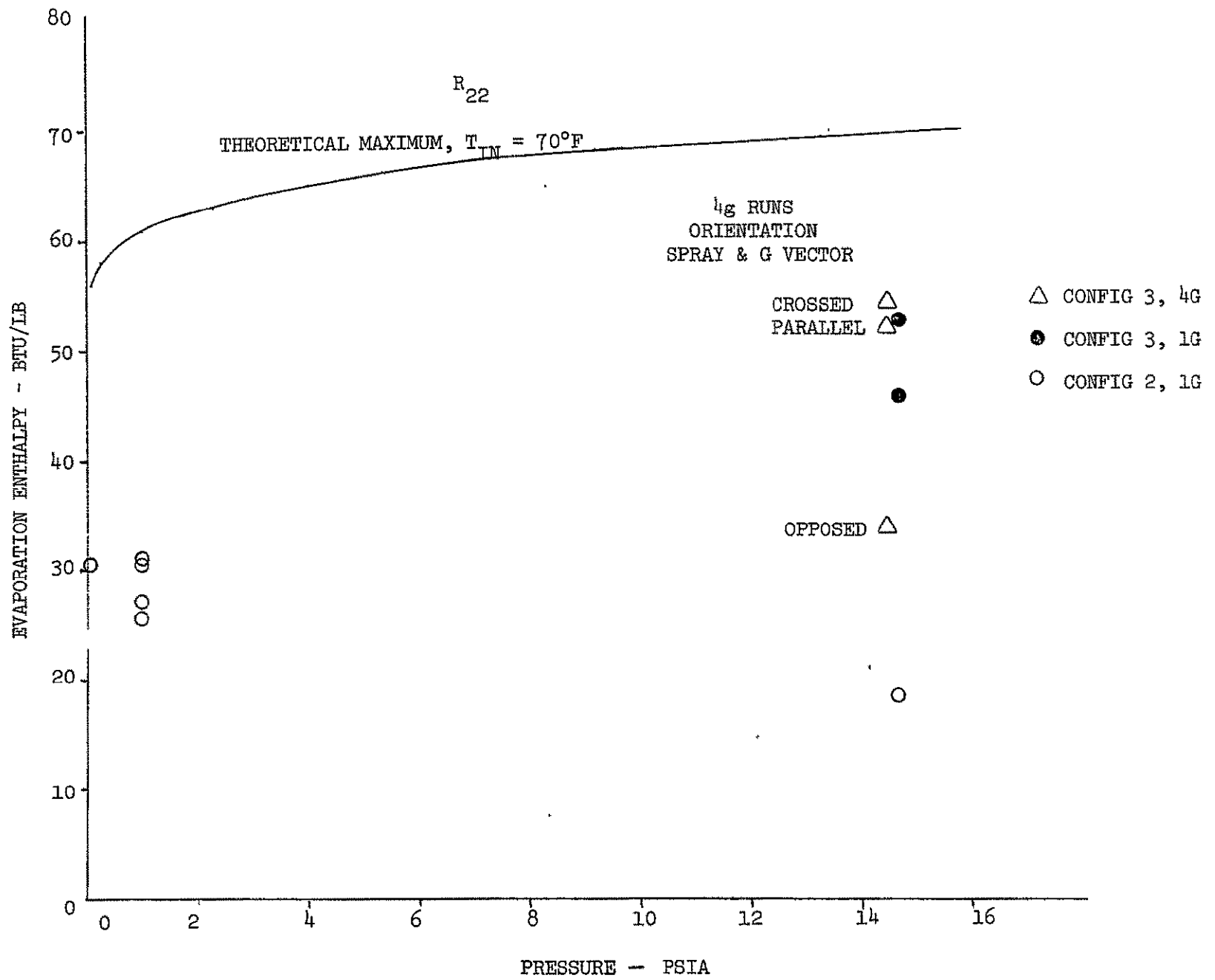
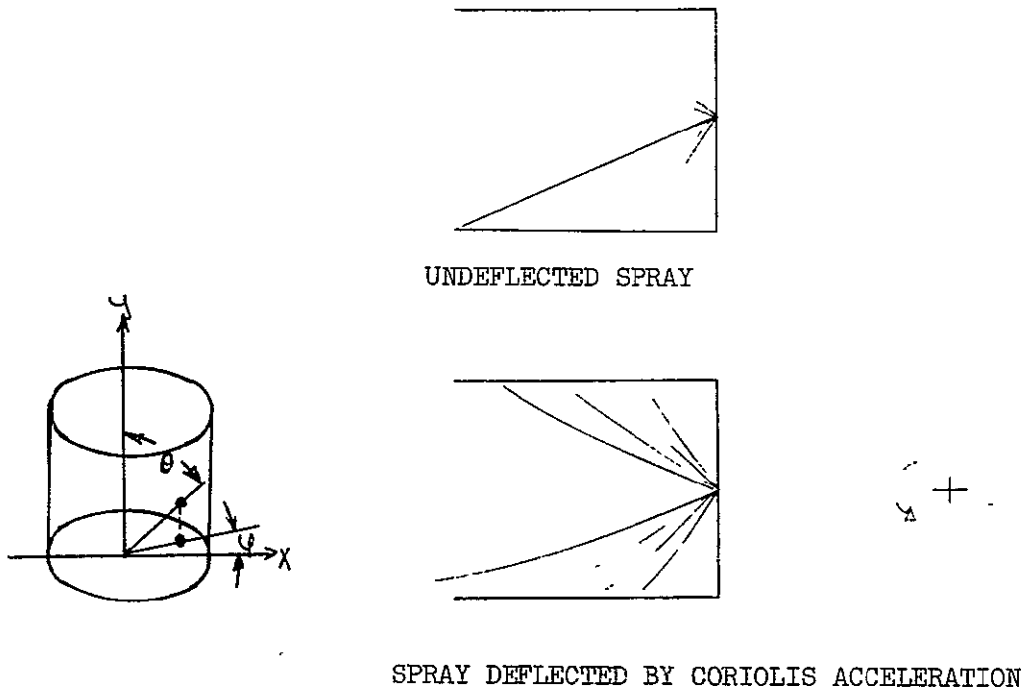


FIGURE 37 REFRIGERANT 22 EVAPORATION ENTHALPIES



The analysis determined the initial direction of the particles which hit the edge of the evaporator. If θ denotes the angle off centerline of the spray and φ denotes the azimuth, the function θ_e yields the initial direction off centerline of the particle which strikes the edge and which has initial azimuth φ_i . These functions are shown in Figures 38, 39, and 40, for the three orientations tested.

For the sake of calculation, it was assumed that the spray density was uniform within the bounds $\theta_1 < \theta < \theta_2$, where θ_1 = angle of the edge (24.6°) and θ_2 = 45 degrees. The fluid fraction spilled is then calculated from

$$\frac{\dot{w} \text{ spilled}}{\dot{w} \text{ total}} = \frac{\int_{\varphi=0}^{\varphi=360} (\theta_e(\varphi_i) - \theta_1) d\varphi_i}{\int_{\varphi=0}^{\varphi=360} (\theta_2 - \theta_1) d\varphi} \quad \theta_e \geq \theta_1$$

These calculations led to the values of spilled fraction tabulated below, together with the observed decrease in evaporation enthalpy.

(76)

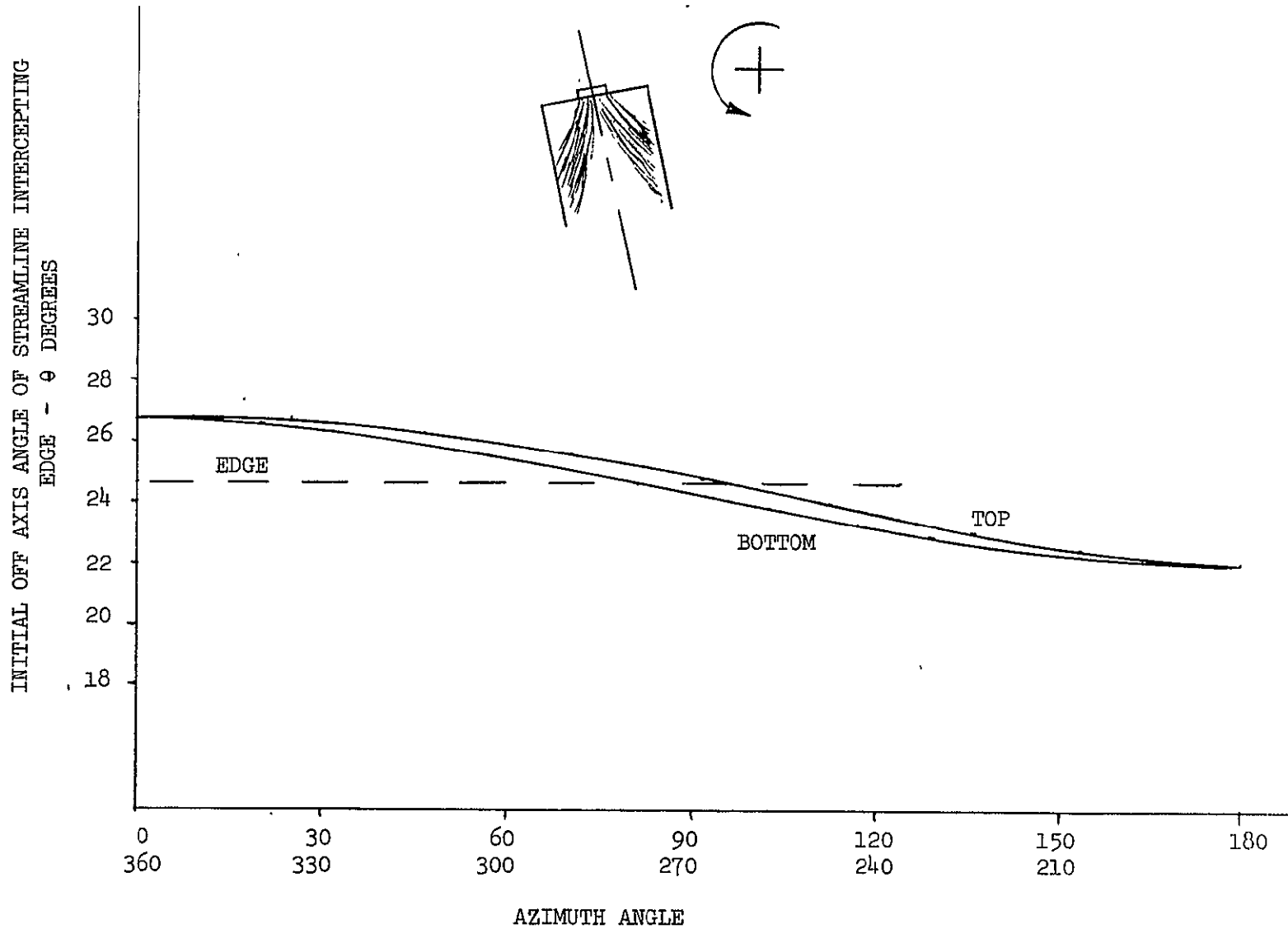


FIGURE 38 EFFECT OF SPIN TEST ON SPRAY DISTRIBUTION

(11)

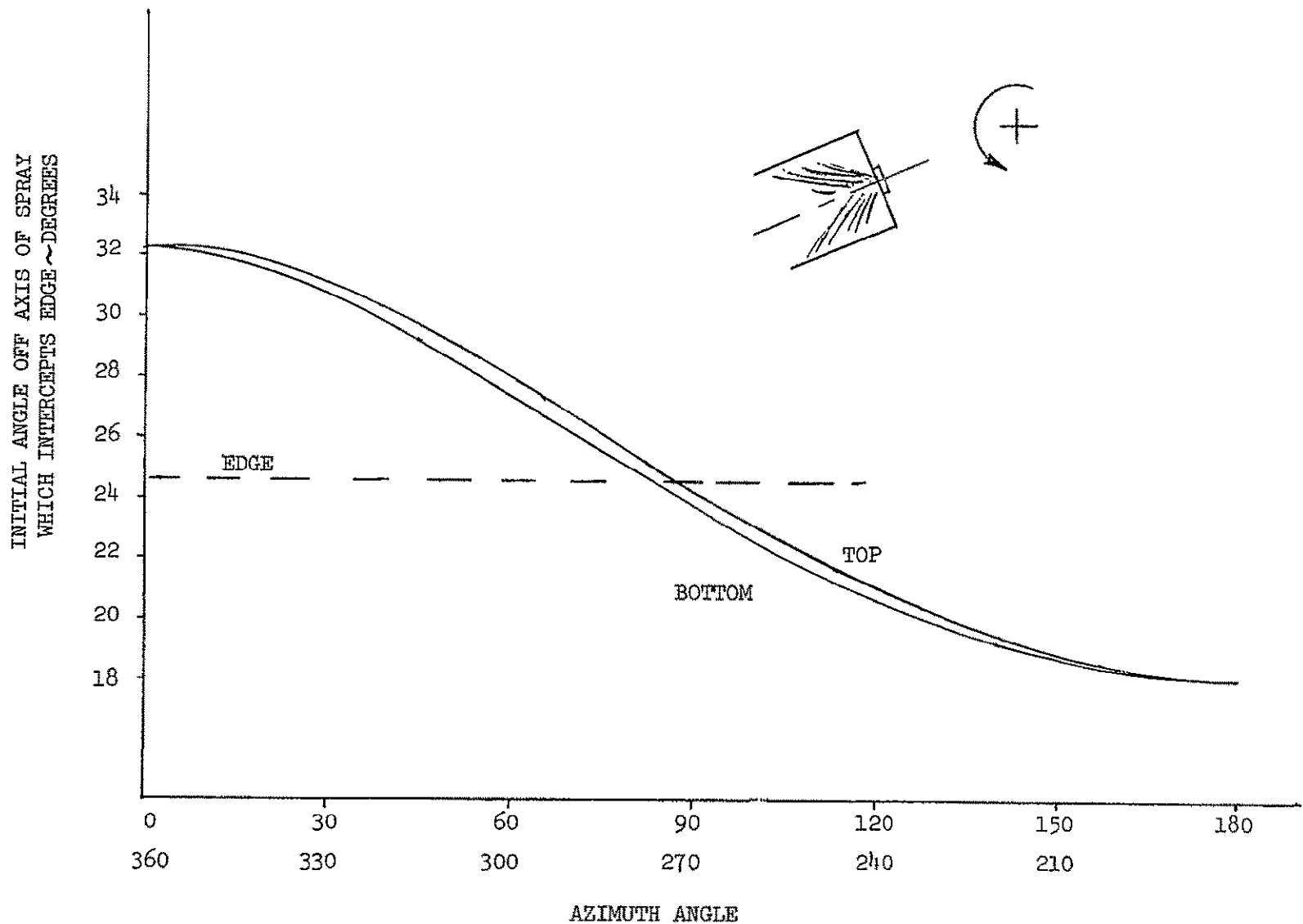


FIGURE 39 EFFECT OF SPIN TEST ON SPRAY DISTRIBUTION

(81)

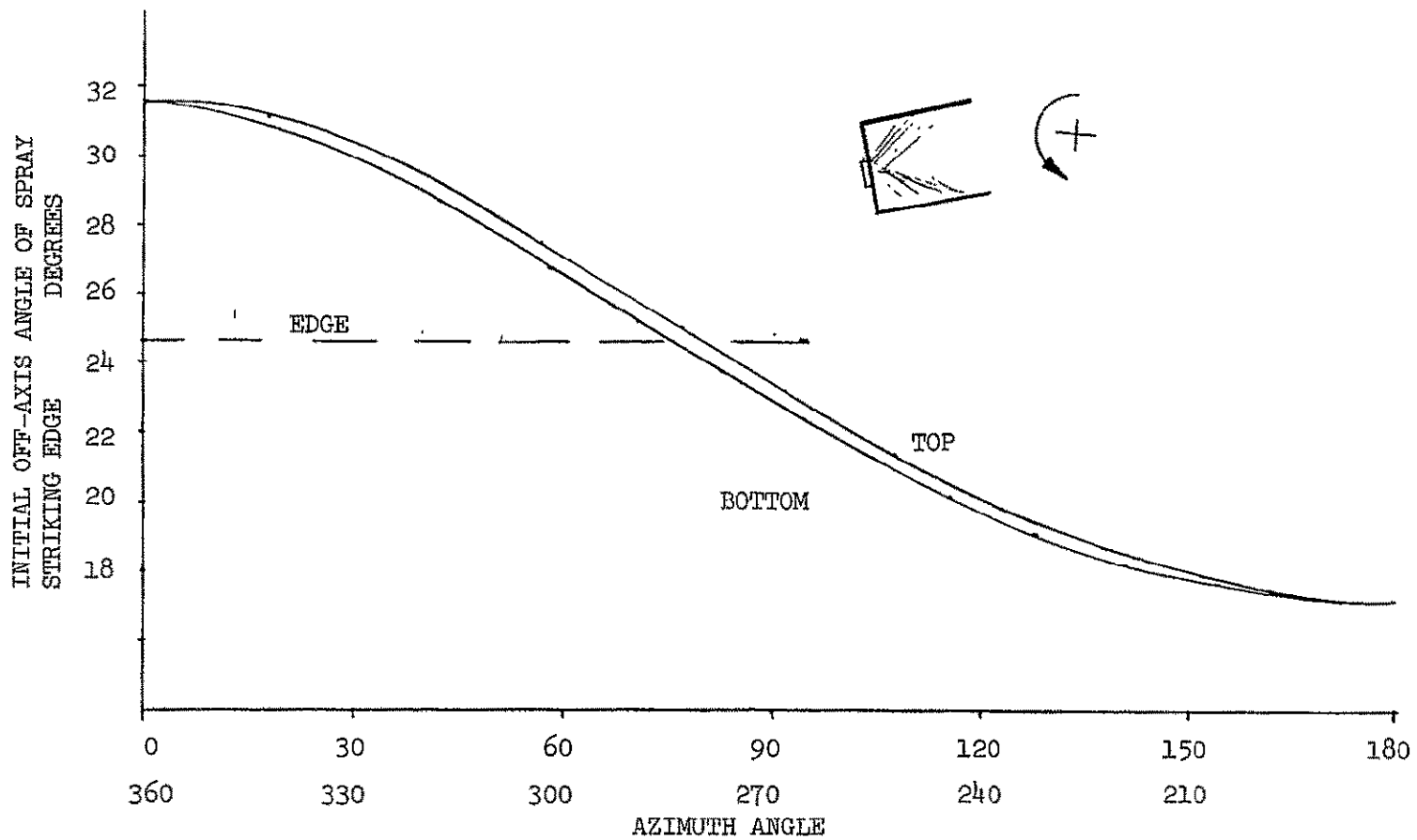


FIGURE 40 EFFECT OF SPIN TEST OF SPRAY DISTRIBUTION

Run	Calculated Percent Spilled	Relation of 4-g Force Vector and spray direction	Percent Decrease in evaporation enthalpy
37	9%	Parallel	30%
40	3%	Crossed	30%
39	7.6%	Anti-parallel	30%

As can be seen, the percent spilled and percent decrease do not agree well. Little can be said about the expected accuracy of the calculation due to the dearth of information concerning the distribution of mass in the spray. The direct liquid loss does not seem to account for the entire evaporation loss.

In the 4-g tests, some qualitative information concerning the spray pattern can be deduced from the transient cooling profiles within the evaporator. Figure 41 shows the location sketch of the thermocouples together with the transient histories recorded for each during control (1-g) and the three 4-g positions. During the water runs the thermocouple positions 2 and 4 indicated were only indirectly affected while position 3 was evidently voided of direct cooling during all the 4-g runs. This sensor was near the edge of the sprayed zone and most markedly shows the effect of the spray trajectory deflection. The remaining temperature shows the reduction experienced at one position in the local cooling due to spray distortion. All curves show less temperature drop resulting from the "lost" fluid.

The Freon 4-g runs show the effect of the liquid pool which formed. In the parallel case where the liquid was forced onto the heavy back face (position 4), a significant cooling increase was obtained. In each case, the free liquid did not strongly cool position 1 temperatures since no pooling could occur there in contrast to the 1-g runs where pooling directly above that thermocouple is known to have occurred. Positions 2 and 3 show fairly minor differences. In the anti-parallel case where the liquid was forced out the open end, the most significant loss in evaporation enthalpy was noted. The values of evaporation enthalpy which were achieved for the 4-g runs with Freon are shown in the table below:

Run	Angle between spray and 4-g force vector	Evaporation enthalpy Btu/lb
32	0° (parallel)	53
30	90° (crossed)	54.5
31	180° (anti-parallel)	34
27	1-g test (reference)	53

These 4-g runs apparently show that the water sprayed evaporator could be highly efficient during a simple, linear 4-g acceleration since only minimal spray distortion would occur. No final configuration will be used wherein the evaporant could escape as easily as in the tested configuration. For Freon the enthalpy obtained during maneuvers would depend upon

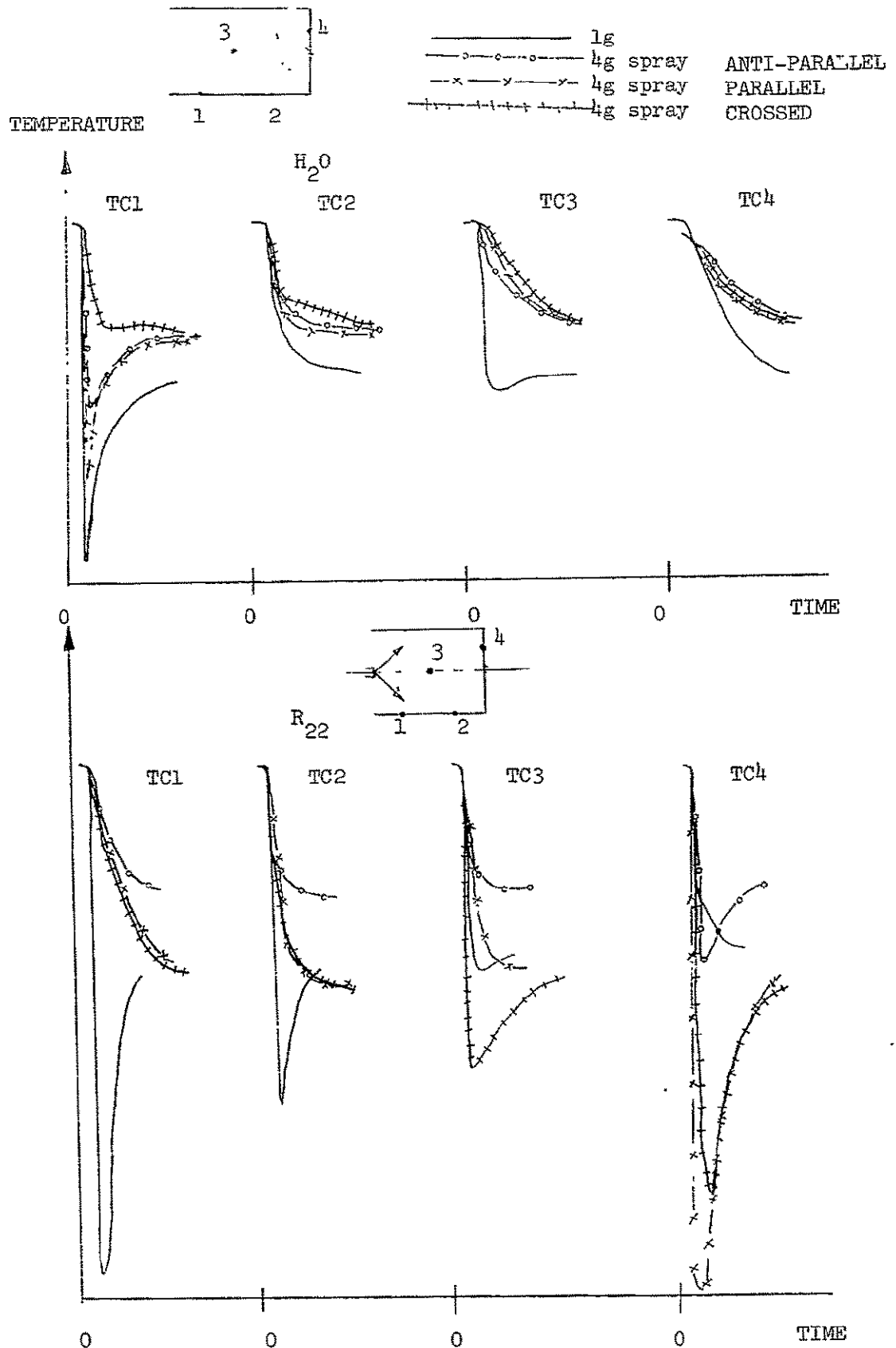


FIGURE 41 ACCELERATION EFFECTS ON EVAPORANT DISTRIBUTION

liquid containment. More consideration should be given to the problem of pooling in positions where strong cooling could result in unwanted effects.

Only 1-g runs were made with ammonia due to incompatibility of the spray with the spin fixture. It is believed that the results would be comparable with Freon results due to the similarity of 1-g operation characteristics. Runs 41-45 were conducted with NH_3 in two variations of configuration 3. In the first the spray was directed toward the thin sheet covering the open end and in the second the spray was directed at the backside of the can from the open end. The latter was superior due to better contact achieved with direct spray onto the evaporator proper. Figure 42 shows the values obtained with NH_3 as compared to the theoretical maximum expected. The effect of back pressure is as expected. Liquid spill out of the evaporator and heavy misting were noted visually much the same as for Freon.

(82)

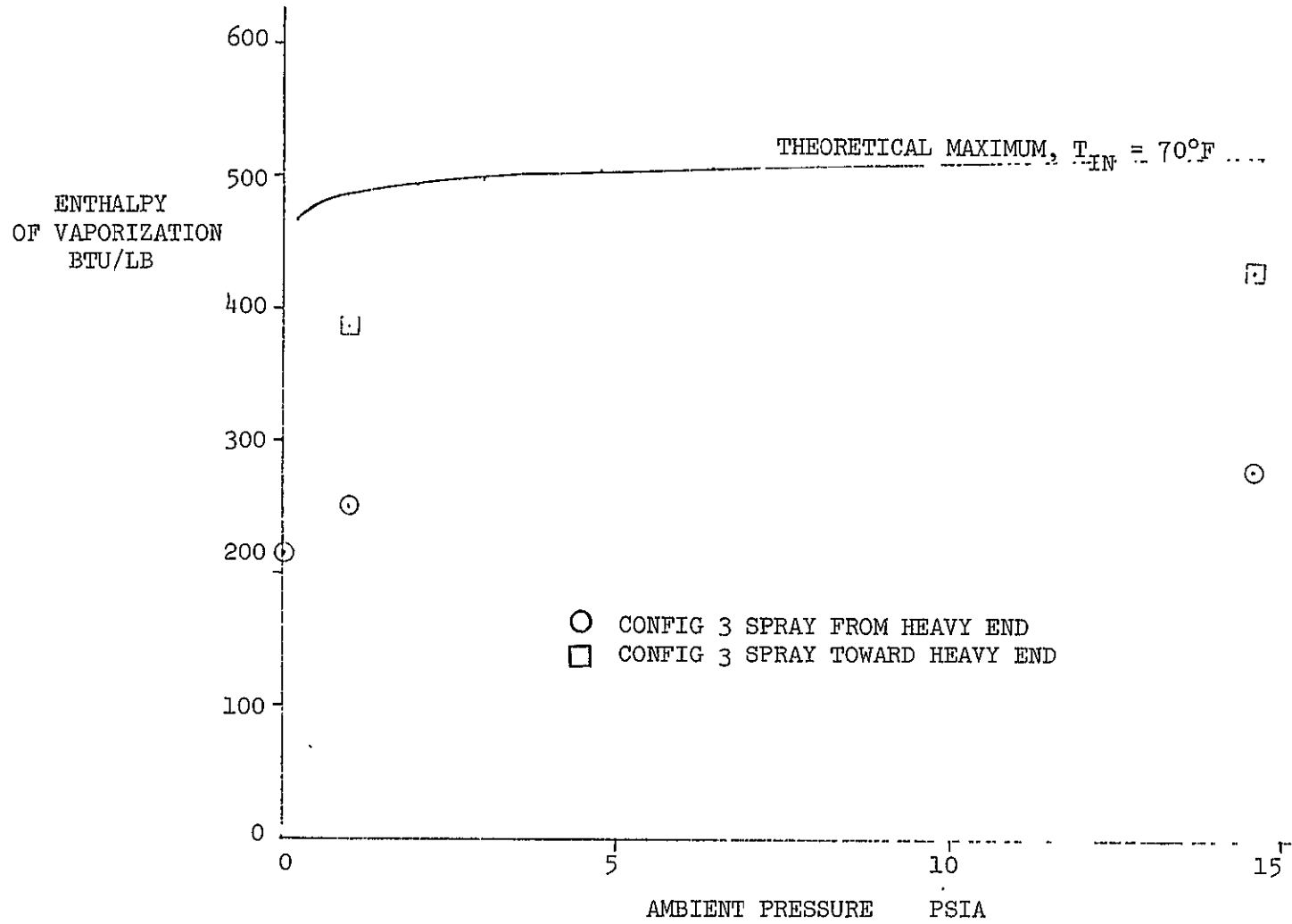


FIGURE 42 VAPORIZATION ENTHALPY ACHIEVED WITH AMMONIA

3.8 Feasibility Documentation Test

Using the concepts suggested from the preceding sections, a test was designed which would explore the feasibility of the spray evaporator. The primary emphasis of the test centered on demonstrating (1) a high fraction of evaporation, (2) the lack of a requirement for a backpressure valve, (3) controlability by supply rate modulation, and (4) the absence of any operational problems which would preclude the development of the device. Several other items were considered of interest lower than primary. These include frosting tendencies of the exit vapor tube, spray nozzle freezing problems, and simple control system suitability.

The test simulated a variable heat load by varying the inlet temperature over a prescribed schedule. Since water was used as the transport fluid, an attempt was made to circumvent freezing by maintaining its temperature above 32°F. To allow this, the control temperature limits were set at 46°F and 40°F, beyond which only about a one degree overshoot is anticipated (see Figure 28). Therefore, the minimum temperature expected is 39°F, providing all assumptions made were valid.

The construction of the evaporator was selected to provide a series, one channel tube which covers the entire active area of the evaporator. The use of a rectangular copper tube allowed a coil of the tubing to become the evaporator wall. Photographs of the evaporators during construction are shown in Figures 43 and 44. The largest gaps in the intertube space were of the order of .020, with a reasonable tightness achieved for most of the joint. The tubing was butt welded to form a continuous tube which was tacked together at about 6 to 10 inch intervals. After the tube was joined into the desired form, the active face was cleaned with acid, rinsed, covered with paste flux, heated, and saturated with molten solder; then the excess solder was wiped off with a dry cloth and the piece allowed to cool. This procedure resulted in nearly complete gap filling and yet left a solder thickness of one mil or less on a test specimen.

The evaporator was mounted in the LTV Space Environmental Systems vacuum chamber as shown schematically in Figure 45. Photographs of the installation are shown in Figures 46, 47, 48, 49 and 50. Measurements were made of chamber pressure, evaporator internal pressure, current evaporant supply weight, current evaporant and contents weight, transport loop flow rate, and transport loop pressure drop. In addition, temperatures of all fluids were measured at locations indicated by the sketch in Figure 51.

In each run sequence, the following procedure was followed. A full load condition was set up at steady state; from which the location of the thermocouple at (or nearest) the downstream end of the cooled section was determined. Using this thermocouple as a control sensor, a profile run was initiated. Following the profile run and a dormant period, the second profile run was initiated. This sequence was repeated for variations in evaporator and fluid. For the NH₃ and Freon evaporants, duplicate runs with ambient pressures of 1 psia and 14.7 psia were run. For the water evaporant, an increased load of about 70 percent was conducted for both evaporators.

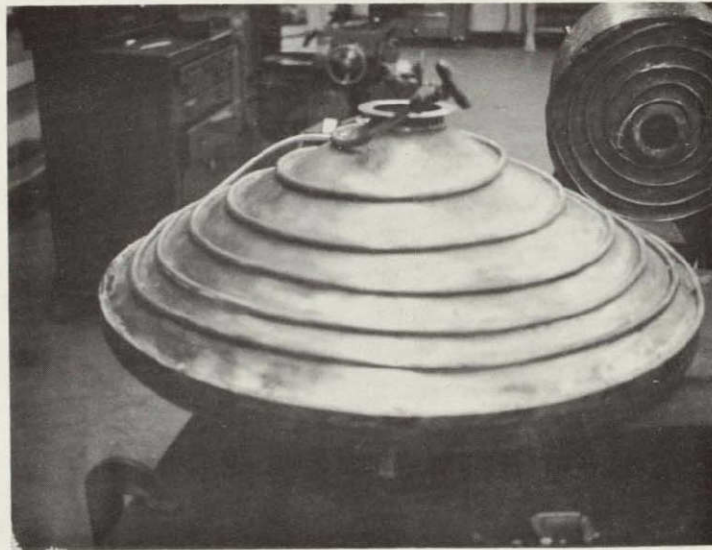


FIGURE 43 PLATE EVAPORATOR UNDER CONSTRUCTION

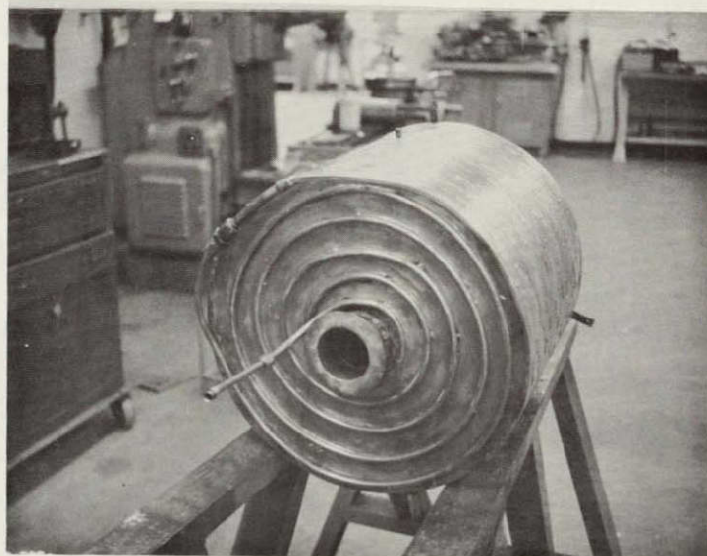
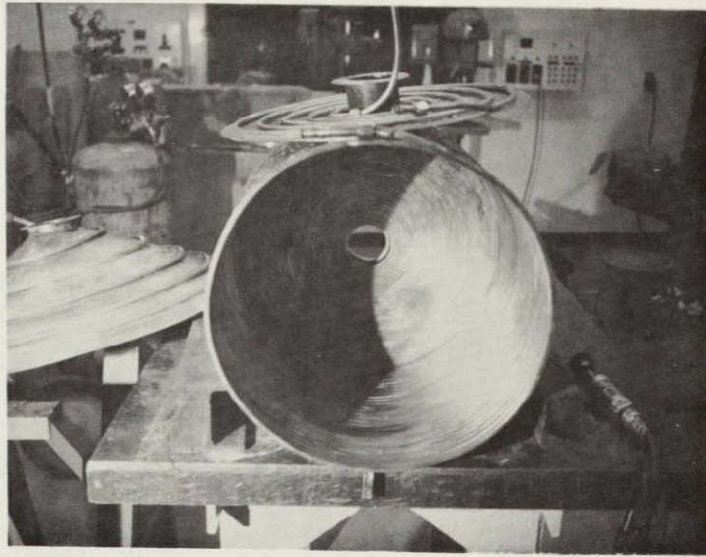


FIGURE 44 CYLINDRICAL EVAPORATOR UNDER CONSTRUCTION

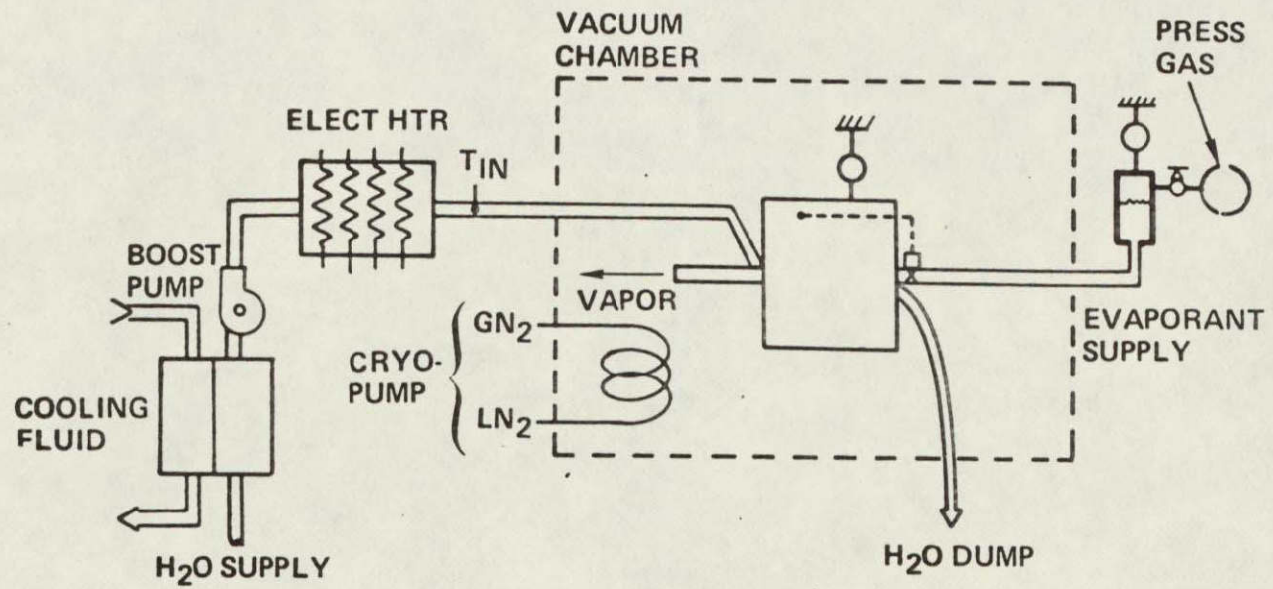


FIGURE 45 SCHEMATIC OF TEST INSTALLATION

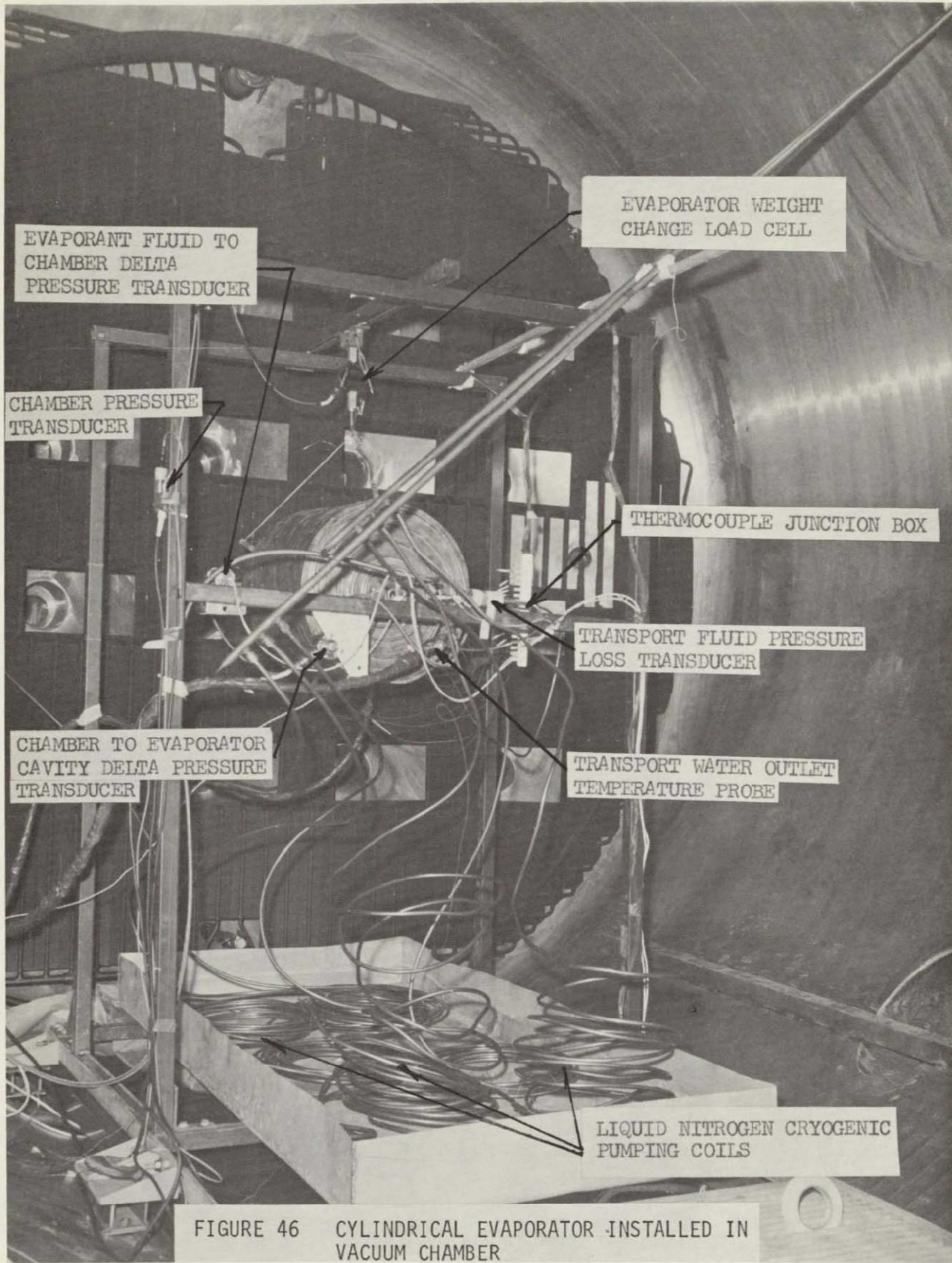


FIGURE 46 CYLINDRICAL EVAPORATOR INSTALLED IN VACUUM CHAMBER

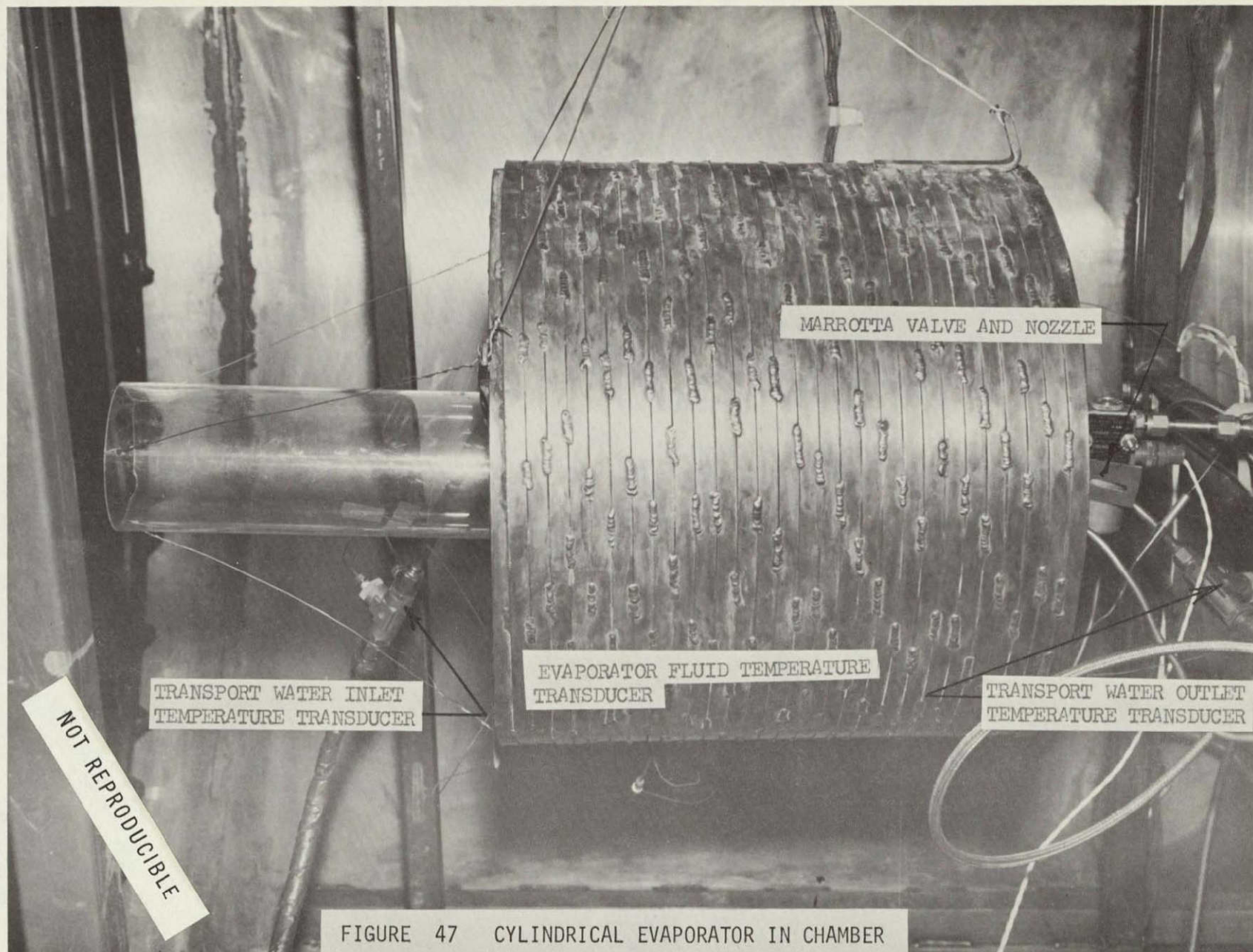


FIGURE 47 CYLINDRICAL EVAPORATOR IN CHAMBER

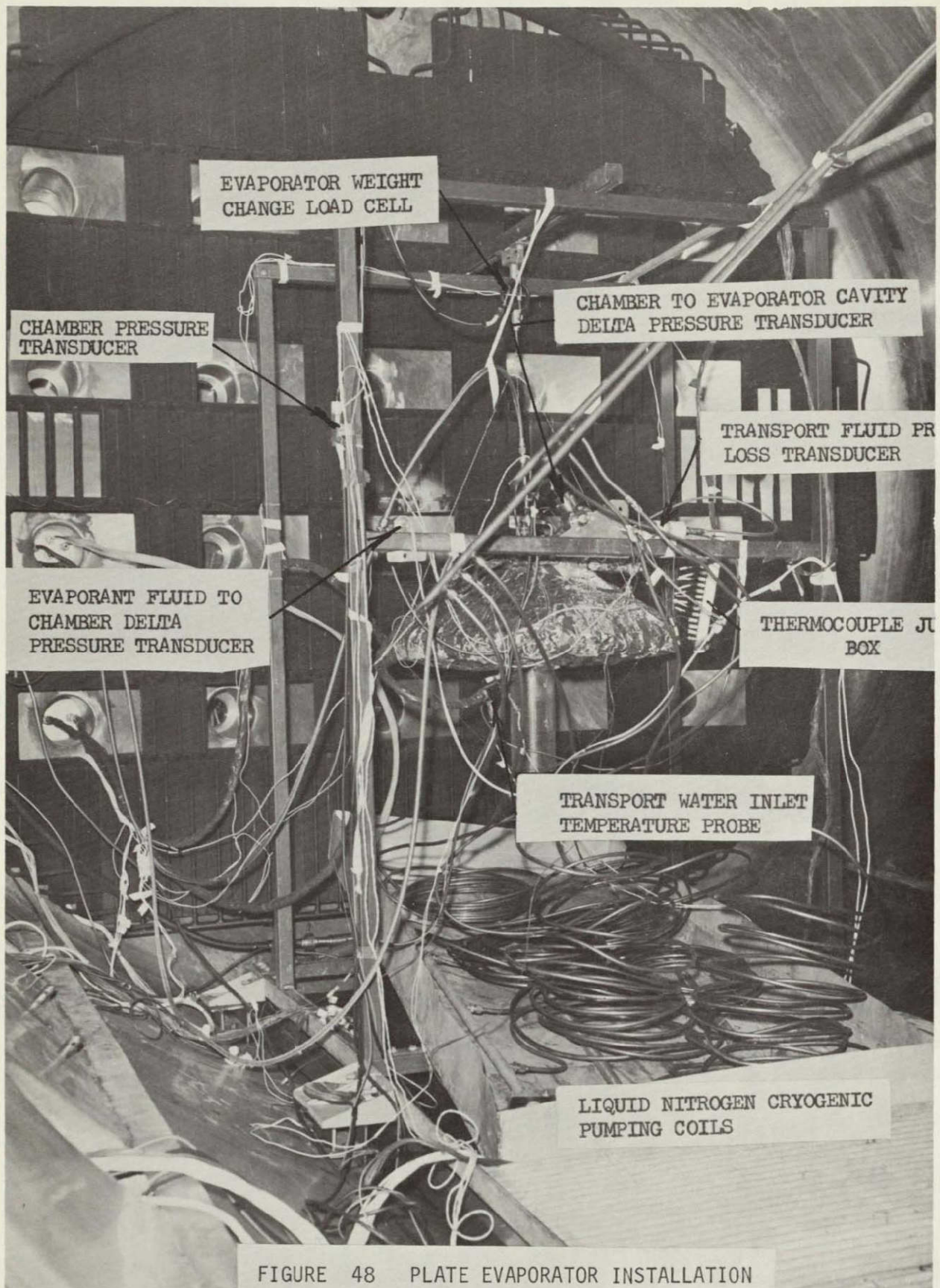
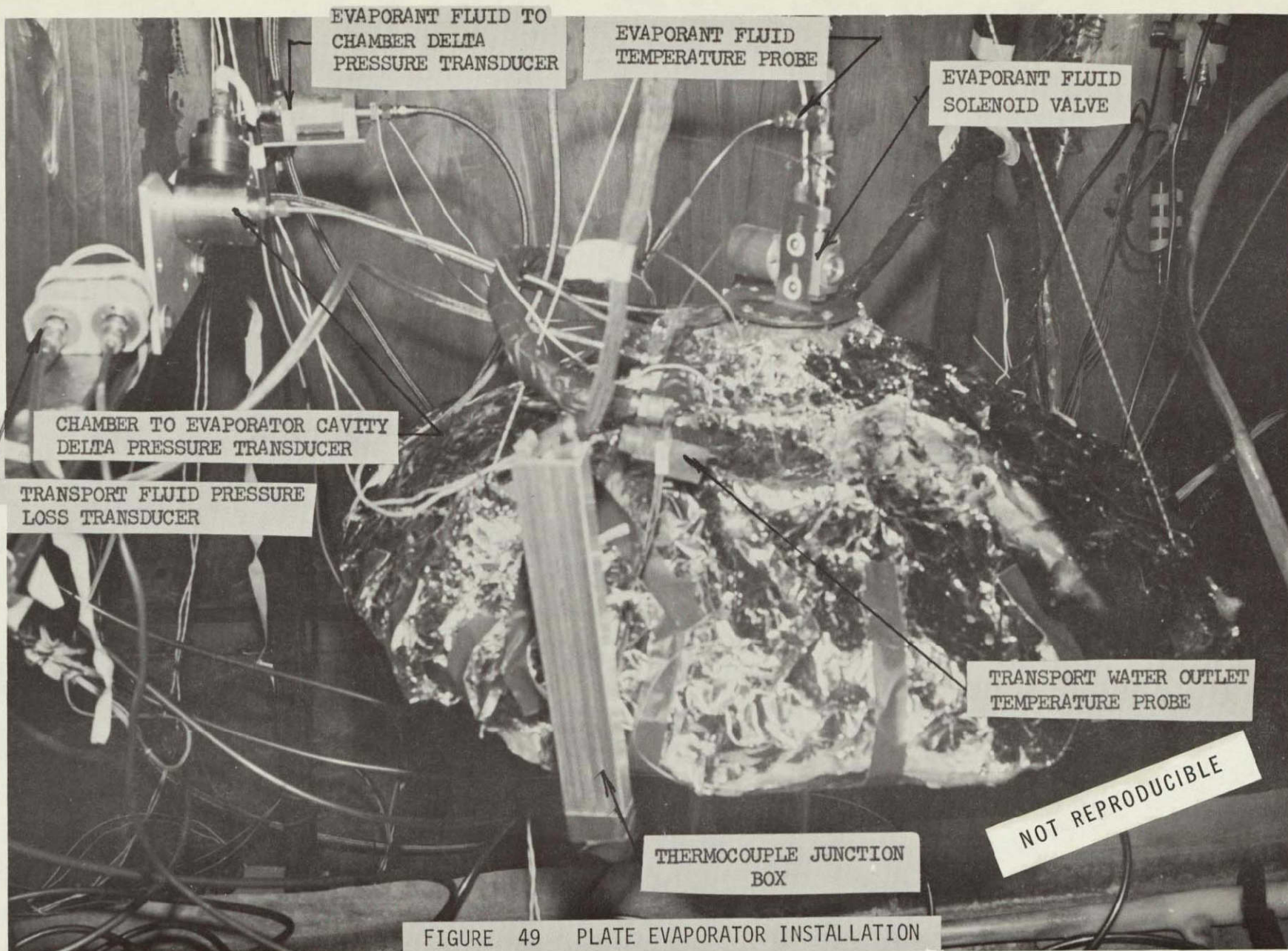
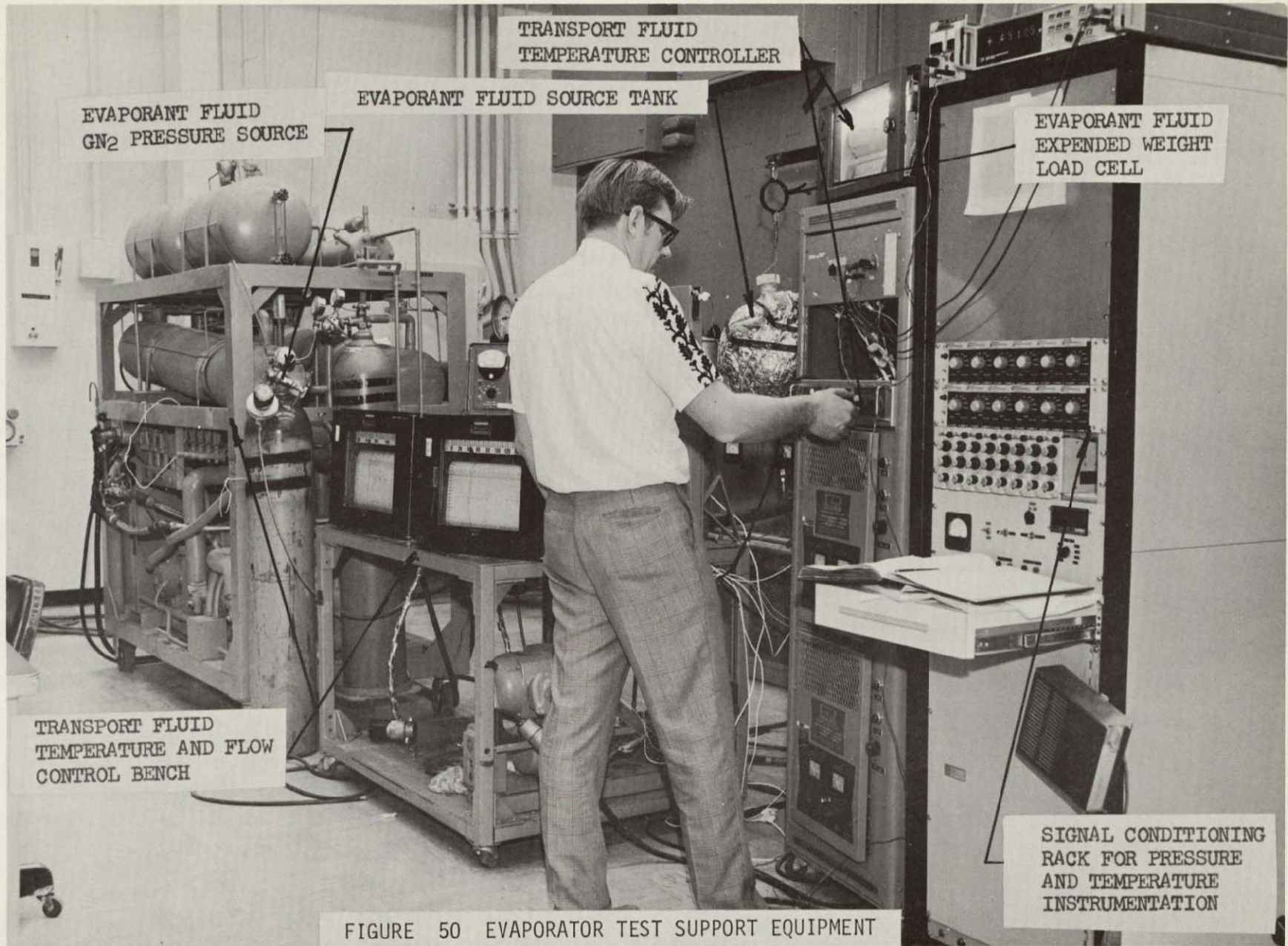


FIGURE 48 PLATE EVAPORATOR INSTALLATION

(96)





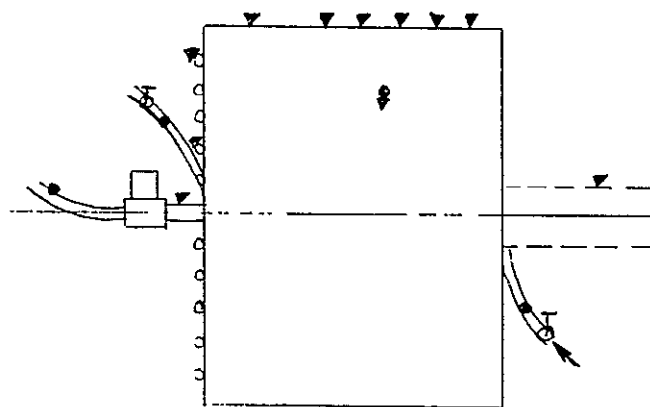
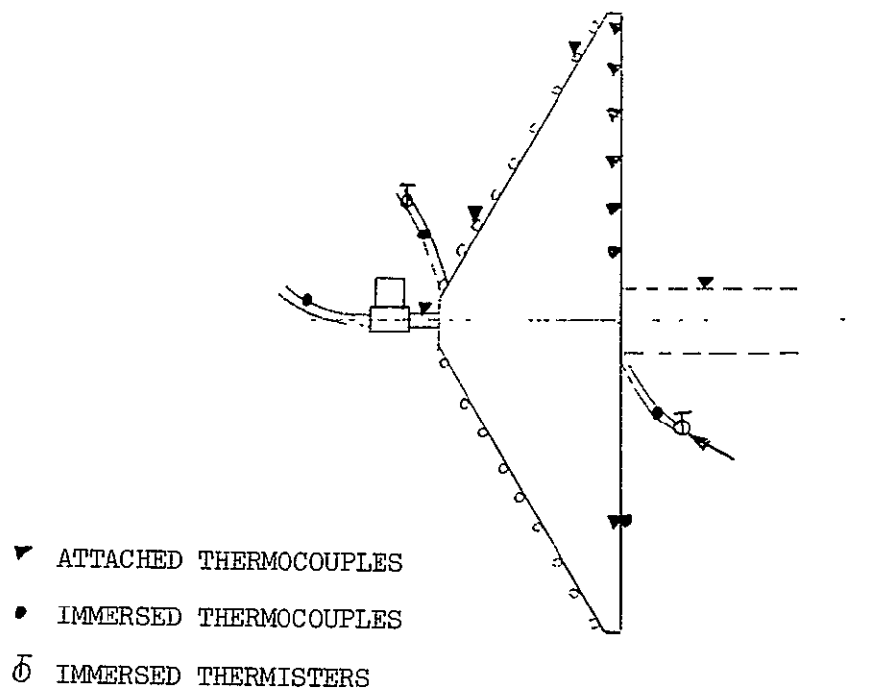


FIGURE 51 TEMPERATURE INSTRUMENTATION LOCATIONS

Figures 52 through 59 display the inlet and outlet temperature profiles and the evaporant use for the runs conducted. The runs in Figures 52 and 53 (cylinder, Freon 22) display two separate features which are important to note. In the first, about midway through the run the flow rate of transport fluid dropped momentarily due to incipient freeze up. At the end of the run, the transport line was frozen. The dual temperature control was accomplished partly by automatic control for the sensor in the evaporator and partly by a manual control using the displayed outlet temperature as reference. The outlet control was manually switched on and off at 35°F. The outlet temperature near the time in question was approximately 34 degrees but the evaporator was turned on by mistake resulting in a quick freeze up. The result obtained was not considered to be compromised seriously since the run was essentially complete. In the second (Figure 53), the Freon supply was exhausted before the run was completed. Neither of these runs was duplicated due to a lack of available evaporant. The relative completeness of these runs was judged adequate to demonstrate the function of the evaporator; therefore the expense of additional evaporant and model setup time was not considered justified.

In the water runs, Figures 54 through 57, considerable freezing of the spray nozzle was encountered, a complete account of which will be considered later. With water in each evaporator, the single on-off control functioned satisfactorily and no control or transport freezing problems were encountered. Some overshoot of the prescribed 35 to 45 degree band was noted to limits of 34 and 46 except for a single excursion to 50°F. In the ammonia runs, Figures 58 and 59, overshoot of the prescribed control band was noted up to about 50 degrees maximum temperature on two occasions. A dual sensor control was again required to prevent freezing as in the Freon runs. Less freezing tendency was encountered for ammonia than for Freon which is assumed to be due to the fact that the profile runs were performed at 1 psia where the vapor flow influence on the spray distribution is decreased.

The most significant difficulty in obtaining a complete run was encountered with the plate configuration and Freon as evaporant. Several attempts with the dual sensor control setup were attempted but each time the transport fluid was frozen. An attempt to locate the frozen portion showed that the actual freezing occurred near the evaporant outlet (transport inlet) but the first thermocouple did not register cold enough to freeze even though at its projected temperature freezing would have been encountered within a few seconds. This problem is fairly severe since it indicates that the heat fluxes in the neighborhood of the transport inlet are extremely high. The apparent account for the difference in the cylinder and plate behavior is due to physical orientation. With the extreme fluxes encountered in each configuration, some accumulation occurs, which in the horizontal position falls to the bottom and pools. In contrast, the plate was mounted pointed downward where the fluid was driven toward the exit by the vapor. This accumulated liquid continued to cool the high flux location for a brief time after the supply was cut off, thus aiding the freezing.

The thermodynamic results of these tests are shown in Table 5. There seems to be no pattern established to yield the reason for variability

(76)

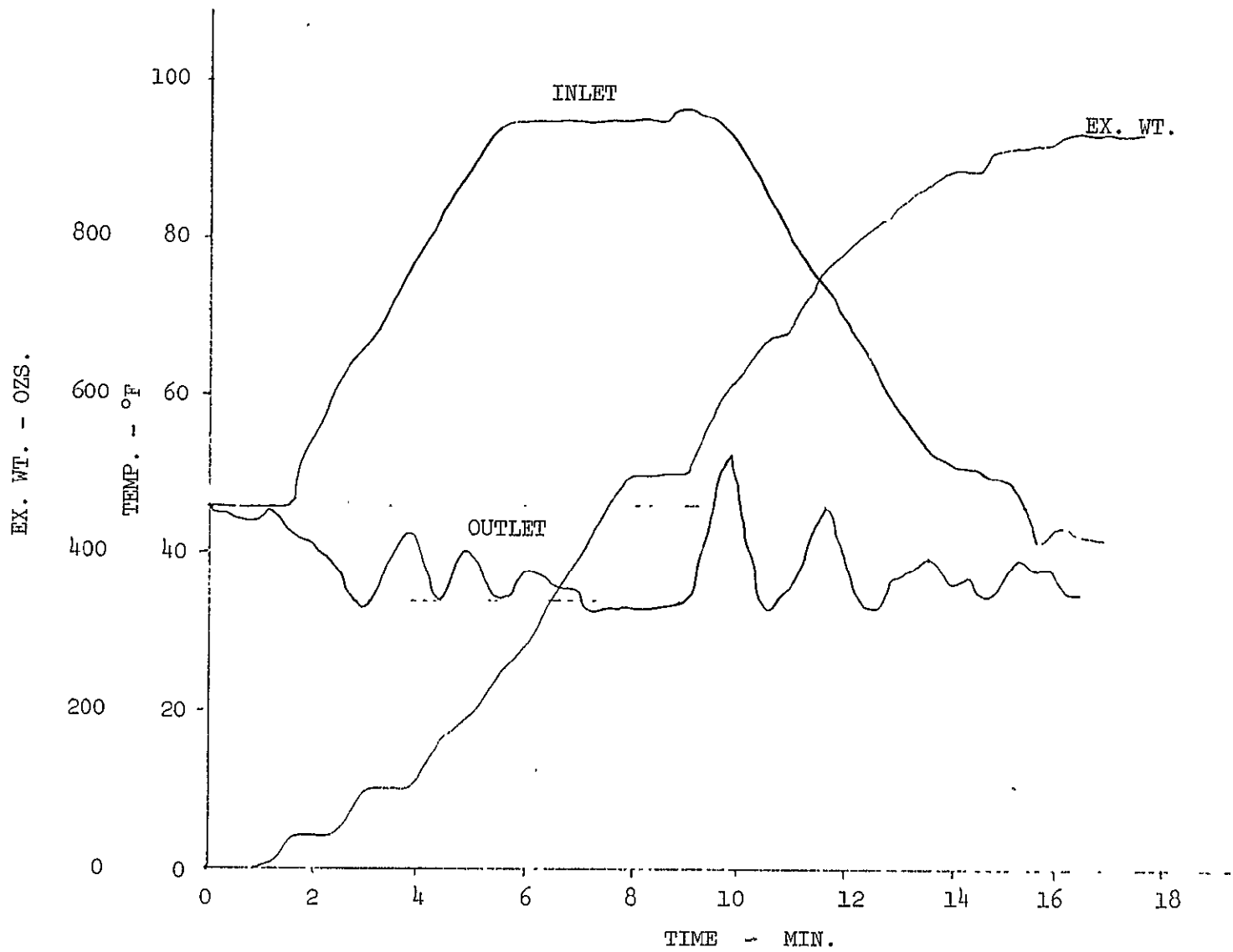


FIGURE 52 THERMODYNAMIC RESULTS - FREON 22 - PROFILE 1 - CYLINDER

(95)

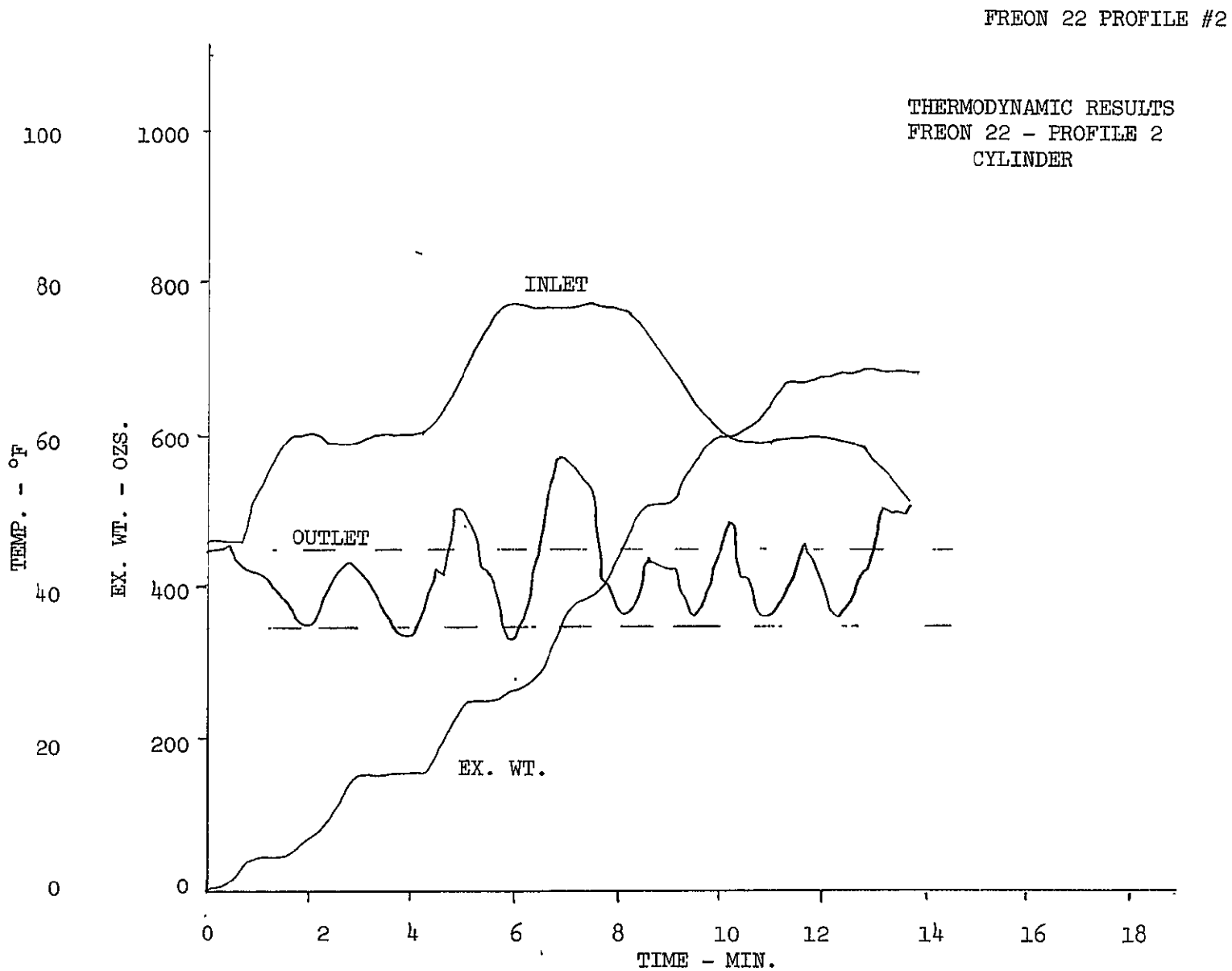


FIGURE 53 THERMODYNAMIC RESULTS - FREON 22 - PROFILE 2 - CYLINDER

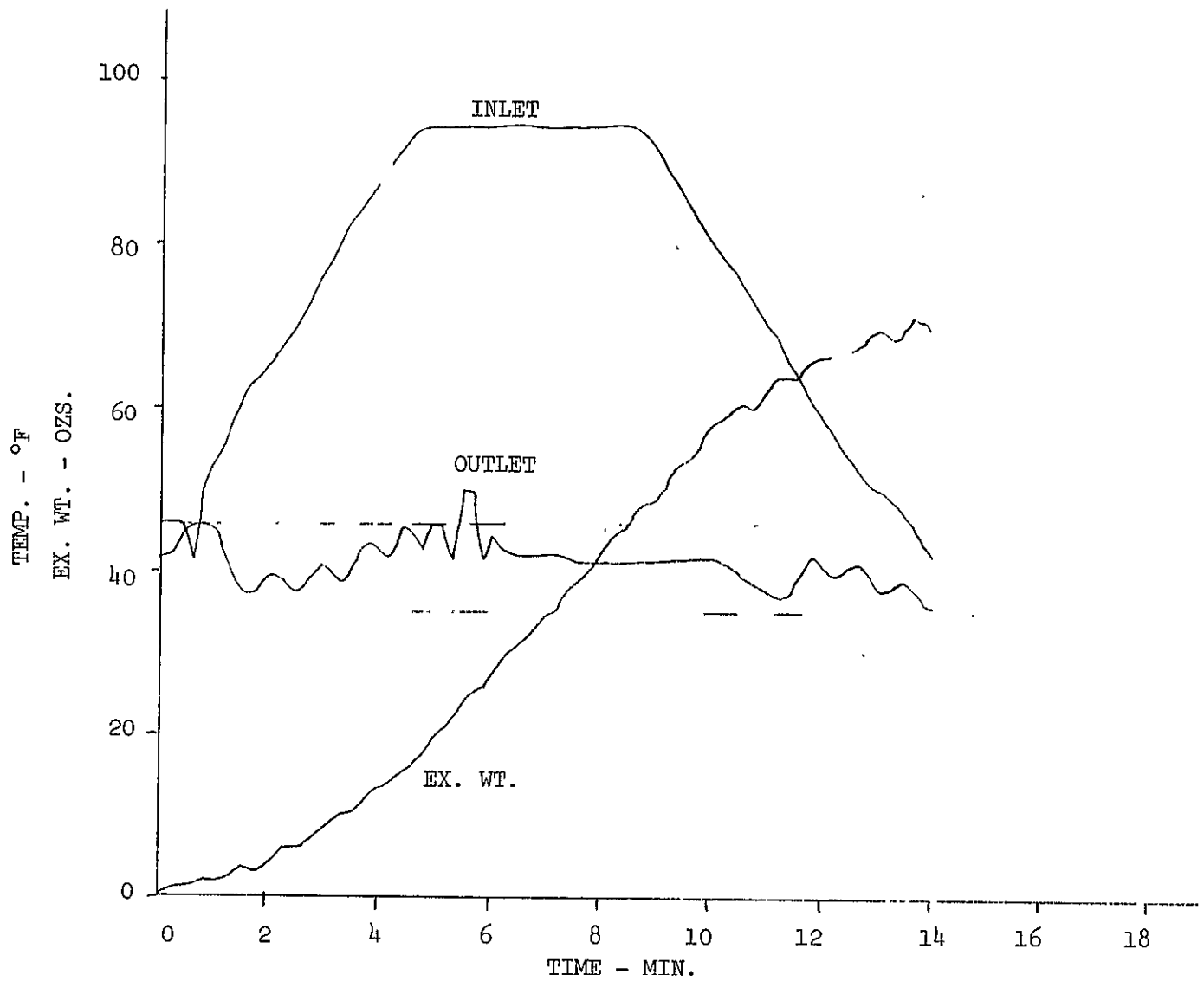


FIGURE 54 THERMODYNAMIC RESULTS - H₂O - PROFILE 1 - PLATE

(97)

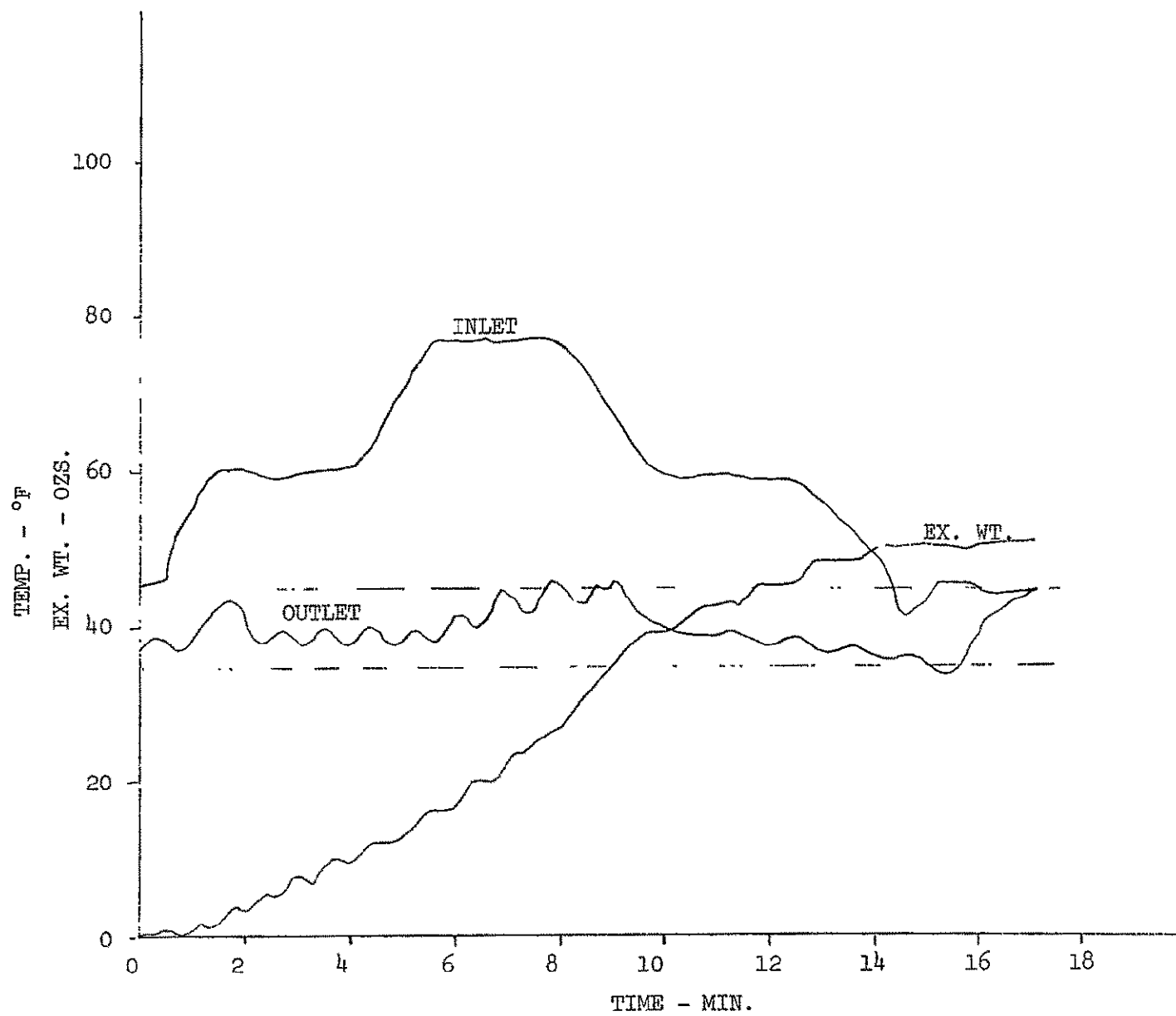


FIGURE 55 THERMODYNAMIC RESULTS - H₂O - PROFILE 2 - PLATE

(86)

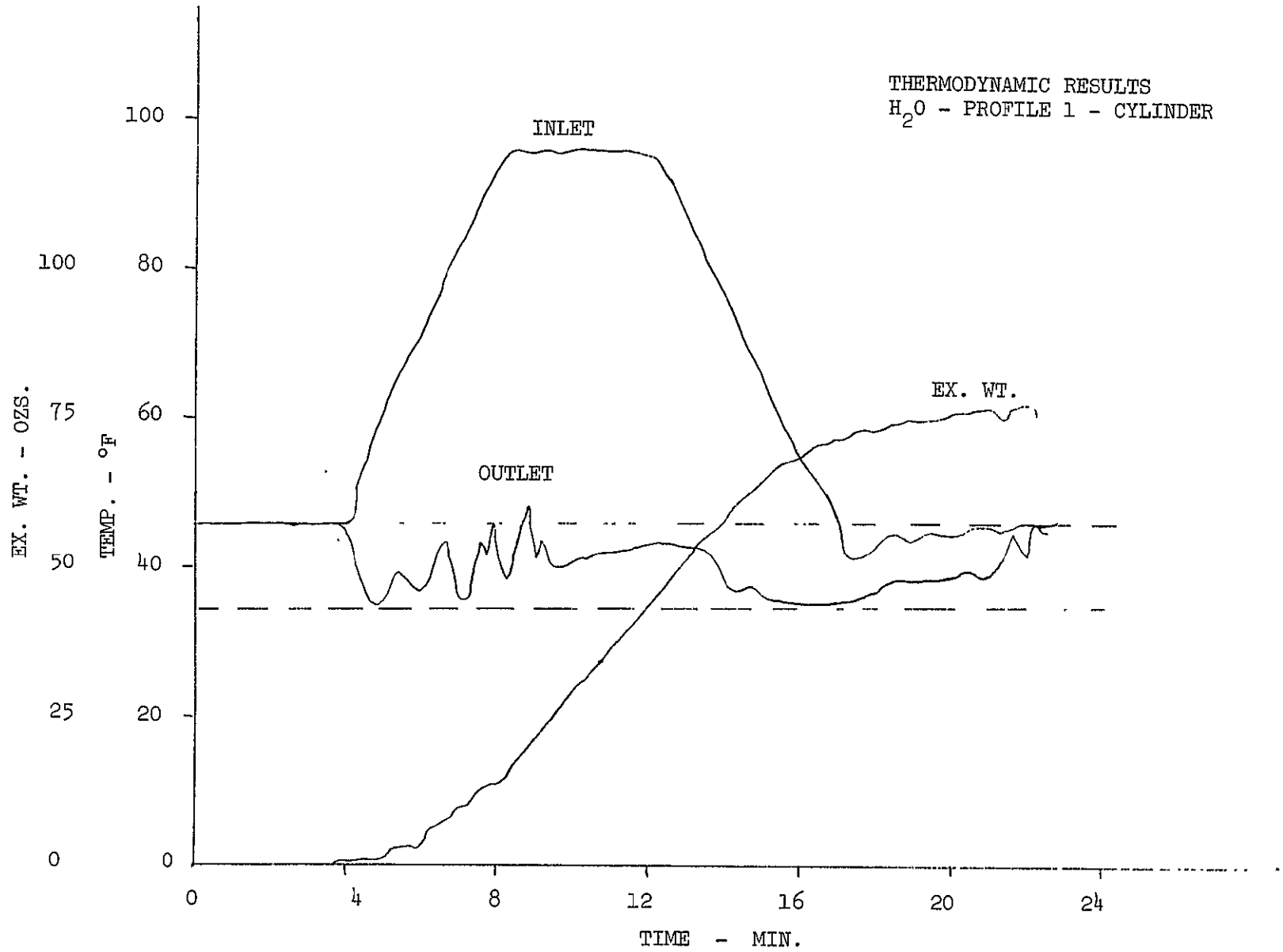


FIGURE 56 THERMODYNAMIC RESULTS - H₂O - PROFILE 1 - CYLINDER

(66)

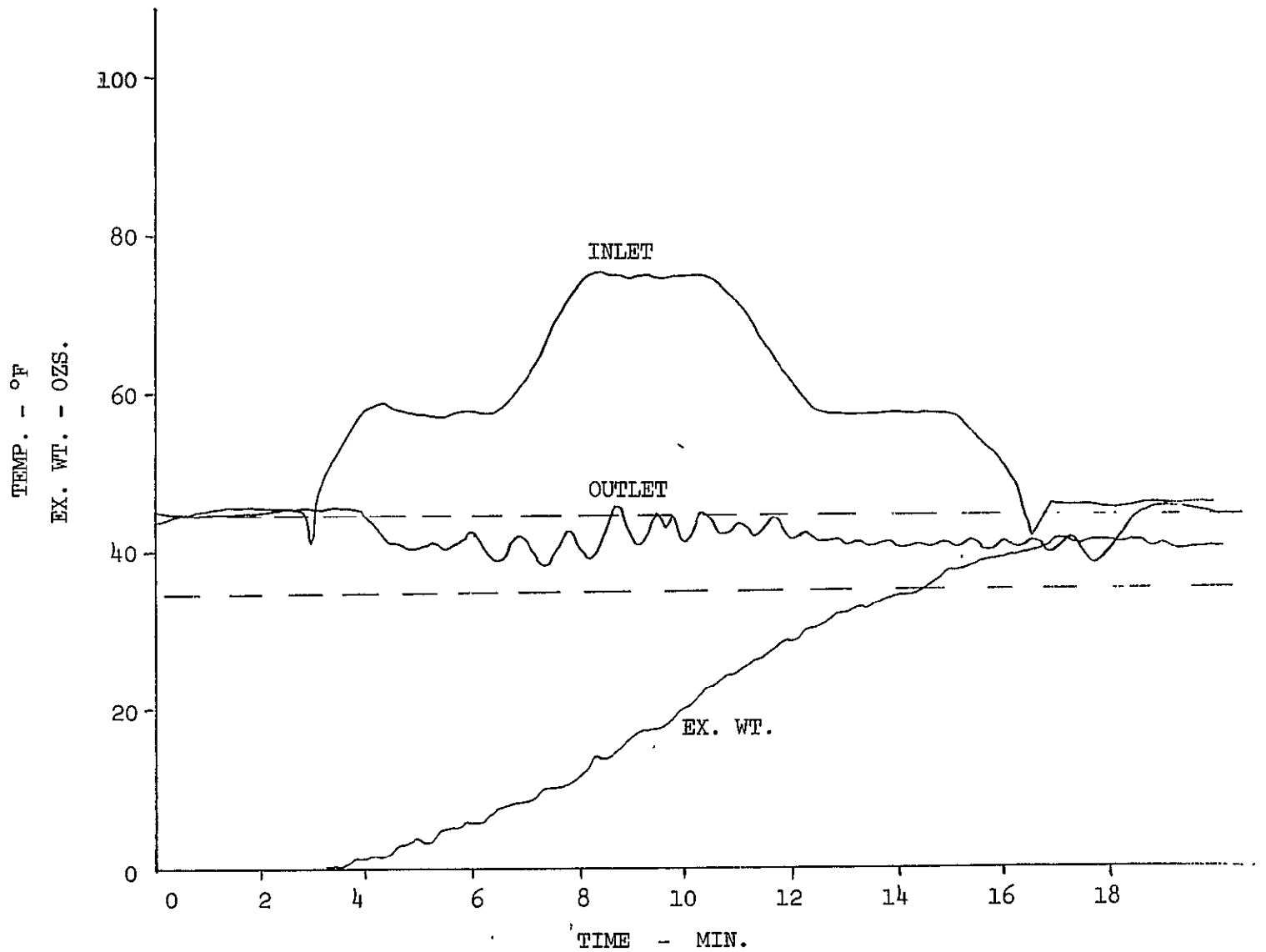


FIGURE 57 THERMODYNAMIC RESULTS - H₂O - PROFILE 2 - CYLINDER

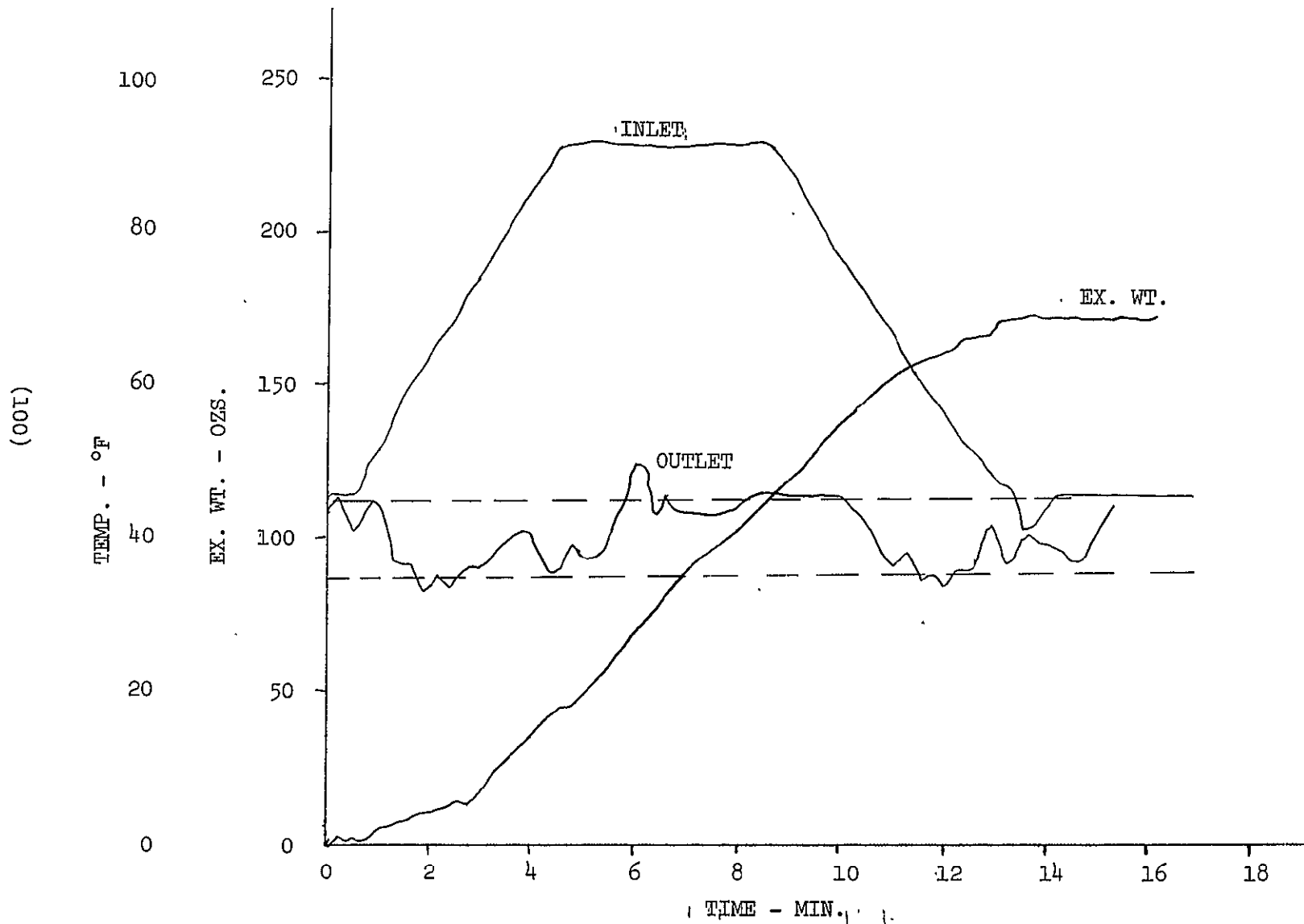


FIGURE 58 THERMODYNAMIC RESULTS - NH₃ - PROFILE 1 - PLATE

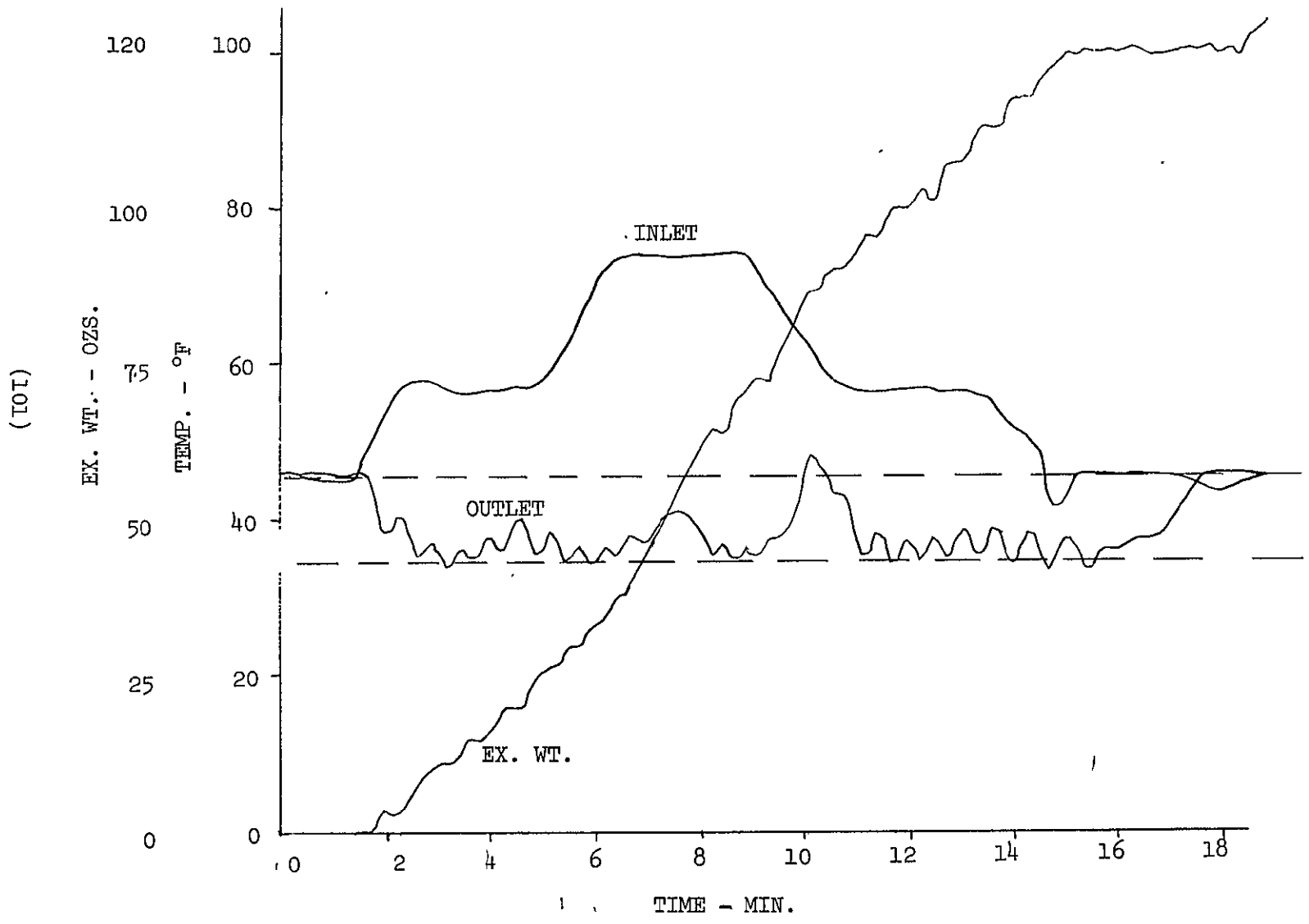


FIGURE 59 THERMODYNAMIC RESULTS - NH₃ - PROFILE 2 - PLATE

of the water data. A brief explanation of the sources of random error are given at this point since the variation in observed enthalpy might well be due to basic data accuracy limitations. First, the flow rate measurement random error should not exceed 2 percent, while the expended weight is valid to one ounce. One ounce of water represents 2.5 percent in profile 2 and 1.4 percent in profile 1. In the steady state runs, the slope of the graph weight versus time was used to estimate the weight flow rate to an estimated 4 percent resolution. Computation of the value of the heat rejection integral $\int \dot{w} C_p (T_{in} - T_{out}) dt$ is estimated to be within 4 percent.

including the flow rate uncertainty. Data output density is one complete set per 11 seconds which should be adequate for the above estimated accuracies. There also exists the possibility of systematic errors in flow rate of not over 2 percent (equivalent to the random error estimate); in expended weight of 2 percent; and in temperature of 0.3°F representing 3 percent in a common run. Thus, the results are stated as enthalpy effect equals 965 Btu/lb ± 7 percent of systematic nature and ± 8 percent of a random nature. Neglecting any possible systematic error, one could anticipate measured values from 890 Btu/lb to 1040 Btu/lb due to random errors in data acquisition and reduction. A similar statement applies for NH₃ and Freon where the values of random error nearly span the values of enthalpies obtained. The information in Table 5 represents all the thermodynamic data acquired and are felt to demonstrate a high liquid use efficiency.

The distribution of cooling within the evaporator has been deduced from a consideration of the temperatures measured in the transport line at steady state full load. For clarity the length of flow path to and angular position of each thermocouple has been calculated. From these, the cooling effect per unit length or the aggregate cooling to a particular sensor may be calculated. The latter has been presented to avoid the speculation involved in calculating its derivative from the mean value. The results of this calculation are shown in Figures 60, 61, and 62. This presentation illustrates convincingly the extreme non-uniformity of the NH₃ and Freon cooling effects. Also the water runs demonstrate effectively identical spray patterns as shown in the cooling effect versus angular position plot. On a per unit length basis, the water spray is more uniform than for the other evaporants which accounts for its superior controllability.

The problem of spray nozzle freezing was encountered frequently during the testing with water. During test 1 conducted earlier, identical nozzles in somewhat different plumbing arrangements were not susceptible to freezing. While it is felt that the freezing tendency may be eliminated entirely by the development of an appropriate nozzle/valve integration, the data are presented as determined in the test.

The freezing phenomenon follows a consistent sequence. First the nozzle is spraying liquid at a steady rate. The temperature about one half inch back of the nozzle shoulder and the inlet evaporant temperature are nearly the same at about 70°F. The nozzle flow is stopped by a valve in the line, but the trapped liquid boils in the line and "dribbles" out the exit. The liquid contacts the face of the nozzle, where it changes to solid and vapor in a period not indicernable visually, perhaps one second. The ice thus formed usually "chips" off the nozzle and more liquid

TABLE 5 THERMODYNAMIC RESULTS

EVAPORATOR	PROFILE OR LOAD	EVAPORANT	NET ENTHALPY BTU/LB
Plate	Profile 2	H ₂ O	912
Plate	Profile 1	H ₂ O	970
Plate	Full Load	H ₂ O	1010
Plate	Increased Load	H ₂ O	907
Cylinder	Half Load	H ₂ O	890
Cylinder	Full Load	H ₂ O	1045
Cylinder	Increased Load	H ₂ O	893
Cylinder	Profile 2	H ₂ O	1020
Cylinder	Profile 1	H ₂ O	1040
		Average	965
Plate	1 psia Full Load	Freon 22	56.4
Plate	14.7 psia Full Load	Freon 22	63.5
Cylinder	14.7 psia Full Load	Freon 22	59.5
Cylinder	14.7 psia Profile 1	Freon 22	72.4
Cylinder	14.7 psia Profile 2	Freon 22	61.
		Average	62.5
Plate	1 psia Profile 2	NH ₃	365
Plate	1 psia Profile 1	NH ₃	332
Plate	1 psia Full Load	NH ₃	387
Plate	14.0 psia, Full Load	NH ₃	344
		Average	357

(401)

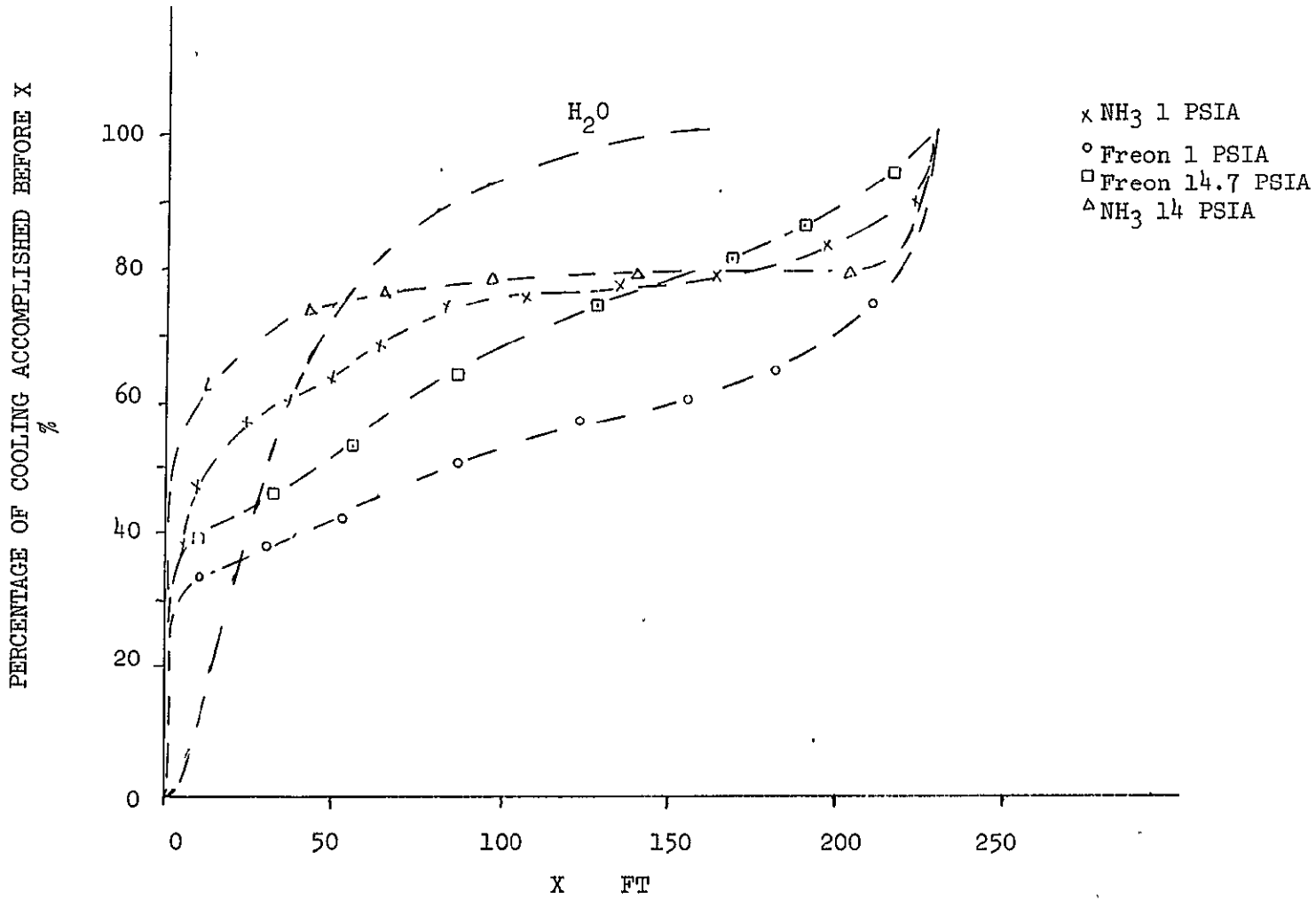


FIGURE 60 COOLING DISTRIBUTION PER LENGTH IN PLATE

(501)

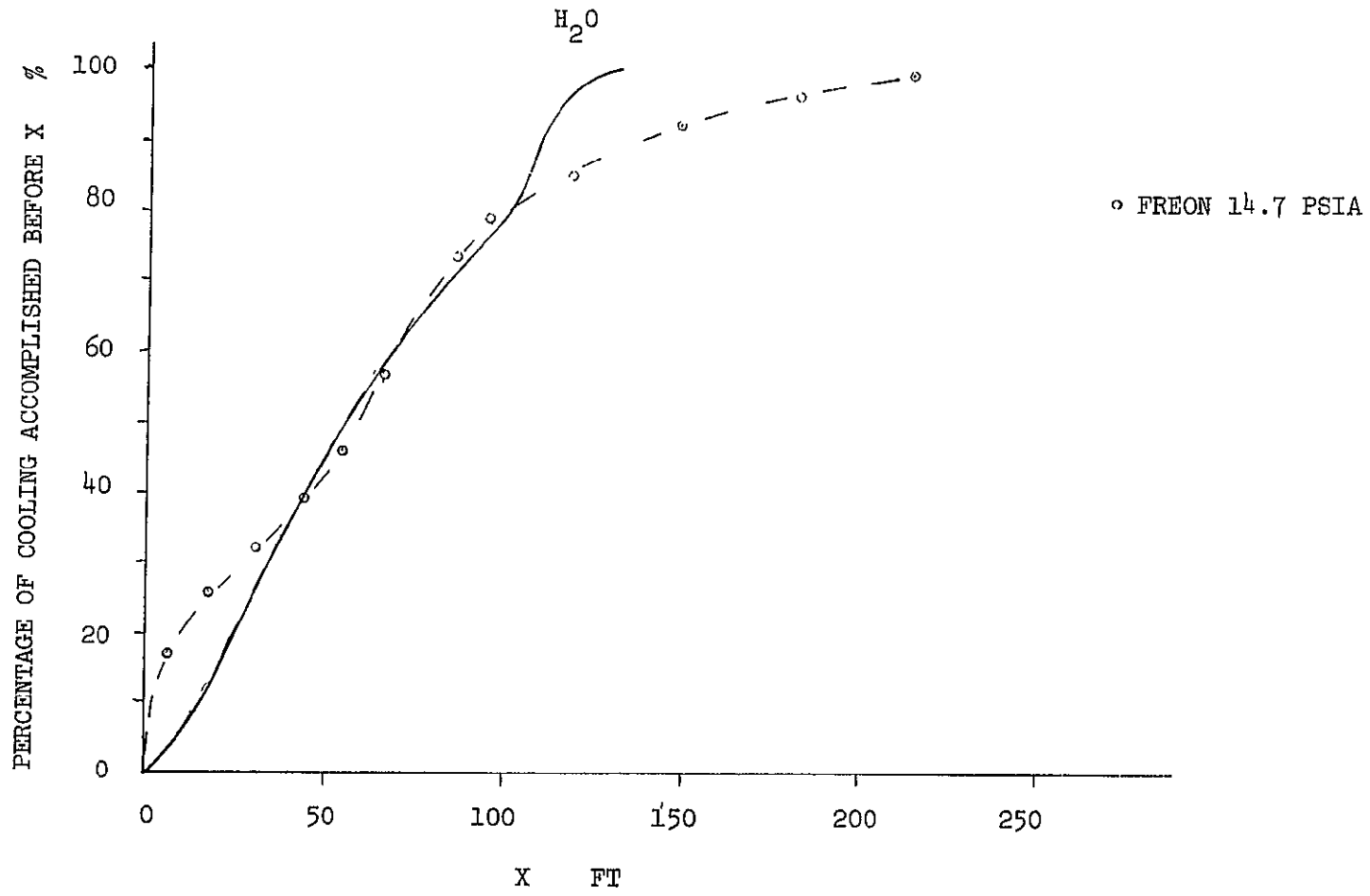


FIGURE 61 COOLING DISTRIBUTION PER LENGTH IN CYLINDER

Σ ⊕ Σ

(106)

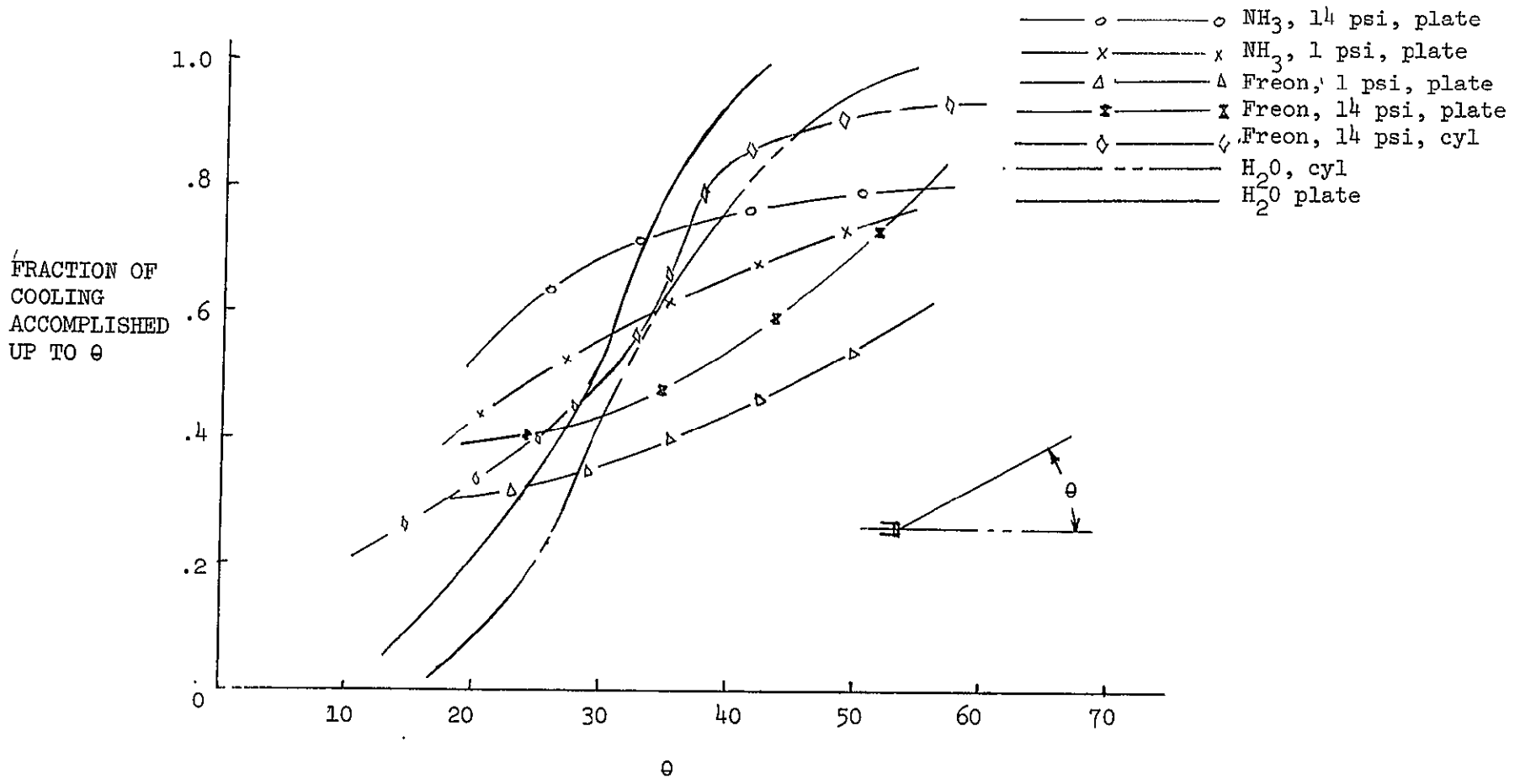


FIGURE 62 DISTRIBUTION OF EVAPORANT WITH ANGLE

TABLE 6 NOZZLE FREEZING DATA

CONFIGURATION	LIQ HOLD UP	ORIENTATION	HEAT TEMP CONTROL	INSULATION TEMP 40° EVAP	LIQUID PRESS (PSI)	PURGE PRESS (PSI)	ESTIMATED FREEZE PROBABILITY
Brass Fitting SS Nozzle	10cc	Down	None	Infinite	20-70	None	Not Possible (BELLJAR)
SS Fitting SS Nozzle	3cc	Horiz. Sl. Up	Up to 120°F	Slight	20	None	Large 70.5
SS Fitting SS Nozzle	3cc	Horiz. Sl. Up	None	Infinite	85	None	Large (BELLJAR)
SS Fitting SS Nozzle	3cc	Horiz. Sl. Up	Up to 120°F	Slight	20	25. Helium	1/3
SS Fitting SS Nozzle	3cc	Horiz. Sl. Up	Up to 120°F	Slight	20	100 Helium	1/50
SS Fitting Brass Joint SS Nozzle	6cc	Horiz. Sl. Up	None	Infinite	85	None	None Observed (BELLJAR)
SS Fitting Brass Joint SS Nozzle	6cc	Horiz. Sl. Up	Up to 100°F	Slight	20	None	1/20
SS Fitting Brass Joint SS Nozzle	6cc	Horiz. Sl.	Up to 100°F	Large	20	None	1/20
SS Fitting Brass Joint SS Nozzle	6cc	Down	80°F	Large	20	None	1/2
SS Fitting SS Nozzle	3cc	Down	80°F	Large	20	100 N ₂	None
SS Fitting Brass Joint Brass Nozzle	6cc	Horiz. Sl. Up	None	Slight	20	None	None

(107)

exits, repeating the sequence. Sometimes however the solid adheres to the nozzle and the liquid which flows out freezes quickly into a dendritic structure. This treelike form continues to grow as the liquid finally is purged from the nozzle. The nozzle temperature is observed to fall and the heater, if any, begins to function. Despite the heater, the ice fails to cleave from the nozzle. As soon as the evaporator function is required a fresh spurt of water floods the ice structure and now freezes as fast as it is supplied. This freezing in grotesque shapes continues as long as the liquid is supplied. At the same time, the evaporator sensor temperature rises, no heat being added to the evaporant.

Several attempts to prevent freezing were made, as shown in Table 6. Among these items were adding a heater to the nozzle which had no effect, coating the nozzle surface with a non-wetting agent which may have reduced the freezing tendency somewhat - it then grew the tree from the hole directly - and adding an insulator between evaporant valve and evaporator transport loop which had little effect. Then a gas purge line was added to the line between the valve and nozzle. The purge pressure was adjusted in increments with a fixed purge time of about 1 second. The purge was effective but after perhaps 50 cycles another freezing condition occurred.

During this time, the recollection of the lack of problems associated with the earlier test drove us to reproducing the earlier set up. The second test set up had all stainless steel materials and about 3 cc liquid hold up. The first test had a combination of brass and stainless steel materials with 10 cc liquid hold up. The actual nozzle was identical. In the former test a heavier valve was used, but had the same power dissipation as the present valve. No heater was used in the first test. Installation of the brass/stainless steel plumbing resulted in nearly faultless operation - again some 50 cycles were accomplished but freezing finally occurred. Since the brass insert with its greater heat capacity and transfer rate capability was evidently responsible for some difference, a brass nozzle was ordered. While waiting for its arrival, other runs were made with Freon and finally with water - this time spraying downward with the brass fitting in the line. This configuration most nearly duplicated the former test, but the same result of freezing occurred again. This time the evaporant was cooled and frozen inside the nozzle which effectively blocked the flow. Upon replacing the purge setup in the downward spraying direction, a successful operation was allowed on all the plate configuration runs. Upon re-installing the cylinder with a brass fitting and brass nozzle, a profile was run with no heater and a strong thermal connection to the evaporator - about the worst condition of any attempted earlier. No freezing was encountered.

The detailed analytical study and experimental program presented in the foregoing technical discussion have established the feasibility of the flash evaporator concept. The promise shown by the flash evaporator concept to date warrants early definition of the general form of the evaporator development program, so that program planning can proceed without delay. The purpose of this section is to outline the tasks to be performed to bring a flash evaporator system to a flight prototype status. The phases of the program and the key task headings are summarized in Tables 7-10. Phase I represents the development program currently in progress, while Phase II consists of preliminary design/development of a breadboard system, with supporting R&D effort. In Phase III, detail design, fabrication, and testing of a qualifiable flight prototype system will be accomplished, and in Phase IV the flight system will be qualified and manufactured. A tentative program schedule is shown in Figure 63 with major milestones indicated. An attractive option is that of identifying the flight prototype transport fluid passage design and all valving within Phase II. This would essentially eliminate the Phase III effort except for electronic components and evaporant supply tankage.

TABLE 7

FLASH EVAPORATOR FEASIBILITY STUDY
(PHASE I)

ANALYSIS AND DESIGN TASKS

- Define Basic Design Parameters
- Define Scale Models for Feasibility Tests
- Define and Develop Analytical Models for Prototype Design
- Investigate Flow Control Methods

FABRICATION AND TESTING TASKS

- Fabricate and Test Scale Models to Prove Feasibility
- Perform Preliminary Testing of Control Systems

OUTPUT: Two Flash Evaporator Configurations,
Analytical Model

TABLE 8

FLASH EVAPORATOR PRELIMINARY DESIGN/DEVELOPMENT
(PHASE II)

ANALYSIS AND DESIGN TASKS	FABRICATION AND TESTING TASKS
<ul style="list-style-type: none"> ◦ Define Performance Requirements for Breadboard Unit 	<ul style="list-style-type: none"> ◦ Support Configuration Definition
<ul style="list-style-type: none"> ◦ Optimize Evaporator Configuration: <ul style="list-style-type: none"> • Select Liquid Side Concept • Include Shuttle Integration Considerations 	<ul style="list-style-type: none"> ◦ Fabricate and Test Breadboard System ◦ Perform Materials Compatibility Tests
<ul style="list-style-type: none"> ◦ Define Full Scale Breadboard Evaporator System Design, Including Control System, Liquid Side Accumulator, Etc. 	<ul style="list-style-type: none"> ◦ Test a Candidate Nozzle for Freezing Tendencies Under Simulated Conditions
<ul style="list-style-type: none"> ◦ Upgrade Analytical Model Based on Test Results 	
<ul style="list-style-type: none"> ◦ Define Materials Compatibility Tests (For Example, Long Duration Exposure of Spray Head to Coolant) 	
<ul style="list-style-type: none"> ◦ Perform Analysis on Causes and Relief of Nozzle Freezing. Define a Test to Prove Analysis. 	

- OUTPUT: (1) Preliminary Performance & Requirements Estimate
- (2) Optimized Flash Evaporator System in Breadboard Form, Refined Analytical Model

TABLE 9

RESEARCH SUPPORT TO PHASE II AND
PHASE III EFFORT

TASKS

- ° EVALUATE ALTERNATE FLOW CONTROL SCHEMES
- ° STUDY EVAPORATOR EFFICIENCY ENHANCEMENT TECHNIQUES, INCLUDING:
 - USE OF MIXED FLUIDS
 - SURFACE CONDITIONING
 - EXHAUST FLOW HEATING
 - SPRAY PATTERN AND SHAPE VARIATIONS
 - DIELECTROPHORESIS
 - FLOW VISUALIZATION METHODS
 - SINGLE DROPLET IMPINGEMENT RESEARCH
 - EXPERIMENTALLY DEFINE PERFORMANCE MAP

OUTPUT: Inputs to Phase II and III Design Efforts
Confidence in End Item.

TABLE 10

FLASH EVAPORATOR FLIGHT PROTOTYPE DESIGN
(PHASE III)

DESIGN AND ANALYSIS TASKS

- Refine System Requirements to Reflect Shuttle CDR Results
- Perform Design, Reliability, and Maintainability Analyses
- Write Preliminary Specifications, Including GSE and OCS Requirements
- Select System Components
- Produce Detail Design
- Support Design Verification Test

FABRICATION AND TESTING TASKS

- Perform Tests in Support of Component Selection
- Fabricate Flight Prototype
- Perform Design Verification Test of Final Configuration

OUTPUT: Qualifiable Flight Prototype Evaporator System

(111)

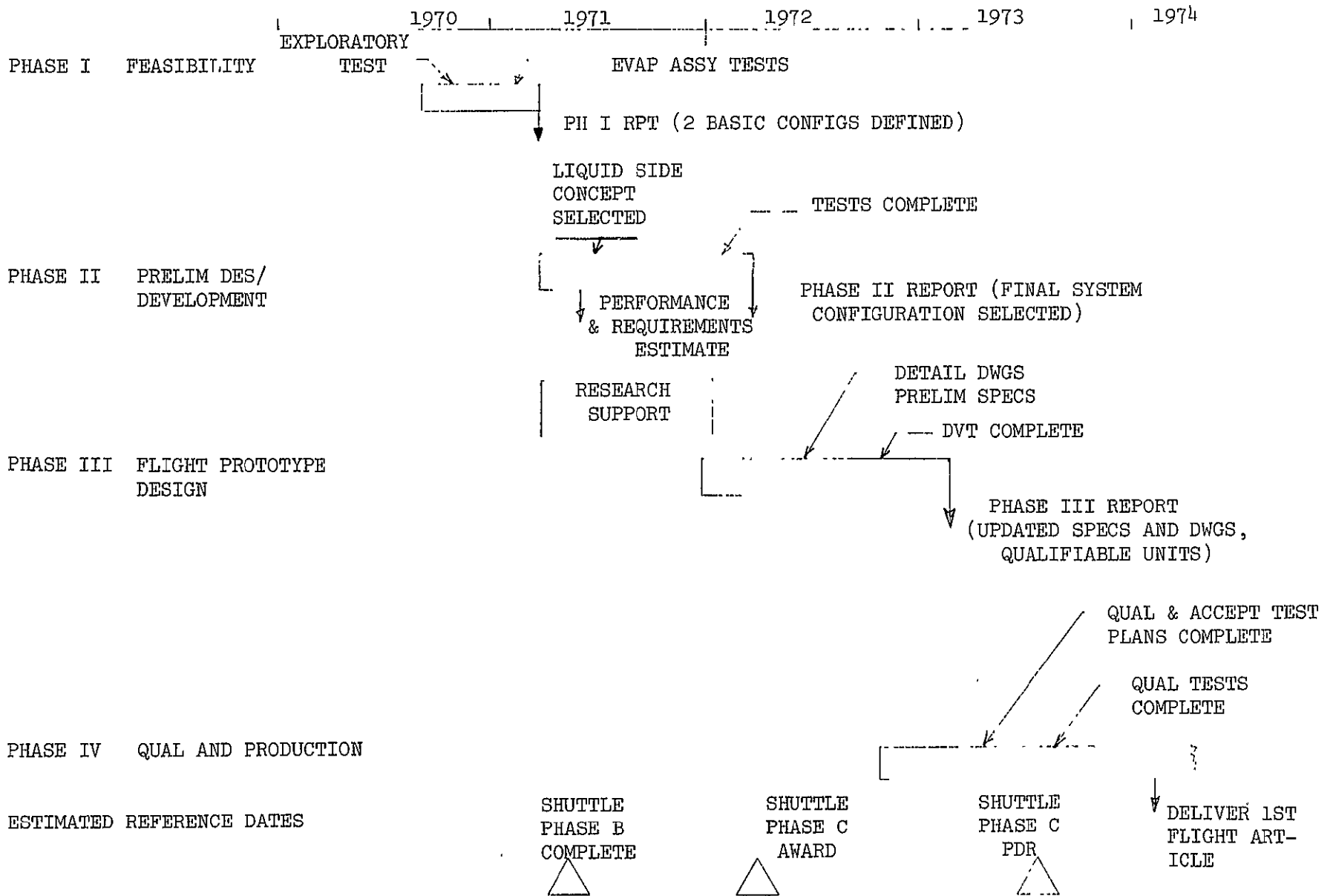


FIGURE 63
FLASH EVAPORATOR PROGRAM SCHEDULE

5.0 CONCLUSIONS AND RECOMMENDATIONS

There are numerous obstacles which, at the outset of this investigation, were considered capable of prohibiting the operation of the spraying flash evaporator. Among these were questions like "can the spray penetrate to the wall without freezing?", and "could stable nucleate or evaporative individual droplet transfer occur at the low pressures relative to the triple point?" Further there were and still are such a large number of independent variables which have not been explored that the same concept could proceed to an unrecognizable descendant of the present tentative design. Despite the numerous questions yet unanswered the work has demonstrated some very positive conclusions:

1. A simple spray of water may be directed through a low pressure vapor to a wall and evaporate with nearly complete liquid evaporation.
2. Pressure of vapor adequate for proper performance may be maintained with pulsed operation without an active backpressure control.
3. Heat fluxes of up to 20,000 BTU/hr-ft² at temperatures below 40°F have been demonstrated in a pair of evaporators at loads of up to 43,000 BTU/hr.
4. A simple on-off control scheme for water and two such controls for Freon and Ammonia have been demonstrated. Some refinement of the control scheme is required, but control by pulsing the evaporant flow is sufficient.
5. Effects of 4g accelerations were explored briefly and at most a moderate effect was experienced.
6. The water spray nozzles were found to cause potential problems of freezing the liquid hold up.
7. The device size was found to be dependent upon the quality of the heat transport fluid design.
8. A plan to pursue the development of the flash evaporator was formulated. Its adoption is recommended.

6.0 REFERENCES

1. Pedersen, C. O., "An Experimental Study of the Dynamic Behavior and Heat Transfer Characteristics of Water Droplets Impinging Upon a Heated Surface", Int. J. Heat & Mass Transfer, 13, pp. 369-381, (1970).
2. McGinnis, F. K., III, and Holman, J. P., "Droplet Heat Transfer Rates", Int. J. Heat & Mass Transfer, 12, pp. 95-108, (1969).
3. Sears, F. W., Thermodynamics, 2nd Edition, Addison Wesley, 1959.
4. Delaney, L. J., Houston, R. W., and Eagleton, L. C., "The Rate of Vaporization of Water and Ice", Chem Engr. Science, 19, pp. 105-114 (1964).
5. Steddum, R., et al, "Investigation of the Characteristics of Fluids Vented into a Vacuum".
6. Simmons, J. A., Gift, R. D., Markels, M., "Investigation of the Effects of Vacuum on Liquid Hydrogen and Other Cryogenes used on Launch Vehicles", ARC Final Summary Report, 18 Dec 1964, NASA AC #X6512159, CR60495.
7. Cho, S. H., and Sunderland, J. E., "Phase Changes of Spherical Bodies", Int. J. Heat & Mass Transfer, 13, pp. 1231-1233 (1970).
8. Engel, O. G., "Mechanism of Rain Erosion", WADC TR 53-192 (1953).
9. Kays W. M., Convection Heat Transfer, McGraw-Hill, 1966. _____
10. Lewis, B. ed Combustion Process, Vol. II of High Speed Aerodynamics and Jet Propulsion, Princeton U. Press, 1956.
11. Dawley, R. A., "The Expulsion of Water-Based Liquids into Hard Vacuum", Boeing Report D2-84191-1, 1966, AD 479076.
12. Gayer, M. D., "Flash Evaporator Nozzle and Basic Evaporator Tests", LTV Test Report 000TIR0090, 23 October 1970.
13. Rogers, R. R., "Flash Evaporator Concept Testing", LTV Test Report 000TIR0091, 9 March 1971.

APPENDIX
COMPUTER PROGRAM

This Appendix contains a brief description of the type of input required to operate CINDA followed by the details concerning the card input necessary to execute the program. Included is a listing of the models used in the study, for which card decks are available.

The data input for CINDA consists of several data blocks, each started by a BCD 3 block header card and terminated by an END card. A list of these data blocks and what information must be provided within these data blocks follows:

```
BCD 3 THERMAL SPCS
- None
END
BCD 3 NODE DATA
- List of all nodes, their initial temperature and capacitance
  values
END
BCD 3 CONDUCTOR DATA
- List of all conductors, their adjoining node numbers and
  conductor values
END
BCD 3 CONSTANTS DATA
- Program control constants having unique names and user constants
  which may be floating point numbers, integers or alpha -
  numeric characters
END
BCD 3 ARRAY DATA
- List of arrays which are required for the proper execution of
  VARIABLES 1 and VARIABLES 2. All arrays are in FORTRAN order
  and may contain any combination of integers, floating point
  values or alpha - numeric data. Each array is started with
  the integer array number and terminated by END.
END
BCD 3 EXECUTION
- List of program subroutines which call upon and cause the
  execution of VARIABLES 1, VARIABLES 2, and OUTPUT CALLS.
END
BCD 3 VARIABLES 1
- Should contain all the instructions necessary to completely
  define the network elements and boundary conditions prior to
  solving the network.
END
BCD 3 VARIABLES 2
- Should contain all past solution operations if there are any.
END
BCD 3 OUTPUT CALLS
- Should contain those print and plot options which are desired
  by the user.
END
BCD 3 END OF DATA
```

During the development of the various flash evaporator models proposed configurations were broken down into nodes and the input to the CINDA data blocks was generated. Reference should be made to the enclosed listing of a flash evaporator computer program as an aid in understanding what is discussed below.

BCD 3 NODE DATA

- Having determined the nodal breakdown, capacitance values were calculated and initial temperatures were assigned to them.

BCD 3 CONDUCTOR DATA

- Conductor numbers were then assigned to adjoining node pairs and initial conductance values were calculated or assigned.
- Those conductors which had temperature as time varying properties were assigned values since their actual values are calculated in VARIABLES 1.

BCD 3 CONSTANTS DATA

- Appropriate program control constants were set up and user constants were established as needed by EXECUTION, VARIABLES 1 and VARIABLES 2.

BCD 3 ARRAY DATA

- Arrays were established as necessary to provide required information to the EXECUTION, VARIABLES 1, AND VARIABLES 2 data blocks.

BCD 3 EXECUTION

- Desired CINDA subroutine calls were listed and appropriate additional storage locations were set up.

BCD 3 VARIABLES 1

- Within this data block the following operations are programmed as required by the different models.
 - (a) the evaporant spray pattern is defined
 - (b) heat rejection from those nodes which were subject to evaporant deposition is calculated
 - (c) conductance values are calculated for those conductors having temperature or time varying properties
 - (d) required parameters for the determination of the convective heat transfer coefficient are determined
 - (e) appropriate heat loads are impressed on the radiator and environmental cabin
 - (f) radiator bypass flow rate is calculated

BCD 3 VARIABLES 2

- Programmed in this data block are appropriate control schemes

BCD 3 OUTPUT CALLS

- A desired CINDA print option is listed

SUBROUTINE CNVTN

- This subroutine was written to calculate the convective heat transfer coefficient for both laminar and turbulent heat transport fluid flow. It is present in all the models except Model 1.

Presented in the sections which follow are listings of the flash evaporator thermal model computer programs which include in the proper sequence both the job setup cards and the fortran coded program. Within the discussions accompanying these listings will be the details on how to set up the inputs required to run these models on the computer. Copies of these decks can be obtained from the thermodynamics group at LTV-MSD.

```

17 RUN 00256,FC02,243JCU,370F,160,P,5,5
18 MSG FILE REF. TAPE 1 FH432 4 FSTPN 4
19 ASG G=17/07
20 ASG U,J,K,M
21 XOT CUR
TRW U
IN 6
IOC
DEL NOUI*/CODE
DEL NOTIN*/CODE
XOT CINDA

```

MORRIS

MODEL 1

RCD THERMAL SPCS

```

END
PCD THERMAL DATA
1,92.0,5505
2,92.0,3672
3,92.0,3672
4,92.0,3672
5,92.0,3672
6,92.0,3672
7,92.0,3672
8,92.0,3672
9,92.0,3672
10,92.0,3672
11,92.0,5505
12,92.0,352
13,92.0,512
14,92.0,284

```

$$C_i = L \times Vol \times C_p$$

NOT REPRODUCIBLE

END

RCD CONDUCTION DATA

```

1,1,2,0.03288
2,2,3,0.0493
3,3,4,0.0493
4,4,5,0.0493
5,5,6,0.0493
6,6,7,0.0493
7,7,8,0.0493
8,8,9,0.0493
9,9,10,0.0493
10,10,11,0.03288
11,11,12,0.0493
12,12,13,0.027
13,13,14,0.0087

```

$$G_i = kA/\Delta X$$

$$G = \frac{1}{\left(\frac{\ln(r_o/r_i)}{2\pi kL} + \frac{x}{kA}\right)}$$

$$G = \frac{1}{\frac{\ln(r_o/r_i)}{2\pi kL}}$$

END

PCD CONSTANTS DATA

```

1,6
2,10
OUTPUT,5.0
DIFMH,1.0
TIMEND,600.

```

```

No. of Nodes in Array 1
No. of Nodes in Array 5
Print Interval
Time Increment
Stop Time of Problem

```

END

RCD ARRAY DATA

```

1,9,10,11,12,13,14,END 5 NODES WITH EVAPORATION
2,0.0,0.0,54.15,34.6,50.25,28.3,END 6 EVAPORATION AREA
3,0.0,0.01300,30.0,0.01300,30.1,0.0
1200,0.0,END

```

Primary Deposition

Note that there is no comma after the last value on the first card of a two or more card array note also that a doublet pair cannot be broken up.

120

```

4,4,45.,FND HFG
5,1,2,3,4,5,6,7,8,0,10,END
6,54,15,30,1,36,1,36,1,72,2,72,2, 0,0, 0,0, 0,0,END
7,0,0,0,0200,30,0,00200,30,1,0,0,1200,0,0,END

```

Secondary Deposition

```

FND
PCD 3EXECUTION

```

```

F DIMENSION X(14)
F NPIV=14
F NTH = 0
  CSGRVP
  CNFRWD

```

```

FND
PCD 3VARIABLES 1

```

```

F N = K(1)
F M = K(2)
F ATOT = 0.0
F DO 15 J=1,N
F JTES1 = J

```

```

  ARYCTO(JTES1,RTFST,A2+1)
F 15 ATOT = ATOT + RTFST
  DIFCL1(TIMFO,A3,RTFST)
F FLOW = RTFST
  ARYCTO(1,RTFST,A4+1)
F HFG = RTFST

```

```

F DO 20 J=1,N
F JTES1 = J
  ARYCTO(JTES1,ITFST,A1+1)
  ARYCTO(JTES1,RTFST,A2+1)
F 20 W(ITFST) = Q(ITFST) - (RTFST/ATOT)*FFLOW*HFG
F IF (W .LT. 0) GO TO 40

```

121

```

F ATOT = 0.0
F DO 25 J=1,M
F JTES1 = J
  ARYCTO(JTES1,RTFST,A6+1)
F 25 ATOT = ATOT + RTFST
  DIFCL1(TIMFO,A7,RTFST)

```

```

F FLOW = RTFST
  ARYCTO(1,RTFST,A4+1)
F HFG = RTFST
F DO 30 J=1,M
F JTES1 = J

```

```

  ARYCTO(JTES1,ITFST,A5+1)
  ARYCTO(JTES1,RTFST,A6+1)
F 30 W(ITFST) = Q(ITFST) - (RTFST/ATOT)*FFLOW*HFG
F 40 CONTINUE

```

```

FND
PCD 3VARIABLES 2

```

```

FND
PCD 3OUTPUT CALLS
  PRNVP

```

```

FND
PCD 3END OF DATA

```

```

* X01 CLK

```

```

12 ERS
11 IN G
10 IOC
9 1PI G
8
7
6
5

```

NOT REPRODUCIBLE

- * FOR#K LINKU
- * FOR#K EXECFN
- * FOR#K VAR#L1
- * FOR#K VAR#L2
- * FOR#K QUICAL

TD HJG MOPFL IA NH3 RUN NO. 44 CON. NO. 7 HOPZ. SPRAY -
 * XOT LINKU

Title which is printed out at the top of each page of output.
 Columns 13 through 72 are available to the user for run
 identification.

122

12
11
10
9
8
7
6
5
4
3
2

ASG D,J,K,M

XQT LUR

IRW G

IN G

TOC

DEL NOTIN%/CODE

DEL NOTIN%/CODE

XQT CINUA

MODEL 4

RCD 31HERMAL LPCS

FND

RCD 3NODE DATA

01,45.0,2130	\$LIQUID DIFFUSION NODE
02,45.0,1200	\$LIQUID DIFFUSION NODE
03,45.0,1200	\$LIQUID DIFFUSION NODE
04,45.0,6718	\$LIQUID DIFFUSION NODE
05,45.0,6718	\$LIQUID DIFFUSION NODE
06,45.0,6718	\$LIQUID DIFFUSION NODE
07,45.0,6718	\$LIQUID DIFFUSION NODE
08,45.0,2149	\$LIQUID DIFFUSION NODE
09,45.0,1649	\$LIQUID DIFFUSION NODE
10,45.0,1150	\$LIQUID DIFFUSION NODE
11,45.0,0650	\$LIQUID DIFFUSION NODE
12,45.0,0170	\$LIQUID DIFFUSION NODE
13,45.0,0170	\$LIQUID DIFFUSION NODE
14,100,2,545	\$LIQUID DIFFUSION NODE
15,100,2,545	\$LIQUID DIFFUSION NODE
16,100,2,545	\$LIQUID DIFFUSION NODE
17,45.0,0170	\$LIQUID DIFFUSION NODE
18,45.0,0170	\$LIQUID DIFFUSION NODE
19,45.0,0045	\$LIQUID DIFFUSION NODE
20,70.0,0170	\$LIQUID DIFFUSION NODE
21,70.0,0510	\$LIQUID DIFFUSION NODE
22,70.0,0510	\$LIQUID DIFFUSION NODE
23,70.0,0170	\$LIQUID DIFFUSION NODE
24,70.0,0170	\$LIQUID DIFFUSION NODE
25,70.0,0510	\$LIQUID DIFFUSION NODE
26,70.0,0510	\$LIQUID DIFFUSION NODE
27,70.0,0170	\$LIQUID DIFFUSION NODE
28,45.0,0170	\$LIQUID DIFFUSION NODE
29,45.0,0035	\$LIQUID DIFFUSION NODE
30,45.0,4346	\$SOLID DIFFUSION NODE
31,45.0,2491	\$SOLID DIFFUSION NODE
32,45.0,2491	\$SOLID DIFFUSION NODE
33,45.0,1,000	\$SOLID DIFFUSION NODE
34,45.0,1,000	\$SOLID DIFFUSION NODE
35,45.0,1,000	\$SOLID DIFFUSION NODE
36,45.0,1,000	\$SOLID DIFFUSION NODE
37,45.0,3240	\$SOLID DIFFUSION NODE
38,45.0,2400	\$SOLID DIFFUSION NODE
39,45.0,1710	\$SOLID DIFFUSION NODE
40,45.0,0968	\$SOLID DIFFUSION NODE
41,45.0,0178	\$SOLID DIFFUSION NODE
42,45.0,0178	\$SOLID DIFFUSION NODE
43,100,5,918	\$SOLID DIFFUSION NODE
44,100,5,918	\$SOLID DIFFUSION NODE
45,100,5,918	\$SOLID DIFFUSION NODE

This is merely an identification message which may appear on any card within the entire program that has its initial value in column 12 or greater

123

NODE # CAPACITANCE VALUE

ASSIGNED INITIAL TEMPERATURE

7

C


```

46,95,0,.0178 $SOL IN DIFFUSION NONE
47,95,0,.0178 $SOL IN DIFFUSION NONE
48,95,0,.0089 $SOL IN DIFFUSION NONE
49,70,0,.0178 $SOL IN DIFFUSION NONE
50,70,0,27.04 $SOL IN DIFFUSION NONE
51,70,0,27.04 $SOL IN DIFFUSION NONE
52,70,0,.0178 $SOL IN DIFFUSION NONE
53,70,0,.0178 $SOL IN DIFFUSION NONE
54,70,0,27.04 $SOL IN DIFFUSION NONE
55,70,0,27.04 $SOL IN DIFFUSION NONE
56,70,0,.0178 $SOL IN DIFFUSION NONE
57,95,0,.0178 $SOL IN DIFFUSION NONE
58,45,0,.0089 $SOL IN DIFFUSION NONE
59,-460,,1.0 $BOUNDARY NODE

```

FND
RCD 3 CONDUCTOR DATA

```

01,-01,02,.139
02,-02,03,.139
03,-03,04,.139
04,-04,05,.139
05,-05,06,.139
06,-06,07,.139
07,-07,08,.139
08,-08,09,.139
09,-09,10,.139
10,-10,11,.139
11,-11,12,.139
12,-12,13,.139
13,-13,14,.0463
14,-13,15,.0463
15,-13,16,.0463
16,-14,17,.0463
17,-15,17,.0463
18,-16,17,.0463
19,-17,18,.1390
20,-18,28,0.000
21,-28,29,0.000
22,-18,10,.1390
23,-19,20,.0695
24,-20,21,.0695
25,-21,22,.0695
26,-22,23,.0695
27,-23,29,.0695
28,-19,24,.0695
29,-24,25,.0695
30,-25,26,.0695
31,-26,27,.0695
32,-27,20,.0695
33,-29,01,.1390

```

```

$ WDOT*CP CONDUCTORS
$ WDOT*CP CONDUCTORS
$ WDOT*CP CONDUCTORS
$ WDOT*CP CONDUCTORS
$ WDOT*CP CONDUCTORS
$ WDOT*CP CONDUCTORS
$ WDOT*CP CONDUCTORS
$ WDOT*CP CONDUCTORS
$ WDOT*CP CONDUCTORS
$ WDOT*CP CONDUCTORS
$ WDOT*CP CONDUCTORS
$ WDOT*CP CONDUCTORS
$ WDOT*CP CONDUCTORS
$ WDOT*CP CONDUCTORS
$ WDOT*CP CONDUCTORS
$ WDOT*CP CONDUCTORS
$ WDOT*CP CONDUCTORS
$ WDOT*CP CONDUCTORS
$ WDOT*CP CONDUCTORS
$ WDOT*CP CONDUCTORS
$ WDOT*CP CONDUCTORS
$ WDOT*CP CONDUCTORS
$ WDOT*CP CONDUCTORS
$ WDOT*CP CONDUCTORS
$ WDOT*CP CONDUCTORS

```

GEN 34,11,1,1,1,30,1,1.0,1.0,1.0,1.0

```

45,12,41,0.3440 $ HA CONDUCTORS
46,13,42,0.3440 $ HA CONDUCTORS
47,14,43,1.3900 $ HA CONDUCTORS
48,15,44,1.3900 $ HA CONDUCTORS
49,16,45,1.3900 $ HA CONDUCTORS
50,17,46,0.3440 $ HA CONDUCTORS
51,18,47,0.3440 $ HA CONDUCTORS

```

NOT REPRODUCIBLE

124

CONDUCTOR # INITIAL CONDUCTANCE VALUE

ADJOINING NODE PAIR

```

52,10,41,.01720      $ HA CONDUCTORS
53,20,49,.03440      $ HA CONDUCTORS
54,21,50,.69500      $ HA CONDUCTORS
55,22,51,.69500      $ HA CONDUCTORS
56,23,52,.03440      $ HA CONDUCTORS
57,24,53,.03440      $ HA CONDUCTORS
58,25,54,.69500      $ HA CONDUCTORS
59,26,55,.69500      $ HA CONDUCTORS
60,27,56,.03440      $ HA CONDUCTORS
61,28,57,.03440      $ HA CONDUCTORS
62,20,58,.01720      $ HA CONDUCTORS
63,30,31,.0011       $ KA/DELX CONDUCTORS
64,31,32,.0021       $ KA/DELX CONDUCTORS
65,32,33,.0208       $ KA/DELX CONDUCTORS
66,33,34,.0083       $ KA/DELX CONDUCTORS
67,34,35,.0083       $ KA/DELX CONDUCTORS
68,35,36,.0083       $ KA/DELX CONDUCTORS
69,36,37,.0093       $ KA/DELX CONDUCTORS
70,37,38,.0093       $ KA/DELX CONDUCTORS
71,38,39,.0068       $ KA/DELX CONDUCTORS
72,39,40,.0042       $ KA/DELX CONDUCTORS
-73,50,59,5.58E-11   $ RADIATION CONDUCTORS
-74,51,59,5.58E-11   $ RADIATION CONDUCTOR
-75,54,59,5.58E-11   $ RADIATION CONDUCTOR
-76,55,59,5.58E-11   $ RADIATION CONDUCTOR

```

END

RCD \$CONSTANTS DATA

```

1,8      $NUMBER OF NODES WITH EVAPORATIVE HEAT
2,11     $NUMBER OF FLOW CONDUCTORS
3,11     $NUMBER OF CONVECTION CONDUCTORS
4,11     $NUMBER OF PLATE CONDUCTORS
5,1      $CONTROL SCHEME SELECTION

```

These are user constants which are needed in VARIABLES 1, VARIABLES 2, and EXECUTION, e.g., as an index in a DO LOOP

```

OUTPUT,15.0
TIME1,1.0
NLOOP,200
DIRXCA,01

```

These are program control constants which control the program execution

```

TIME,ND,1800.0
IIFST,
JIFST,
KIFST,
LIFST,
MIFST,
PIFST,
SIFST,
TIFST,
UIFST,
VIFST,

```

These are program control constants which are used to obtain and store values in the ARRAY DATA block

END

RCD \$ARRAY DATA

```

1,33,34,35,36,37,38,39,40,END $NODES WITH EVAP
2,148.5,148.5,148.5,148.5,148.5,95.0,72.9,50,81,28,72,END $ARFA FOR NODES
3,.006944,1000.,END $ FLOW (LH/SFC), AND HEG (BTU/LB)
4,0.,0.,45.,360.,95.,900.,05.
1260.,45.,4800.,45.,END
5,.17884,END $HEAT TRANSPORT FLOW RATE
6,0.,0.,.006944,1000.,.006944,END $EVAPORATIVE FLOW VS TIME
7,32.0,1.00E-4,50.,.625E-4,100.,0.383E-4 $WATER VISCOSITY

```

125

12
11
10
9
8
7
6
5
4
3

```

140.,.242E-4,200.,.167E-4,250.,.0.129E-4  $ VS TEMP
340.,.0.38E-4,400.,.0.07E-4,FND  $ (LR/TN-SFC)
R,32.,.1.0,200.,.1.0,300.,.1.083,400.,.1.18R  $WATER SPECIFIC
440.,.1.285,500.,.1.415,FND  $HFAT(RTI/IB-F)
O,32.,.0.741E-05, 50.,.0.766E-05, 100.,.0.820E-05$WATER THERMAL
140.,.0.877E-05, 200.,.0.907E-05, 250.,.0.917E-05$CONDUCTIVITY
340.,.0.912E-05, 450.,.0.900E-05, 500.,.0.891E-05$(RTI/SEC-IN-F)
FND
10.,.0,1092.,200.,.078.,300.,.410.,END $LATENT HFAT H2O(RTI/IB)
11.,.0,0.3005, 50.,.0.3611, 100.,.0.3576 $WATER DENSITY
140.,.0.3542, 200.,.0.3478, 250.,.0.3390 $ (LR/TN**3)
340.,.0.3218, 450.,.0.3009, 500.,.0.2951 $
FND

```

NOT REPRODUCIBLE

```

12.,.0,13.5, 50.,.9.5, 100.,.4.6 $PRANPTL NO.
140.,.2.8, 200.,.1.9, 250.,.1.4 $FOR WATER
340.,.1.0, 450.,.0.7, 500.,.0.6 $(MU*CP/K)
FND
13.,.2.75,160.,.86,231.,.58,464.,.87,860.,.72,1256.,.57,1652.,.42
1413.,.675,2025.,.595,2108.,.06,2161.,.074,END $ ARRAY FOR ENTRY LENGTH
14.,.245.,.125.,.5,70.,.2,70.,.2,395.,.85,395.,.85
345.,.85,126.,.65,97.,.19,67.,.74,38.,.20,FND $D,FIL
15.,.0,END $ E IN FFLOW=F*WDOT
16.,.45.,.5.,.5.,END
17.,.0,0.,.037,237.,.036,472.,.032,706.,.026,1080.,.014
1415.,.0,0.,.4248.,.0.,.4608.,.014,4950.,.026,5184.,.032
4429.,.036,5663.,.037,END $LEFT RADIATOR HEAT LOAD/UNIT AREA
18.,.0,0.,.027,486.,.025,954.,.021,1415.,.016,1760.,.029
1764.,.015,3920.,.015,3924.,.020,4248.,.016,4716.,.021
4184.,.025,5670.,.027,END $RIGHT RADIATOR HEAT LOAD/UNIT AREA
19.,.0,2.,.317,5000.,.2.317,END $ Q ON CABIN

```

126

```

FND
PCD 3EXECUTION
DIMENSION X(100)
NPRIM=180
NTH=0

```

} These cards set up the necessary additional storage locations

```

CSCIMP
CNF,PK

```

```

FND
PCD 3VARIABLES L

```

```

T N = K(1)
F ATOT = 0.0
F DO 15 J=1,N
F JTEST = J
F 15 ATOT = ATOT + RTEST
F WDOT = RIFST
F HFG = RTEST
F IF (RIFST .EQ. 0.0) GOTO 60
F E=RTEST
F EFLOW=E*WDOT
F DO 20 J=1,N
F JTEST = J

```

} Calculate the total area of deposition within the evaporator

Get the maximum value of evaporant flow rate

Get the evaporant heat of fusion

Get the evaporant flow rate multiplier which has been determined by the control scheme

```

F ARY<TO(JTEST,ITEST,A1+1)
F ARY<TO(JTEST,RIFST,A2+1)

```

} Calculate Q on those nodes which have evaporant spray

F 20 Q(LTEST)=Q(LIFST)-(RTFST/ATOT)*FFLOW*HFG

F 60 NFLCN=K(2)
F NHACN=K(3)
F ARYCTO(1,RTFST,A14+1) %PICK UP FLOW ID
F RTFST
F ARYCTO(1,RTFST,A5+1) %PICK UP HT FLUID FLOW
F FLOW=PI*CT

F IMIX=(1(23)+(27))/2.
F XRP=(45.-TMIX)/(1(28)-1M(X)
F IF(XRP .GT. 0.0) XRP = 0.0
F IF(XRP .GT. 1.0) XRP = 1.0
F WDOTK= FLOW *(1.-XRP)
F WDOTBP= FLOW *XRP

Determine the radiator bypass flow rate and calculate appropriate values for flow conductances

F G(22)=WDOTR
F UO 2/ IE=23,32
F 27 G(1)=WDOTP/2.
F UO 28 IE=20,21
F 28 G(1)=WDOTRP
F IOUT=(WDOTR*IMIX+WDOTRP*(28))/FLOW
F IF(IOUT .GT. 45.) IOUT=45.
F I(29)=IOUT
F WP=3.14159*(D
F UO 10 IE=L,NFLCN
F RTFST=I(1)

127

F DIDEG1(RTFST,A8,STFST) %GET CP
F G(1)=FLOW*STFST
F DIDEG1(RTFST,A7,STFST) %GET VISCOSITY
F RE=4.*FLOW/STFST/WP
F DIDEG1(RTFST,A12,STFST) %GET PR
F PR=STFST
F DIDEG1(RTFST,A9,STFST) %GET THERMAL CONDUCTIVITY
F AK=STFST
F LTES=I

Obtain from the array data pertinent information before calling subroutine CNVTN

F ARYCTO(LTEST,STFST,A13+1) %PICK UP Y
F ARYCTO(LTEST,RTFST,A14+2) %PICK UP FLUID LUMP LENGTH
F FIL=RTFST
F WHI=3.14159*D*FIL
F Y=STFST
F NHAG=I + 33
F 10 CALL CNVTN(RE,PR,AK,Y,D,AHT,G(NHAG))

F UO 21 L=50,51
F DIDEG1(ITMF0,A17,RTFST)

F 21 Q(L)=(RTFST/2.)*130.

F UO 22 L=44,55
F DIDEG1(ITMF0,A18,RTFST)

F 22 Q(L)=(RTFST/2.)*130.

F UO 19 IE=43,45
F DIDEG1(ITMF0,A19,RTFST)

Impress the appropriate heat loads on the radiator and environmental cabin.

F 19 Q(1)=RTFST

F END

F RCD 3 VARIABLES 2

F IOUT=T(41)

F IOUT=T(41)

F IOUT=T(41)

F IOUT=T(41)

F IOUT=T(41)

F IOUT=T(41)

F IOUT=T(41)

F IOUT=T(41)

F IOUT=T(41)

F IOUT=T(41)

F IOUT=T(41)

F IOUT=T(41)

```

F   KODE=K(5)
F   IF(KODE.F0.0) GO TO 999
F   IF(KODE.F0.2) GO TO 530
-----
      ARY<TO(1,RTEST,A16+1) $GFT TFIX
      ARY<TO(2,STEST,A16+1) $GFT DFLTA1
      ARY<TO(3,TTEST,A16+1) $GFT DFLTA2
-----
F   IFIX=PIFCT
F   DFLTA1=STEST
F   DFLTA2=TI*ST
F   IFST1=IFIX+DELTIA1
F   IF(TOUT.GT,TEST1) GO TO 100
F   IFST2=IFIX-DELTIA2
F   IF(TOUT.LT,TEST2) GO TO 101
F   GO TO 102
F 100 E=1.0
      STORPY(1,1.0,A15+1)
F   GO TO 103
F 101 E=0.0
      STORPY(1,0.0,A15+1)
F   GO TO 103
F 102 CONTINUE
      ARY<TO(1,RTEST,A15+1)
F   E=RTEST
F 103 WRITE(6,15)E,TIMEN,TOUT
F 15  FORMAT(3H E=,3X,F3.1,3H,6HTIMEN=,3X,F8.2,3H,5HTOUT=,3X,F6.2)
F   GO TO 999
F 530 CONTINUE
      ARY<TO(1,RTEST,A16+1) $ GFT TFIX
      ARY<TO(2,STEST,A16+1) $ GFT DFLTA
      ARY<TO(3,TTEST,A16+1) $ GFT EMAX
      ARY<TO(4,UTEST,A16+1) $ GFT EDDOT
      ARY<TO(1,VTEST,A15+1) $ GFT E
-----
F   IFIX=PIFCT
F   DFLTA=STEST
F   EMAX=TI*CT
F   EDDOT=UTEST
F   E=VTEST
F   UT1=IOUT-TFIX-DFLTA
F   UT2=IOUT-TFIX+DFLTA
F   IF(ABS(TOUT-IFIX).LE,DELTA) GO TO 200
F   IF(TOUT.GT,TFIX) GO TO 201
F   EDDOT=EDDOT*DI2
F   IF(EDDOT.LT.(-FMAX)) EDDOT=-EMAX
F   GO TO 300
F 200 EDDOT=0.0
F   GO TO 300
F 201 EDDOT=EDDOT*DI1
F   IF(EDDOT.GT,FMAX) EDDOT=EMAX
F 300 DFLF=EDDOT*DTIMEII
F   E=E+DFLF
F   IF(F.GT.1.) F=1.0
F   IF(E.LT.0.) E=0.0
F   VTEST=E
      STORPY(1,VTEST,A15+1) $ STORE E
F   WRITE(6,400)E,TIMEN,TOUT
F 500 FORMAT(3H E=,3X,F7.5,3H,6HTIMEN=,3X,F8.2,3H,5HTOUT=,3X,F6.2)
F 999 CONTINUE

```

NOT REPRODUCIBLE

Control Scheme #1 (On-Off)

Control Scheme #2 (Proportional)

128

```

12 F   WRITE(6,400)E,TIMEN,TOUT
11 F 500 FORMAT(3H E=,3X,F7.5,3H,6HTIMEN=,3X,F8.2,3H,5HTOUT=,3X,F6.2)
10 F 999 CONTINUE
9
8
7
6
5
4
3
2

```

END

RCD 300 INPUT CALLS
PRNIMP

END

RCD 3000 OF DATA

* XOT LINK

ERS

IN G

TPI "

DEL NFINP%/CODE

NOT REPRODUCIBLE

* FOR CNVTN,CNVTN

SUBROUTINE CNVTN(RE,PR,AK,Y,D,AHT,G)

IF (RE.LF.2000.) GO TO 10

RF8=RF**0.8

PR3=PR**0.3

ANU=0.023*PR3*RF8

GO TO 20

10 CONTINUE

GRAF17=1./(RE+PR)*Y/D

GR3=GRAF17**0.3333333

DFNOM=GR3*FTZ + 0.015*GR3

ANU=3.66 + 0.0155/DFNOM

20 H=ANU*AK/D

G=H*AHT

RETURN

END

* FOR,K LINKU

* FOR,K EXECIN

* FOR,K VARPL1

* FOR,K VARBL2

* FOR,K UUTICAL

* P HDG _____ FLASH EVAPORATOR _____ MODEL_4

* XOT LINKU

Title Card: Columns 13 through 72 are available

129

12
11
10
9
8
7
6
5
4
3